COMPUTER SIMULATION OF DIAMOND FILM GROWTH BY CHEMICAL VAPOR DEPOSITION USING MONTE CARLO METHOD

By

JIAN XING

Bachelor of Science
Sichuan University
Chengdu, People's Republic of China
1982

Master of Science
Oklahoma State University
Stillwater, Oklahoma
1989

Submitted to the Faculty of the
Graduate College of the
Oklahoma State University
in partial fulfillment of
the requirements for
the Degree of
DOCTOR OF PHILOSOPHY
December, 1993

COMPUTER SIMULATION OF DIAMOND FILM GROWTH
BY CHEMICAL VAPOR DEPOSITION
USING MONTE CARLO METHOD

Thesis Approved:

Thesis Adviser

Dean of the Graduate College

ACKNOWLEDGMENTS

I take this opportunity to express my most sincere appreciation to Dr. H. L. Scott, my major adviser and thesis supervisor, for his most kind suggestion of the problem, and his invaluable guidance during this investigation and preparation of this thesis.

I wish to express my sincere gratitude to Dr. L. M. Raff, Dr. J. H. H. Perk, and Dr. B. J. Ackerson, the other members of my graduate committee, for their guidance and counseling. Especially, I wish to express my thanks to Dr. L. M. Raff for helpful discussions of surface chemistry of carbon.

I acknowledge financial support from the O. S. U. Diamond Research Group and Oklahoma State University Center for Energy Research (UCER).

I wish to express my thanks to Dr. P. A. Westhaus for much help during my graduate study here, and I also would like to express my thanks to everyone who has taught me or given me help in this department.

The completion of this work on my part is in reality the result of effects made by literally hundreds of persons who have been a part of my life, beginning with my parents, Mr. Yu-Ting Xing and Mrs. Shao-Qun Yang. I feel this is one place that appreciation for them should be expressed. Without their giving me constant guidance, support and strength throughout my life, it is impossible for me to have the success today. I won't ever forget my elder sister, Ms. Zhao Xing, for encouragement and assistance at all time. The same should be said of all members of my wife's family, especially her parents, Mr. Minquan Qin and Mrs. Chengwan Zhang.

Most significantly, I wish to express my deepest thanks to my wife, Zhi Qin, for her many sacrifices, infinite patience and constant understanding. I also wish this thesis is a gift to my daughter, Elaine Z. Xing.

TABLE OF CONTENTS

Chapter Page

LIST OF TABLES

LIST OF FIGURES

CHAPTER I

INTRODUCTION

1-1 The History of Diamond

As long as about three thousand years ago, man picked up a glistening pebble and by some chance found it to be different from other stones. It was extreme hardness. From that time, diamond began to acquire magical powers. The nature of the diamond had puzzled scientists for hundreds of years. The first well-documented experiment on a diamond was carried out by two Italian academicians, G. Averani and C. A. Targioni, in 1694 at the Accademio del Cimento in Florence [1]. They set up a large magnifying glass, focused a beam of light on a small diamond and saw it "crack, coruscate and finally disappear," leaving a minute quantity of blue ash. Some years later, the French physicist Babinet, along with eminent colleagues like the great French chemist Antoine-Laurent Lavoisier, proved beyond reasonable doubt that diamond was carbon in exceptionally pure form. One of Lavoisier's most celebrated experiments (in 1772 [2]) was, to place a diamond in a bell jar filled with oxygen which rested in a basin containing mercury. The rays of the sun were then focused on the diamond by means of a large magnifying glass. After the diamond had been consumed, the bell jar was found to contain great quantities of carbonic acid, indicating to Lavoisier that the diamond was composed principally of carbon.

Diamond was shown to consist only of carbon by the English chemist Smithson Tennant in 1797 [3], when he burned some carefully weighed diamonds in oxygen enclosed in a vessel made of gold. The weight of the carbon in the carbon dioxide that resulted corresponded very closely to the weight of the original diamond [4]. Today we can make chemical measurements with vastly higher precision.

We now know that any gem quality diamond is at least 99.5 % pure carbon. The remainder is mainly nitrogen plus some hydrogen and oxygen.

By the beginning of the nineteenth century it was reasonably well established that diamond and graphite are both made of the same chemical element, carbon [5]. But just how were the particles aggregated? What is the difference in the way the carbon atoms are bonded that determines whether they make a crystal of diamond or a lump of charcoal? In 1913, William Henry Bragg and his elder son William Lawrence Bragg used x-ray diffraction on diamond to determine how the carbon atoms were arranged. According to their publication [6], the arrangement is illustrated in Fig. 1. The Bragg model showed how every atom is at the center of a tetrahedron of four other atoms. Their model was completely consistent with the x-ray data and it gave the correct density for diamond. The model is still completely accepted today.

A few years later, in 1924, J. D. Bernal, working with Bragg at the Royal Institution in London, published his results for the structure of graphite [7]. Fig. 2 shows his model, in which the atoms are linked closely in a two-dimensional net, each mesh of the net being a hexagon. The separation of the neighboring atoms in the hexagons is smaller than the carbon-carbon spacing in diamond (1.42 Å against 1.54 Å), and the bonding is very strong, so that graphite exhibits in the plane of the cleavage sheets considerable hardness. The planes, separated by about 3.4 Å, are too far apart for the atoms to bond together strongly. The weak bonding between the planes, combined with the strong bonding within the planes, enables them to slide over each other while remaining intact. This property is exploited when graphite is used as a lubricant.

1-2 Physical and Chemical Properties of Diamond

Diamond, the hardest of all materials, has many unique properties besides hardness such as high thermal conductivity, high chemical resistance, low friction and wear, optical transparency.

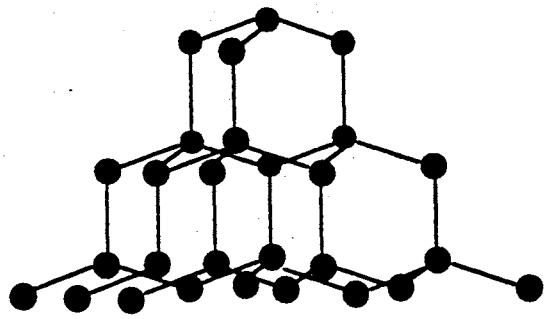

(a)

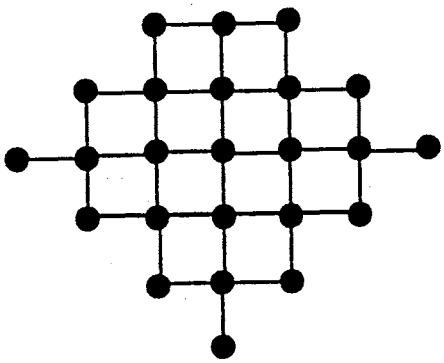

(b)

Figure 1. Two views of the atomic model of diamond, made by W. H. and W. L. Bragg [6]: (a) sideview, (b) top view. The black balls represent carbon atoms and the rods show the chemical bonds between nearest neighbor atoms.

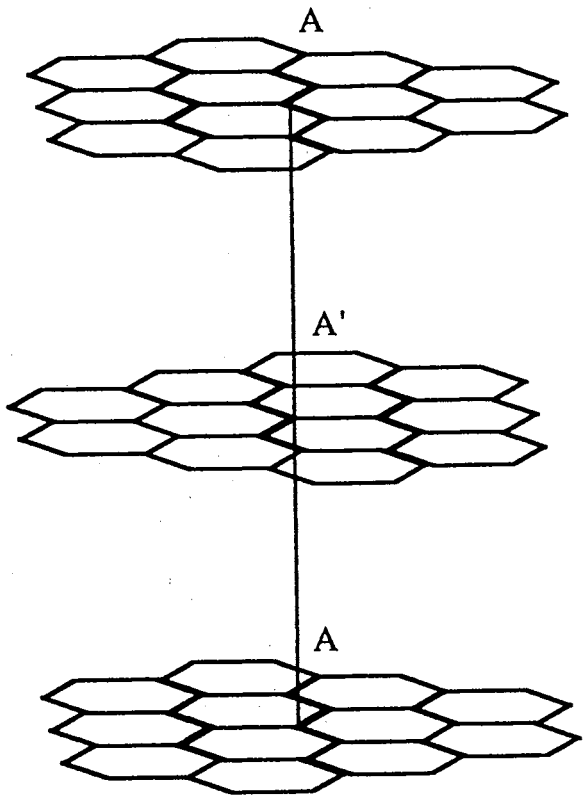

Figure 2. Crystallographic structure of graphite, as found by J. D. Bernal [7]. One carbon atom is located at the apex of each hexagon. In the common form of graphite (shown here) the crystal structure repeats after one intermediate plane (sequence AA'A on the vertical line).

As we described in the previous section, carbon atoms in diamond are bonded together by covalent bonds in a tetrahedral coordination pattern. Carbon atoms are relatively small atoms, and the smaller interatomic distance between atoms, the stronger are the covalent bonds. This property of diamond determines its hardness. For example, carbon is the smallest atom in the fourth group of the periodic table of elements. The next element of the fourth group is silicon. Semiconducting silicon has the same crystal structure as diamond. However, silicon atoms are larger than carbon atoms. The distance between neighbors in silicon is 2.34 Å compared with 1.54 Å in diamond. It has been comfirmed that the large spacing of the silicon lattice makes it less strongly bonded than the compact diamond crystal. In the electronics industry, silicon ingots are cut to the required size by diamond. In the construction industry, diamond saws and drills cut concrete reinforced with steel. In the oil business, diamonds stud tough rock-drilling bits.

Because the atoms in diamond are both light and strongly bonded, they can vibrate at unusually high frequencies. The maximum frequency is about $40 \times 10^{12} H_Z$, compared with $16 \times 10^{12} H_Z$ in silicon and $6 \times 10^{12} H_Z$ in common salt [5]. The high vibrational frequencies give diamond several important properties. The first is the high thermal conductivity. From the quantum physics point of view, if the thermal energy (kT) is comparable with, or larger than, the quantum energy of a vibration ($h\nu$), the vibration is very likely to be set off. In the case of diamond, the frequencies are unusually high. The quantum energies required to create vibrations are therefore also large and so, compared with any other crystal, at room temperature there are relatively few vibrations present in a diamond. The diamond lattice is relatively static and ordered, and heat waves can easily move through it. The connection between heat and atomic vibration is simply that the atoms in a hot crystal vibrate more than in a cold crystal. When we warm part of a crystal, the atoms in that part are made to vibrate more than usual. These vibrations spread out in the cooler parts of the crystal, conducting the heat outwards. For a crystal to be a good conductor of heat, the vibrational waves must be able to spread out easily. Waves can move most easily through a perfectly

ordered crystal (an imperfect region of the crystal may scatter the waves). At room temperature, a diamond conducts heat six times better than copper does, five times better than silver does [8]. Thus it can make a heat sink with far better performance than any other material. Diamond is also a semiconductor, with a high frequency limit 32 times better than silicon. Moreover, a high-power, high-voltage diamond transistor will be smaller than its silicon or gallium arsenide counterparts of the same rating. The shorter dimensions of the diamond device mean that charge carriers have less distance to travel and are simultaneously subject to a more intense electric field. This advantage lets it operate 40 - 100 times faster than a silicon or gallium arsenide device [9].

The second important property is the high transparency to most infared radiation. Vibrations of the atoms in a crystal can also be created by infrared radiation. One of the conditions is that the frequencies of the radiation and the vibration must be equal so that the two waves may resonate together. The frequencies absorbed by pure diamond are about $6 \times 10^{13} Hz$ corresponding to wavelengths of about 5 μm, ten times shorter than the wavelength for common salt [5]. Diamond windows are transparent at the wavelengths absorbed by almost any other materials. For example, Carbon dioxide lasers are capable of delivering tens of kilowatts of power at their lasing wavelength of 10.6 μm which is absorbed by most materials. However, a pure diamond window, 0.1 mm thick, absorbs less than a ten-thousandth of the 10.6 μm radiation passing through it. The excellent thermal conductivity of diamond ensures that even the small fraction of the energy absorbed by the window is rapidly conducted away.

Because the carbon atoms in a diamond are already strongly bonded to each other, diamond is nearly chemically inert. Diamond windows can therefore be used for optical measurements on highly reactive chemicals in materials research. Diamond windows are very strong, chemically inert, and transparent to a wide range of wavelengths. Their high thermal conductivity protects them against local heating. They are also used in space research because they remain transparent under withstanding extreme mechanical force, unpleasant atmosphere and high

temperature. For example, a diamond window, with the size of 18.2 mm diameter and 2.8 mm thick, and weight of 2.5 gram, was used in the Pioneer space probe to Venus which was launched in 1978.

The surfaces of diamonds are all water-repelling at room temperature, and diamond is also hard enough to take a highly-finished cutting edge which is straight to a few tens of atomic spacings and which is extremely sharp, with a radius of curvature of only a few tens of atomic spacings. These properties are exploited when diamond knives are used to cut biological tissue. As the knife cuts through water-containing tissue, the tissue is repelled, on the atomic scale, from the diamond. This is especially important when thin sections of tissue are being cut (as thin as 10 μm). Diamond surfaces also have the useful property of having a low coefficient of friction. It is the best material used as a stylus in record players or as bearings in mechanical industry.

Since diamond has such extraordinary physical and chemical properties, scientists have attempted to synthesize diamond for many years. The next two sections will briefly describe experimental and theoretical, more specifically computer simulation, research in diamond synthesis.

1-3 Experimental Research on CVD Diamond Synthesis

The earliest attempts to make diamond took place in the early nineteenth century. In 1828, J. N. Gannal tried to crystallise diamonds out of a solution rich in carbon [10]. Around 1850, in Paris, C. Despretz studied the electric arc between a platinum electrode and a graphite electrode to make diamond [11]. In 1866, a further attempt to use electricity in diamond synthesis was made by E. Lionnet by decomposing carbon disulphide using the voltages created between a gold leaf and a ribbon of tin. At that time, although the scientific reasons were not yet understood, the South African mines gave the clue: diamonds formed within the earth were certainly created in an environment of very high pressure and very high temperature, so the road to diamond synthesis lay along the path of high pressures and high temperatures. In the late 1870s, J. B. Hannay, an English chemist, heated

a closed tube to get the highest static pressures, in Hannay's time, to synthesize diamond [12]. Unfortunately, the temperatures used by Hannay (he quotes a 'dull red heat') and the pressures attainable by the gases inside the tubes were both far too low to have synthesized diamonds. During the next few decades, other great scientists had developed the technologies of high temperatures and high pressures to attempt to make diamond. H. Moissan, a French chemist, awarded Nobel prize in chemistry for his achievements with fluorine and for introducing the electric arc to high-temperature chemistry, used his electric furnace to obtain temperatures as high as 3000 °C during his diamond synthesis experiments in 1904 [13]. In 1907, C. A. Parsons reported the results of about a hundred experiments involving heating charcoal under 16,000 atmospheres to make diamonds [14] and by 1920, he had completed thousands of experiments [15]. The final results were still negative [16].

The main reason why the early synthesisers' attempts to make diamonds failed was that they had very little scientific guidance as to how to crystallise diamond. It was not until the first decade of this century that scientific theories relevant to synthesising diamond were consolidated. From that time to mid-1955, scientists have concentrated on the problem of making diamond on how to transform graphite into diamond. Thermodynamic theory has been applied to seek the conditions of pressure-temperature phase diagram in which carbon is more stable as diamond structure than as graphite structure [17–23].

In 1955, General Electric Research Laboratory in Schenectady, New York, USA, announced that diamonds had been synthesised, and that a reliable, repeatable processes had been developed [24]. By mid-1955 over one hundred successful runs had been achieved, and diamond crystals of up to 1 mm in size were displayed by General Electric. The success of General Electric resulted primarily from (1) the conditions for synthesising diamonds based on thermodynamic calculations was established; (2) a solvent-catalyst was used to make the diamond synthesis proceed quickly; (3) a new high pressure system designed by Hall being used. Fig. 3 shows the results of the General Electric work [5]. At atmospheric pressure, pure nickel, as a solvent-catalyst, melts at about 1700 K, but when it is in contact with carbon

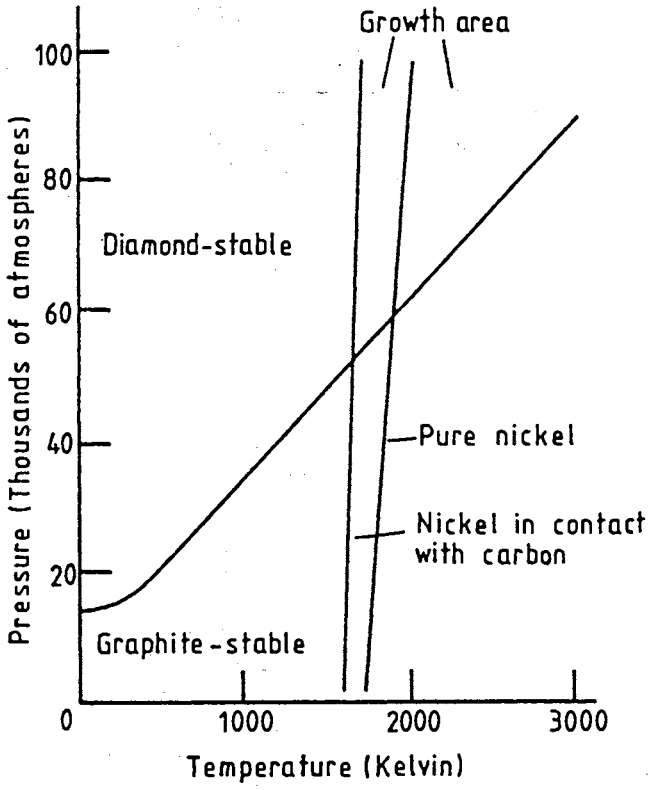

Figure 3. The pressure-temperature phase diagram for carbon, with nickel catalyst, from the results of the General Electric team [5]. The near vertical lines show the melting curves for nickel. Molten nickel lies to the right of the lines. Diamond production requires molten nickel plus a pressure high enough to make diamond more stable than graphite. Diamond production therefore occurs in the top right part of the diagram.

the melting temperature is reduced, and the nickel melts at about 1600 K. The melting point is slightly dependent on the pressure. Successful synthesis occurred at high pressure ($\geq$ 50,000 atmospheres, high enough to be inside the diamond-stable growth region of the phase diagram) and high temperature ($\geq$ 1700 K, high enough to melt the nickel-graphite mixture) (called HP-HT).

The possibility of synthesis of diamond at low pressure in the graphite-stable region where diamond is metastable (LP-HT) was investigated in the late 1950s. This is done by depositing, at a very low rate, carbon atoms on the surface of the diamond. Because the carbon atoms arrived individually, each could bond to the existing lattice, forming part of a new layer of diamond. The first patent on this method was taken out in 1958 in the USA and in 1961 in Canada, separately, by W. G. Eversole of the Union Carbide Corporation [25,26]. Eversole obtained carbon by decomposition of methane. Since then, many scientists were interested in the method. Angus, Will and Stanko [27], Deryagin and Fedoseev [28], successfully synthesized diamond using a similar method. Two factors which limit the usefulness of this method are: (1) there is always a tendency for graphite to form on the surface of the seed, since graphite is the stable form of carbon at these low pressures. Eversole found that he had to stop the growth and clean the graphite from the surface every hour; (2) the growth rates were extremely low (about $10^{-3}\mu$m h^{-1}).

In the mid-1970s Russian researchers, Deryagin, Spitsyn and their co-workers, made a key contribution by showing that atomic hydrogen rapidly etches graphite preferentially, leaving diamond intact [29] [30,31]. With this contribution the modern era of diamond synthesis under low-pressure metastable conditions began by refocusing attention on the method of chemical vapor deposition (CVD) based on hydrocarbon and hydrogen reactants [32–34]. In 1982, Japanese researchers, Matsumoto et al. [35], used tungsten filaments and microwave-assisted CVD methods to produce diamond films at growth rates of the order of 1 μm h^{-1}. Since then, several activated CVD processes involving thermal (hot filament) or

plasma (direct-current, radio-frequency, microwave) activation, electron-enhanced or ion beam deposition, and laser ablation have been developed [36–38].

In 1988 Japanese researchers Hirose, Amanoma, Okada and Komaki announced the synthesis of diamond using a combustion flame at atmospheric pressure with growth rates of about 30 μm h^{-1} [39]. Many researchers including those from the U.S.A. Naval Research Laboratory [40], Pennsylvania State University [41], Auburn University [42] and Oklahoma State University [43] in the U.S.A., and many others around the world have used this technique which is simple and consists of using an oxy/acetylene welding torch with a slightly fuel-rich mixture. Growth rates with this method have been reported up to 150 μm h^{-1}.

Recently, diamond growth rates in excess of 300 μm h^{-1} or deposition areas of $\geq$ 200 cm^2 have been demonstrated by using atmospheric-pressure combustion torches or plasma jets. In spite of the above experimental advances, the elementary growth mechanisms of diamond synthesis by CVD are still not clear and research progress has been slow. In the following section theoretical research and computer simulation of diamond CVD will be described.

1-4 Theoretical Research on CVD Diamond Synthesis

As with any CVD technique, diamond CVD involves a many component gas phase and surface reactions and interactions. Our understanding of the deposition mechanism involves several aspects such as gas-phase activation, diamond crystal nucleation on the substrate, diamond growth, adsorption and desorption processes, and diffusion along the growing surface. A schematic of the diamond CVD process is shown in Fig. 4. The aspects mentioned above in the theoretical researches of diamond CVD will be discussed below.

Diamond Surfaces

The crystal structure of diamond [44] is shown in Fig. 5. The space lattice of diamond is *fcc*. The primitive basis has two identical atoms at 000 and $\frac{1}{4}\frac{1}{4}\frac{1}{4}$.

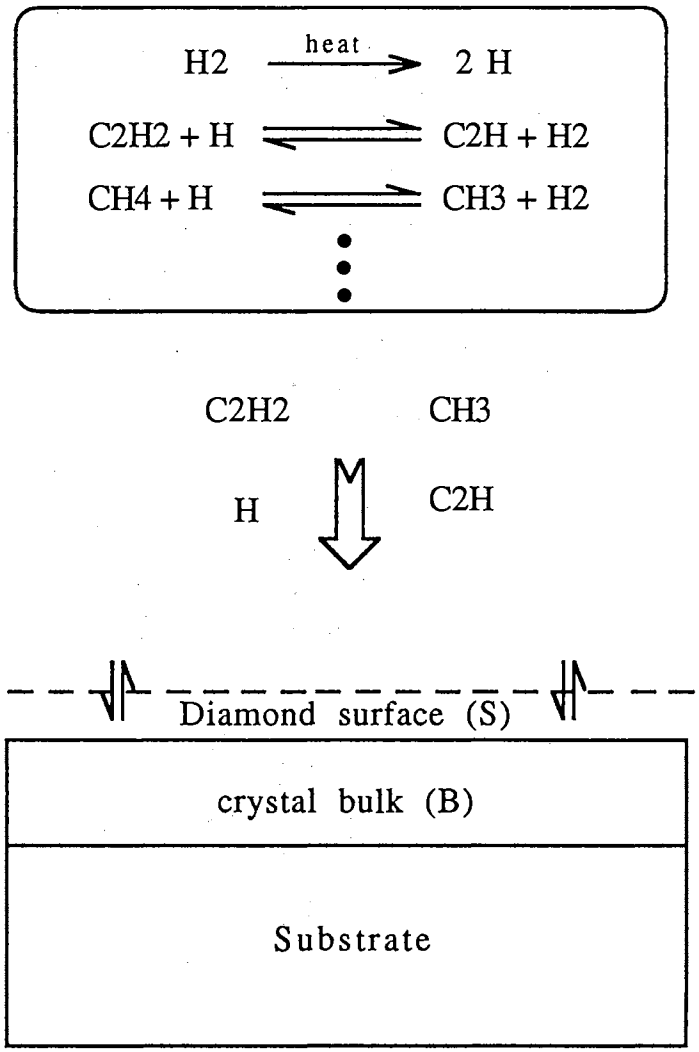

Figure 4. A schematic picture of the diamond CVD process. Various reactive and transport processes are shown in the gas-phase and surface. Chemical desorption and adsorption through a boundary layer (dashed line), diffusion along the surface (S), and into the crystal bulk (B), may also occur.

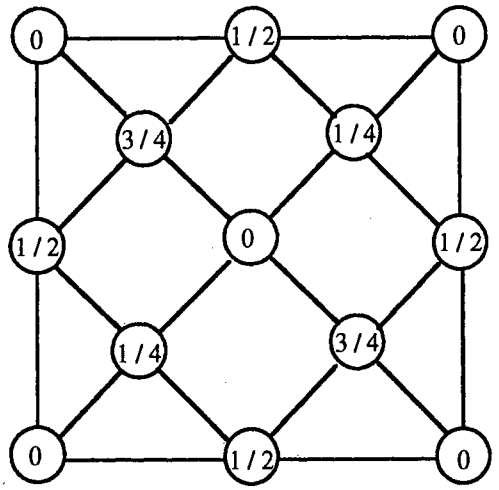

(a)

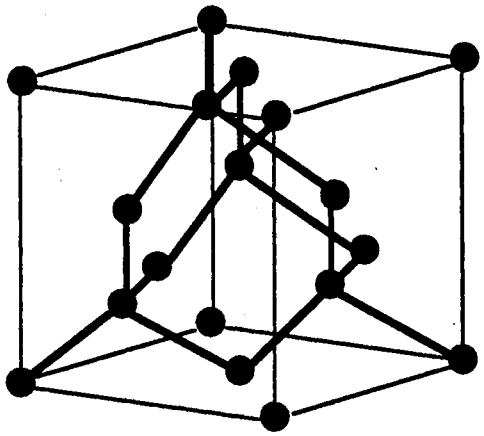

(b)

Figure 5. Diamond structure. (a) Atomic positions in the cubic cell of the diamond structure projected on a cube face; fractions denote the height above the base in units of a cube edge. (b) Crystal structure of diamond showing the tetrahedral bond arrangement.

In Fig. 5 (a), the points at 0 and $\frac{1}{2}$ are on the *fcc* lattice; those at $\frac{1}{4}$ and $\frac{3}{4}$ are a similar lattice displaced along the body diagonal by one-fourth of its length. Thus the conventional unit cube contains eight atoms. The tetrahedral bonding characteristic of the diamond structure is shown in (b). Each atom has 4 nearest neighbors and 12 next nearest neighbors.

Under conditions of chemical vapor deposition, heated diamond surfaces are exposed to atomic and molecular hydrogen, as well as various hydrocarbon species. The diamond (111) surface has attracted a lot of interest because of its technological importance in the growth of thin films. Pate [45] provided an excellent summary of the atomic and electronic structure of the (111) surface. Experiments show that the cleaved and polished diamond (111) surface is terminated with $C-H$ bonds and retains the bulk structure [45] [46–48], called 1X1 LEED (low energy electron diffraction) pattern or C(111)-(1X1), repeat structure of one unit cell by one unit cell, shown in Fig. 6.

The (100) diamond surface has been studied in a number of experiments [50–52]. The cleaved and polished diamond (100) surface is dihydride-terminated bulk structure, diamond C(100)-(1X1), shown in Fig. 7(a). Annealing above 1300 K in vacuum produces a diamond C(100)-(2X1) monohydride structure (Fig. 7(b)) [50], or a diamond C(100)-(2X1) π bonded structure (Fig. 7(c)) [53].

The (110) diamond surface is the least-studied of low index planes. The as-polished surface exhibits a 1X1 LEED pattern consistent with the structure of the truncated bulk [53]. Unlike the (111) and (100) surfaces, no reconstruction is observed after annealing to over 1300 K [54].

Diamond CVD Gas-Phase

The gas-phase in diamond acetylene-based CVD systems has been characterized, through many experiments [55–68]. It consists of important reactive species, such as atomic hydrogen H, and the diamond "growth species", such as molecules

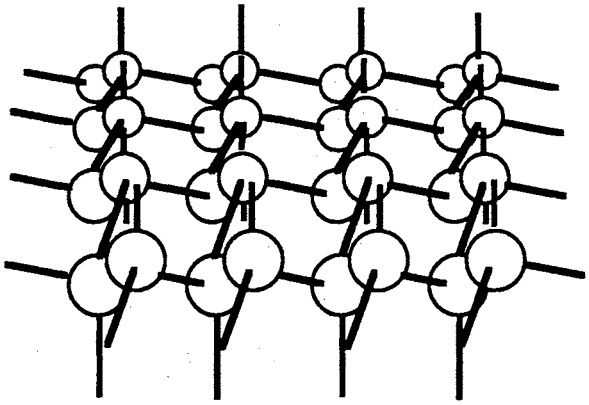

Figure 6. Structure of diamond (111) surface: The cleaved and polished diamond (111) surface is terminated with $C - H$ bonds and retains the bulk structure, called C(111)-(1X1).

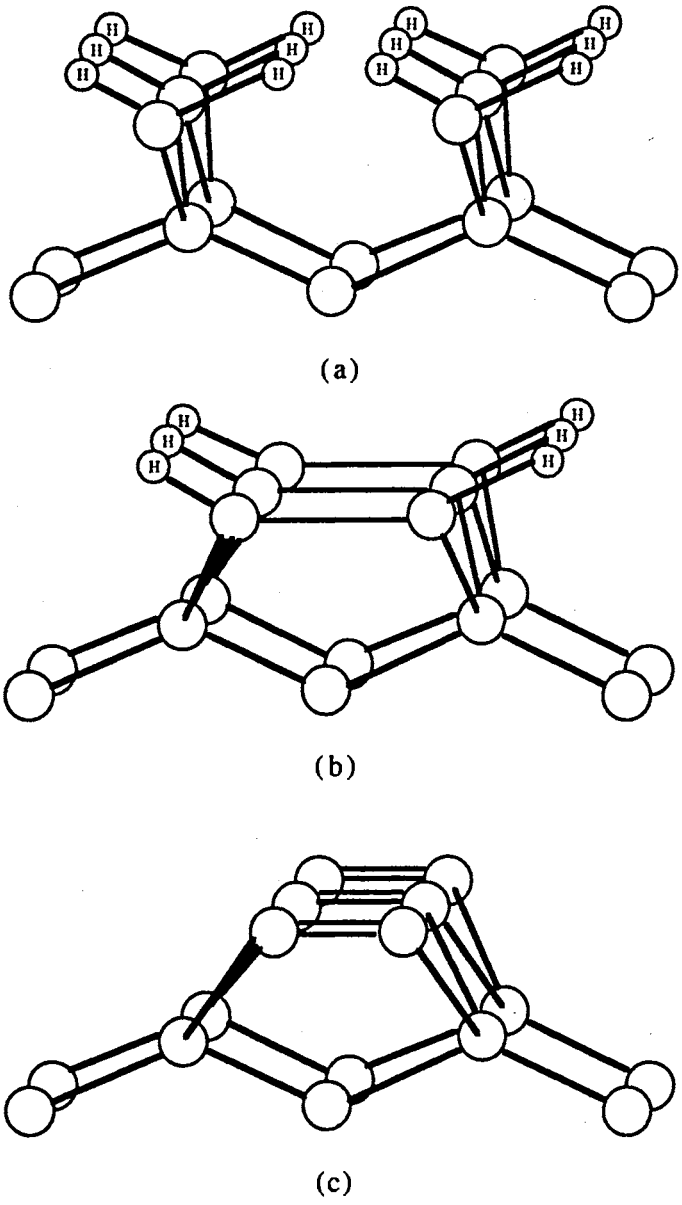

Figure 7. Structure of diamond (100) surface: (a) The cleaved and polished diamond (100) surface is a dihydride-terminated bulk structure, called C(100)-(1X1). (b) Annealing above 1300 K in vacuum produces a diamond C(100)-(2X1) monohydride structure, or (c) a diamond C(100)-(2X1) π bonded structure.

CH_4, C_2H_2, radicals CH_3, C_2H. The concentration of gas-phase species dependents on several variables like specific activated CVD processes, gas-phase temperature and the ratio of gaseous mixtures. Fig. 8 shows high concentrations of CH_4, C_2H_2, C_2H and H, as well as lower densities of CH_3 and C_2H_4, which were detected during diamond growth from CH_4/H_2 mixtures in the filament-assisted diamond CVD growth [57]. Mitsuda et al [66] have reported that abundant C_2H_2 and CH_4 signals were observed by using mass spectrometry from Ar(Argon)$/H_2/CH_4$ and $Ar/H_2/C_2H_2$ microwave plasma jets. Matsui et al have measured the composition of oxy/acetylene combustion flames as a function of the C_2H_2/O_2 using laser-excited fluorescence(LEF) and sampling mass spectrometry [63]. In the range $1.0 \leq C_2H_2/O_2 \leq 1.2$, the mole fraction of unburned acetylene remaining in the flame is nearly identical to that for the ethynyl radical C_2H, but for $C_2H_2/O_2 = 1.5$, the mole fraction of acetylene exceeds that for C_2H.

Based on the composition measurements of diamond CVD gas-phase and energy calculations, theoretical researchers assumed that the primary growth species could include acetylene (C_2H_2) [69–72]; C_2H_2 and ethynyl radical (C_2H) [73,74]; methyle (CH_3) [75,76]. More detailed discussions about various models of primary growth species will be given in later sections.

Diamond Crystal Nucleation Substrates

There has been much work directed toward understanding the diamond nucleation phenomenon, especially nucleation on nondiamond substrates including Hf, Ta, W, Ti, Nb, Mo [77–81] and Si, Ni, Pt [59] [82–87]. Nucleation is most commonly assisted by abrasion or seeding [88] with diamond powder. Diamond abrasion reduces the induction time for nucleation and increases the nucleation density [89] [90].

Belton and coworkers have performed x-ray photoelectron spectroscopy (XPS), electron energy loss spectroscopy (EELS), and low energy electron diffraction (LEED) of filament-assisted diamond deposition on Si, Ni and Pt [82,83] [59]. Based on the experimental results, they proposed a model for nucleation

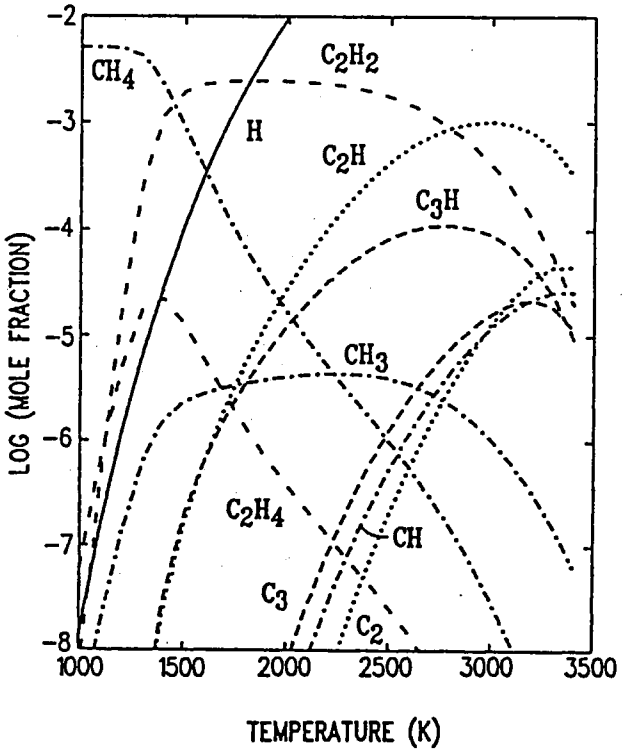

Figure 8. Concentrations of gas-phase species for a 0.5 % CH_4/H_2 mixture at thermal equilibrium in the filament-assisted diamond CVD growth process [57].

on scratched platinum and nickel substrates [84]. They concluded that diamond nucleates on platinum and nickel by pre-deposition of graphitic carbon precursors. Defect sites in these graphite deposits contain the nucleation sites for diamond. These nucleation sites are sensitive to the presence of gas phase oxygen species. Addition of oxygen to the gas phase suppresses diamond nucleation by elimination of the nucleation sites but does not suppress growth of existing diamond. Their model is shown in Fig. 9: (a) high oxygen concentrations clean (etch) the platinum surface of all graphitic deposits; (b) graphitic carbon precursors pre-deposit by decreasing oxygen; (c) formation of diamond nucleation sites occur on the graphite; (d) diamond nucleation occurs with low oxygen feed gases; (e) growth continues under the high oxygen conditions which did not nucleate graphite.

The interface studies have been quite important for insight into surface species present during growth, but it has not been possible to establish theoretical calculations to answer the questions such as: were the graphitic islands present during growth on the platinum surface necessary nucleation sites for diamond, or simply a competitive carbon deposition channel? Do the carbide layers detected on various surfaces play an active role in the nucleation step?

Diamond Growth Models

Based on the fact that acetylene is the most stable gaseous product in a flame capable of producing diamond film at high temperature, Frenklach and Spear have proposed an elementary-reaction mechanism as a model of diamond growth on the $C(111)$ diamond surface. According to their model, the main monomer growth species is acetylene (C_2H_2) and the reaction mechanism consists of two alternating steps: surface activation by H-atom abstraction and subsequent adsorption of an acetylene molecule [69]. The adsorbed acetylene is attached to the diamond substrate by a single $C-C$ bond. A subsequent hydrogen-atom transfer forms a radical site at which a second C_2H_2 can attach. Huang, Frenklach, and Maroncelli (HFM) applied molecular orbital calculations on a 9-carbon model compound to

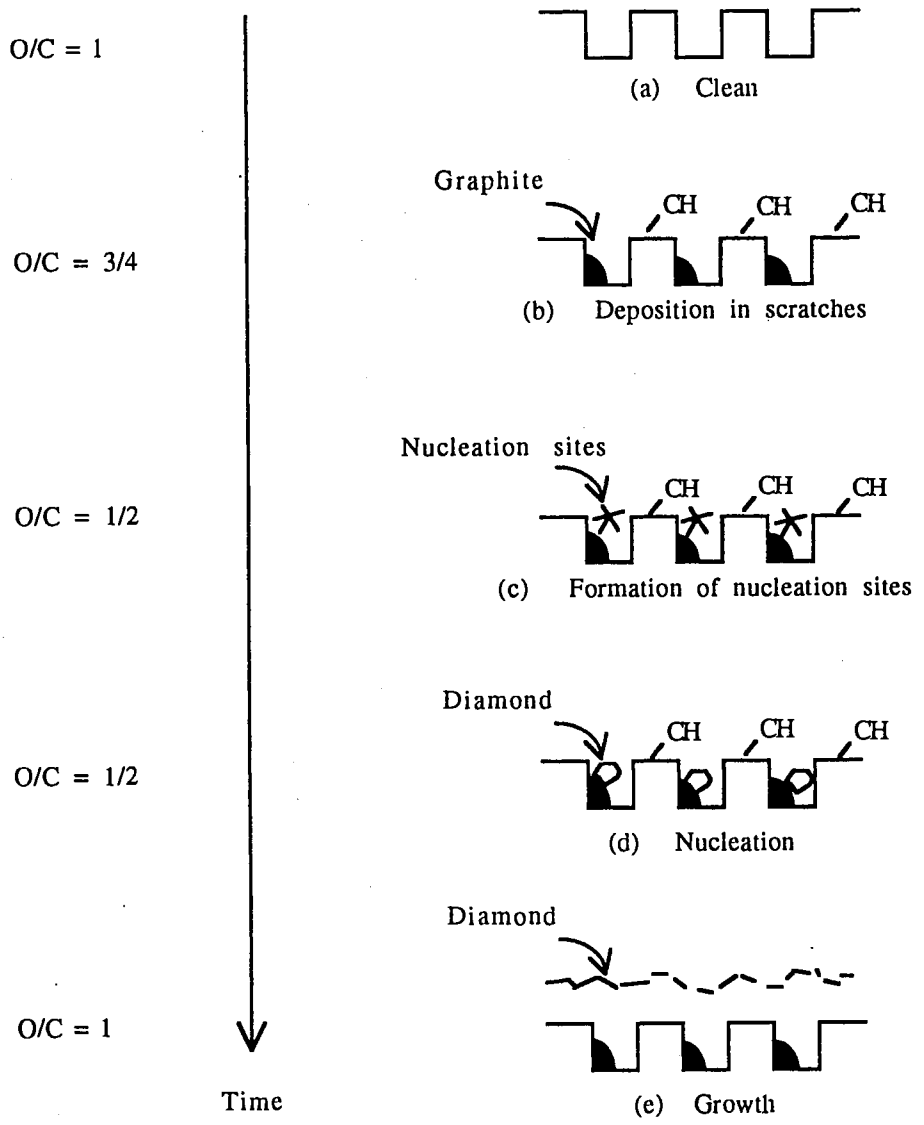

Figure 9. Belton et al's nucleation model [84] on the scratched platinum substrate. (a) high oxygen concentrations clean (etch) the platinum surface of all graphitic deposits; (b) graphitic carbon precursors pre-deposit by decreasing oxygen; (c) formation of diamond nucleation sites occur on the graphite; (d) diamond nucleation occurs with low oxygen feed gases; (e) growth continues under the high oxygen conditions which did not nucleate diamond.

verify that their model was energetically favorable [71]. Frenklach has recently added methyl radical, CH_3, in the vapor phase [91] (see later section).

Harris and Belton have suggested on the basis of thermochemical analysis that the mechanism of Frenklach and Spear may not lead to diamond film formation because the desorption of the second acetylene may occur at a rate which is similar to the adsorption rate [92]. They propose as an alternative that acetylene binds to the substrate via the formation of *two* $C-C$ bonds simultaneously. Harris has also proposed a diamond growth model based on methyl radical CH_3 addition to the $C(100)$ surface [93].

Raff and coworkers have found that the ethynyl radical C_2H is capable of forming any bonds that acetylene might theoretically form; the reaction probabilities for an ethynyl radical are significantly greater than those for the corresponding reactions of acetylene. Consequently, C_2H may be a more important diamond growth species than acetylene [73]. They conclude that the HFM mechanism [69] [71] with C_2H as the principal growth species may play a significant role in diamond film growth.

1-5 Numerical Simulations

Modern computer technology provides us with a powerful tool to model and simulate the processes of diamond CVD growth. Much of the current theoretical modeling work is based upon assumed reaction rates which are at best only poorly understood under the physical conditions present during diamond film growth. Efforts to better understand these conditions and their effect on reaction rates can come from computational simulations. Numerical simulations, including molecular dynamics simulation (MD) and Monte Carlo simulation (MC), have considerably enhanced our understanding of the diamond CVD process.

Molecular Dynamics Simulations

Molecular dynamics simulations (MD) compute the motions of individual molecules, which describe how positions, velocities, and orientations change with time. In effect, molecular dynamics constitutes a motion picture that follows molecules, in certain potential-energy environment, as they dart to and fro, twisting, turning, colliding with one another. MD has been extensively applied to the theoretical studies of chemical reactions occurring on solid surfaces [108–110,99–101].

Frenklach and coworkers [115] used quantum mechanically derived forces, a semiempirical AM1 [101] potential from the MOPAC quantum-chemistry program package [116], to calculate classical atomic trajectories for reactions on hydrogenated diamond $C(111)$ surfaces. The initial configuration of their model was two layers diamond structure formed by 16 carbons labeled from $1 \rightarrow 16$, and 4 hydrogen atoms labeled from $17 \rightarrow 20$. Then, they let one acetylene molecule deposit on the surface to form a "chair" conformation of the C_3H_5 diamond structure. They found the existence of a trapped, physisorption state for an acetylene molecule colliding with a diamond surface at 1200 K, a temperature typical of diamond CVD.

Peploski, Chang, Thompson and Raff employed the empirical hydrocarbon potentials #1 [117] and #2 [73] developed by Brenner [118] to perform molecular dynamics simulations of elementary surface reactions of H-abstraction, and C_2H_2 and C_2H deposition in diamond CVD studies. Trajectories were computed by solution of the classical Hamiltonian equations of motion. Their results indicated the following [73]: (1) The sticking coefficients for acetylene on a clean $C(111)$ surface lie in the range 0.25-0.33 for incident translational energies between 1.5-2.0 eV with surface temperatures in the range 1000-1500 K. (2) Chemisorption of acetylene most frequently involves the formation of two $C_S - C$ single bonds to adjacent adsorption sites on the $C(111)$ surface. (3) Chemisorption of acetylene via the formation of one $C_S - C$ single bond to yield an ethenyl radical is observed and the

subsequent desorption of this species does not appear to be a high probability process on the clean $C(111)$ surface. (4) The addition of a second acetylene molecule is a very low probability process for all surface structures investigated except the clean $C(111)$ surface. When such chemisorption does occur, the probability of subsequent desorption of the acetylene molecule is large unless the ethenyl radical is able to subsequently form a second $C-C$ bond. (5) Addition of a $\dot{C} \equiv CH$ radical to a chemisorbed acetylene group proceeds with a much higher probability than is the case for C_2H_2. The ethynyl radical is also chemisorbed readily to other surface structures with a low probability of subsequent desorption. It therefore appears to be a more important diamond growth species than acetylene.

An earlier empirical classical many-body potential proposed by Tersoff [119–122] has also been applied to the molecular dynamics studies of diamond CVD by Halicioglu [109], and Kaukonen [110] et al. For instance, Kaukonen and Nieminen simulated the growth of diamondlike films and overlayers by the deposition of energetic carbon atoms by molecular dynamics method (MD) in 1991. They used the interatomic many-atom potential suggested by Tersoff to calculate the carbon-carbon interactions.

Monte Carlo Simulations

Monte Carlo simulations (MC) provide a most valuable means for investigating the kinetics of phase transitions [123,124]. There are several that model various types of kinetic processes on lattices, including chemical reactions in the gas phase [125], adsorption-desorption at surfaces [126–130], surface diffusion [131,132], thin film nucleation and growth [91] [133–136].

Based on a Poisson process, Fichthorn and Weinberg [126] applied a dynamical Monte Carlo method to 128 $\times$ 128 square lattices (only for the purpose of theoretical study of dynamical Monte Carlo simulation) with assumed adsorption rate r_A and desorption rate r_D for investigating lattice gas adsorption-desorption at surfaces. Kang and Weinberg [131] reported that a dynamic Monte Carlo with an energy barrier had been explored to surface diffusion studies. 5000 particles

were initially generated on a 100×100 lattice with given force constant k for the harmonic wells.

Mak and coworkers [132] reported their Monte Carlo studies of surface diffusion on inhomogeneous surfaces. They have considered two situations on the surface: surface with blocks and surface with traps (without blocks). For the model without blocked sites, they assumed that the transition probability from one site to another was independent of the binding energy of the site to which the particle jumps. For the model with blocks randomly distributed on the lattice, they calculated the collective diffusion coefficient by assuming that the binding energy ϵ of a site was a random variable governed by a distribution function $p(\epsilon)$. The sizes of their simulations were 40×40 and 50×50 square lattices.

"A real time Monte Carlo simulation of thin film nucleation in localized-laser chemical vapor deposition" has been reported by Kotecki and Herman [134]. A three dimensional ($55 \times 55 \times 10$) grid was defined and a molecule was placed at a random position on the $X - Y$ plane at the lowest position in Z, or (x, y, z_{min}), with a probability given by a constant surface reaction efficiency Θ. Based on a Van der Waals attraction, the normalized bond strength factors bs_1, bs_2 and bs_3 were assumed as certain constant numbers. Probabilities for adatom migrations and desorptions were considered as functions of bs_1, bs_2 and bs_3. They modeled SiH_4 gas (300 K) incident onto surface with the rate of impingement: $R_{SiH_4} = 2.63 \times 10^5 P_{SiH_4}\ (atomic\ site)^{-1}(second)^{-1}$. P_{SiH_4} is the silane pressure in Torr. The maximum number of deposited particles against the real time scale was calculated.

Matsumura et al [135] applied the Kawasaki dynamical Monte Carlo method to the simulation of $Li_1(CuPt)-type$ ordered structure in a III-V alloy of $A_{0.5}B_{0.5}C$ during the (001) epitaxial growth. The configurational term E_c in the internal energy for the surface plane of A and B atoms was assumed to be a function of pairwise interaction parameters $V(\vec{r}_2 - \vec{r}_1)$. The interactions with the first and second nearest neighboring atoms were calculated in units of V_{h1}, a fixed interaction constant.

For modeling of diamond film growth, Chen [133] has explored the rate equations to solve the gas-phase reactions of H radicals with methane CH_4, and used the Monte Carlo method to study the surface reactions. The $CH_n(n = 0 \rightarrow 4)$ species arrived at various diamond lattice sites randomly. He assumed that for all radical species $CH_n(n = 0 \rightarrow 3)$ the sticking coefficients were equal, while for CH_4 the sticking coefficient was negligibly small. He also presented a value for the degree of preference for dangling-bond and CH-bond bonding. He let each deposited radical freely rotate its orientation to facilitate formation of bonds with its four neighbors.

Recently, Frenklach [91] carried out ballistic Monte Carlo simulations of diamond CVD process. As a crystalline seed a $C_{10}H_{16}$ tetrahedral cluster was initialized. Methyl radical CH_3 was added in the vapor phase. Constant per-site rate coefficients for hydrogen abstraction and addition, and reaction probabilities for the addition of CH_3 or C_2H_2 were assumed to determine reaction time increment Δt. The results of the simulations are that the methyl radicals attach readily to the substrate, and , after hydrogen abstraction, provide additional sites for acetylene adsorption. Frenklach's study did not consider surface diffusion, desorption-adsorption, and orientational relaxation on the diamond surface.

This thesis reports our studies of diamond CVD applying a dynamical Monte Carlo method to a molecular model. A semiempirical potential energy function developed by Brenner [118] has been used to govern all events including hydrogen abstraction and addition, C_2H_2 and C_2H desorption-adsorption from or to surface, surface diffusion, and orientational relaxation on the diamond surface. The next chapter will describe the theoretical basis for our studies, including the dynamical Monte Carlo method, the Brenner semiempirical potential energy function, and the main chemical reactions of our molecular model. In chapter 3, detailed methods of our studies will be given. Finally, results and discussion will be presented in chapter 4.

CHAPTER II

THEORY

2-1 The Monte Carlo Method in Statistical Physics

General Aspects of the Monte Carlo Method

The Monte Carlo method has been used in statistical physics studies to model equilibrium and non-equilibrium thermodynamic systems by stochastic computer simulation [123] [137]. The Monte Carlo method consists of a biased sampling of the phase space of system of many particles, and under certain circumstances it will correctly predict the thermodynamic properties of the system.

Consider a system of N particles in volume V at temperature T with Hamiltonian $H(q,p)$. In the canonical ensemble, the thermodynamic average of any observable quantity $A(q,p)$ has the form

$$\langle A \rangle = \frac{\int_\Omega A(q,p) e^{-H(q,p)/k_B T} d^{3N}q d^{3N}p}{\int_\Omega e^{-H(q,p)/k_B T} d^{3N}q d^{3N}p} \tag{1}$$

where Ω is the phase space of system, k_B is the Boltzmann constant.

For the Monte Carlo method, the integral of Eq. (1) is evaluated by sampling points in Ω, selected according to a probability distribution, $P(\mu)$, of state μ [123]. In this case, the integral Eq. (1) can be approximated by a summation formula [138]

$$\langle A \rangle = \frac{\sum_{\mu=1}^{M} A(\mu) e^{-H_\mu/k_B T}/P(\mu)}{\sum_{\mu=1}^{M} e^{-H_\mu/k_B T}/P(\mu)}. \tag{2}$$

At thermal equilibrium

$$P(\mu)_{eq} = \frac{1}{Z} e^{-H_\mu/k_B T} \tag{3}$$

where Z is partition function of the system. If we use P_{eq} in Eq. (3), we get

$$\langle A \rangle = \langle A \rangle_{eq} = \frac{1}{M} \sum_{\mu=1}^{M} A(\mu) \tag{4}$$

where M is the total number of configurations (total number of phase states). $A(\mu)$ could be any observable quantity associated with the system.

The random walk through phase space must be defined so that $\langle A \rangle = \langle A \rangle_{eq}$. This is done in the following manner : Let W be the transition probability per unit time from configuration μ to configuration μ' in the phase space of the system. The first derivative of $P(\mu)$ with respect to time t can be written as the master equation

$$\frac{dP(\mu)}{dt} = -\sum_{\mu} W_{(\mu \to \mu')} P(\mu) + \sum_{\mu'} W_{(\mu' \to \mu)} P(\mu'). \tag{5}$$

We wish to construct a random walk through phase space via a Markov process, such that $P(\mu)$ tends towards $P_{eq}(\mu)$ as the total number of steps M is sufficiently large [123]. In equilibrium the left hand side of Eq. (5) is zero, so that the detailed balance is achieved

$$W_{(\mu \to \mu')} P(\mu) = W_{(\mu' \to \mu)} P(\mu'). \tag{6}$$

In equilibrium, we expect $P(\mu) = P_{eq}(\mu) \propto e^{-H_\mu / k_B T}$, so that

$$\frac{W_{(\mu \to \mu')}}{W_{(\mu' \to \mu)}} = \frac{P_{eq}(\mu')}{P_{eq}(\mu)} = e^{-(H_{\mu'} - H_\mu)/k_B T} = e^{-\Delta H_{\mu \to \mu'} / k_B T}. \tag{7}$$

Now we choose $W_{\mu \to \mu'}$ (this choice is not unique [139]) to satisfy Eq. (7):

$$W_{\mu \to \mu'} \propto \begin{cases} 1 & \Delta H_{\mu \to \mu'} \leq 0 \\ e^{-\Delta H_{\mu \to \mu'} / k_B T} & \Delta H_{\mu \to \mu'} > 0 \end{cases} \tag{8}$$

The choice of Eq. (8) is called Metroplis sampling [137]. In terms of a random walk through phase space, the Monte Carlo algorithm can be executed : If $\Delta H_{\mu \to \mu'} \leq 0$, we accept the move. If $\Delta H_{\mu \to \mu'} > 0$, according to the probability $W_{\mu \to \mu'}$ in Eq. (8), we accept the move for $e^{-\Delta H_{\mu \to \mu'} / k_B T} \geq x$ or reject the move for $e^{-\Delta H_{\mu \to \mu'} / k_B T} < x$, where x is a random number distributed uniformly from 0 to 1. The transition probability of Metroplis walk, $e^{-\Delta H_{\mu \to \mu'} / k_B T}$, as function of ΔH is plotted in Fig. 10 (a).

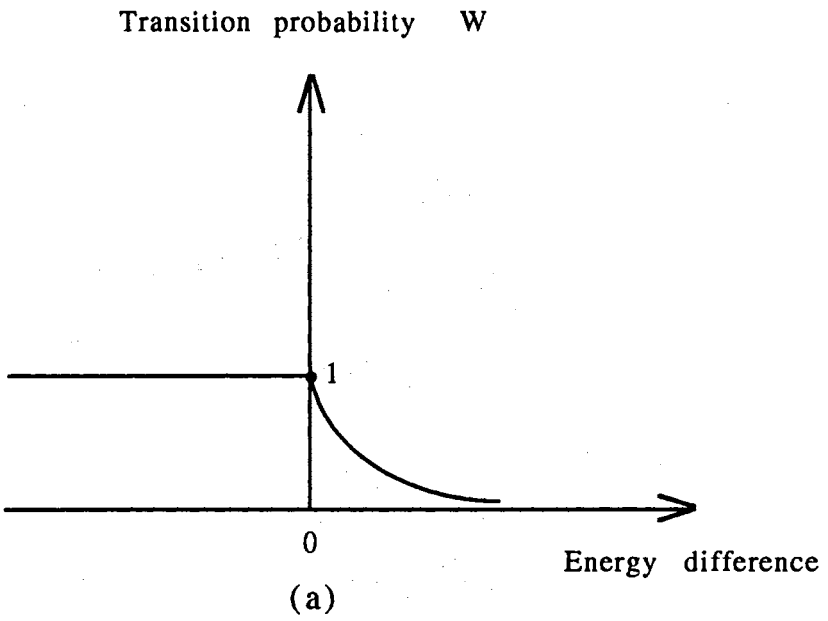

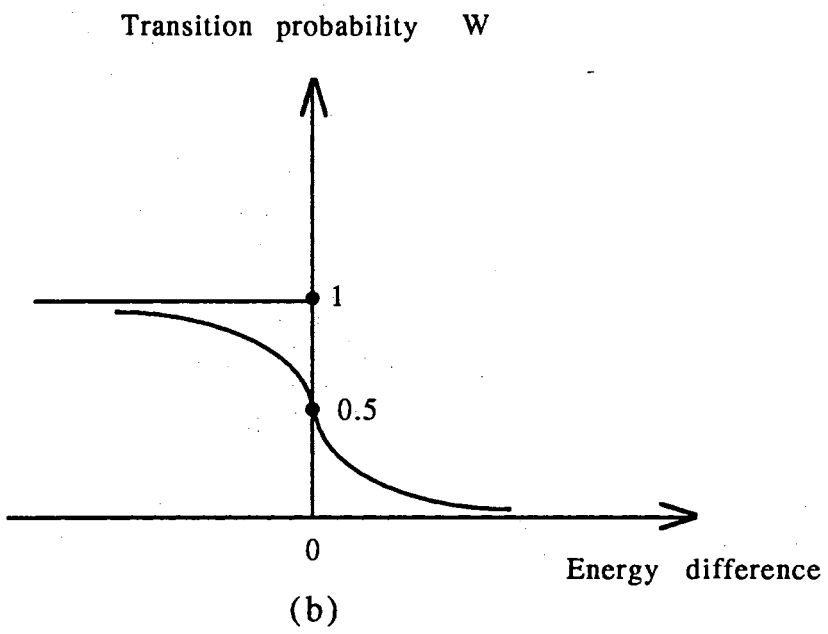

Figure 10. Plots of transition probabilities for (a) Metroplis walk, and (b) Kawasaki dynamics

Dynamical Monte Carlo Processes

The Monte Carlo method can also be applied to study dynamic behavior [123] [140], including surface diffusion of adsorbate atoms in adsorbed monolayers, nucleation of ordered domains from a disordered phase, kinetics of nucleation and phase separation, kinetics of crystal growth.

One of the theoretical foundations of dynamical Monte Carlo processes is Kawasaki dynamics [141–143]. In 1966 Kawasaki published his studies of the time-dependent Ising model. In this model, spin interactions were replaced by certain temperature-dependent transition probabilities (W) for spin exchange. Kawasaki proposed a local-equilibrium approximation to satisfy the detailed balance Eq. (6), then, calculated the diffusion constant and transport coefficients for the system described by the master equation Eq. (5).

Based upon the time-dependent Ising model, Kehr and Binder [140] studied self-diffusion and collective diffusion in interacting lattice gases, including systems with order-disorder phase transitions. They exploited the Kawasaki model to chose as transition probability of a particle to jump from site i to a vacant site f in their studying of simulation of diffusion in lattice gases and related kinetic phenomena

$$W_{i\to f} = \frac{1}{2}[1 - \tanh(\frac{\Delta E_{i\to f}}{2k_B T})], \tag{9}$$

where $\Delta E_{i\to f}$ is the energy difference between the final (f) and initial (i) situations.

In the simulation, a random number x is picked up to compare with the transition probability $W_{i\to f}$, a function of energy change $\Delta E_{i\to f}$. Then, according to Monte Carlo criteria:

If $x < W_{i\to f}$ the jump is performed;

If $x > W_{i\to f}$ no jump occurs.

Fig. 10 (b) shows the plot of Kawasaki transition probability, Eq. (9). To obtain a diffusion constant with dimensions they suggested converting transition probabilities into transition rates with a "time" unit of one Monte Carlo step (MCS) or "Monte Carlo time" [140] [144].

Matsumura et al [135] also reported applications of Kawasaki dynamical Monte Carlo simulation in their studies of crystal epitaxial growth of III-V semiconductor alloys. This thesis presents an application of the Kawasaki dynamic Monte Carlo simulation method to diamond CVD studies. The next section will describe the Brenner empirical potential surface employed in our simulation.

2-2 The Brenner Potential Energy Surface

Based on the Abell-Tersoff bonding formalism [119–122,145,146], Brenner [118] has developed an empirical many-body potential energy surface, with additional terms that correct for an inherent overbinding of radicals and including nonlocal effects. The Brenner energy function captures many of the essential features of chemical bonding in hydrocarbons such as producing the intramolecular energetics and bonding in solid diamond and graphite as well as large number of hydrocarbon molecules, and including buckminsterfullerene [147]. The mathematical expression of the Brenner empirical potential energy for hydrocarbons [118] is described in the following paragraphs.

The binding energy for the hydrocarbon potential is given as a sum over bonds in the form

$$E_b = \sum_i \sum_{j(>i)} [V_R(r_{ij}) - \bar{B}_{ij} V_A(r_{ij})]. \tag{10}$$

In Eq. (10), the sum is over all pairs of atoms i and j within a cut-off radius determined by a function $f_{ij}(r)$ to be described later. $V_R(r_{ij})$ and $V_A(r_{ij})$ are pair-additive repulsive and attractive interactions, respectively,

$$V_R(r_{ij}) = \frac{f_{ij}(r_{ij}) D_{e_{ij}}}{S_{ij} - 1} e^{-\sqrt{2S_{ij}}\beta_{ij}(r - R_{e_{ij}})}, \tag{11}$$

and

$$V_A(r_{ij}) = \frac{f_{ij}(r_{ij}) D_{e_{ij}} S_{ij}}{S_{ij} - 1} e^{-\sqrt{\frac{2}{S_{ij}}}\beta_{ij}(r - R_{e_{ij}})}. \tag{12}$$

$\bar{B}_{ij}$ is an empirical bond-order function to be described later.

The values of the well depth $D_{e_{ij}}$, the equilibrium distance $R_{e_{ij}}$, and the parameters β_{ij} and S_{ij} depend upon the type of bond between atoms i and j, i.e. $C-C$, $C=C$, $C\equiv C$, $C-H$ or $H-H$.

The cut-off function $f_{ij}(r)$ is defined as

$$f_{ij}(r) = \begin{cases} 1 & r < R1_{ij} \\ \frac{1}{2}[1 + \cos(\frac{\pi(r-R1_{ij})}{R2_{ij}-R1_{ij}})] & R1_{ij} < r < R2_{ij} \\ 0 & r > R2_{ij}. \end{cases} \quad (13)$$

Fig. 11 (a) shows a plot of the cut-off function $f_{ij}(r)$ which smoothly cuts off the interaction between atoms i and j when their distance is greater than $R1_{ij}$. The cut-off ranges $R1_{ij}$ and $R2_{ij}$ are also determined by type of bond between atoms i and j.

The empirical bond-order function $\bar{B}_{ij}$ is given by the average of many-body couplings B_{ij} and B_{ji}, and a term associated with a correction for a bond belonging to a conjugated system (If any neighbors are carbon atoms that have a coordination of less than four ($N_{t_i} < 4$), the bond is defined as being part of a conjugated system.):

$$\bar{B}_{ij} = \frac{B_{ij} + B_{ji}}{2} + \frac{F_{ij}(N_{t_i}, N_{t_j}, N_{conj_{ij}})}{2}, \quad (14)$$

where B_{ij} and B_{ji} are many-body coupling terms between the bonds $i-j$ and $i-k$, as well as $j-i$ and $j-k$ where k represents many-body contribution due to other neighboring carbons (see Fig. 12 (a) and Eq. (15) below). The second term of Eq. (14), $F_{ij}(N_{t_i}, N_{t_j}, N_{conj_{ij}})$, the correction for a conjugated system, is used for carbon-carbon bonds only (both i and j are carbons). Otherwise, $F_{CH}(N_{t_i}, N_{t_j}, N_{conj_{ij}}) = F_{HC}(N_{t_i}, N_{t_j}, N_{conj_{ij}}) = F_{HH}(N_{t_i}, N_{t_j}, N_{conj_{ij}}) = 0$. The arguments N_{t_i} and N_{t_j} are the total numbers of neighboring atoms for carbon atoms i and j, respectively. The argument $N_{conj_{ij}}$ is the total number of neighboring carbon atoms for both i and j atoms. The method of counting these neighbors will be given later.

The quantities of B_{ij} and B_{ji} are given as

$$B_{ij} = [1 + \sum_{k(\neq i,j)} G_i(\theta_{ijk}) f_{ik}(r_{ik}) e^{\alpha_{ijk}[(r_{ij}-R_{e_{ij}})-(r_{ik}-R_{e_{ik}})]} + H_{ij}(N_{h_i} N_{c_i})]^{-\delta_i} \quad (15)$$

and,

$$B_{ji} = [1 + \sum_{k(\neq j,i)} G_j(\theta_{jik}) f_{jk}(r_{jk}) e^{\alpha_{jik}[(r_{ji}-R_{e_{ji}})-(r_{jk}-R_{e_{jk}})]} + H_{ji}(N_{h_j} N_{c_j})]^{-\delta_j}, \quad (16)$$

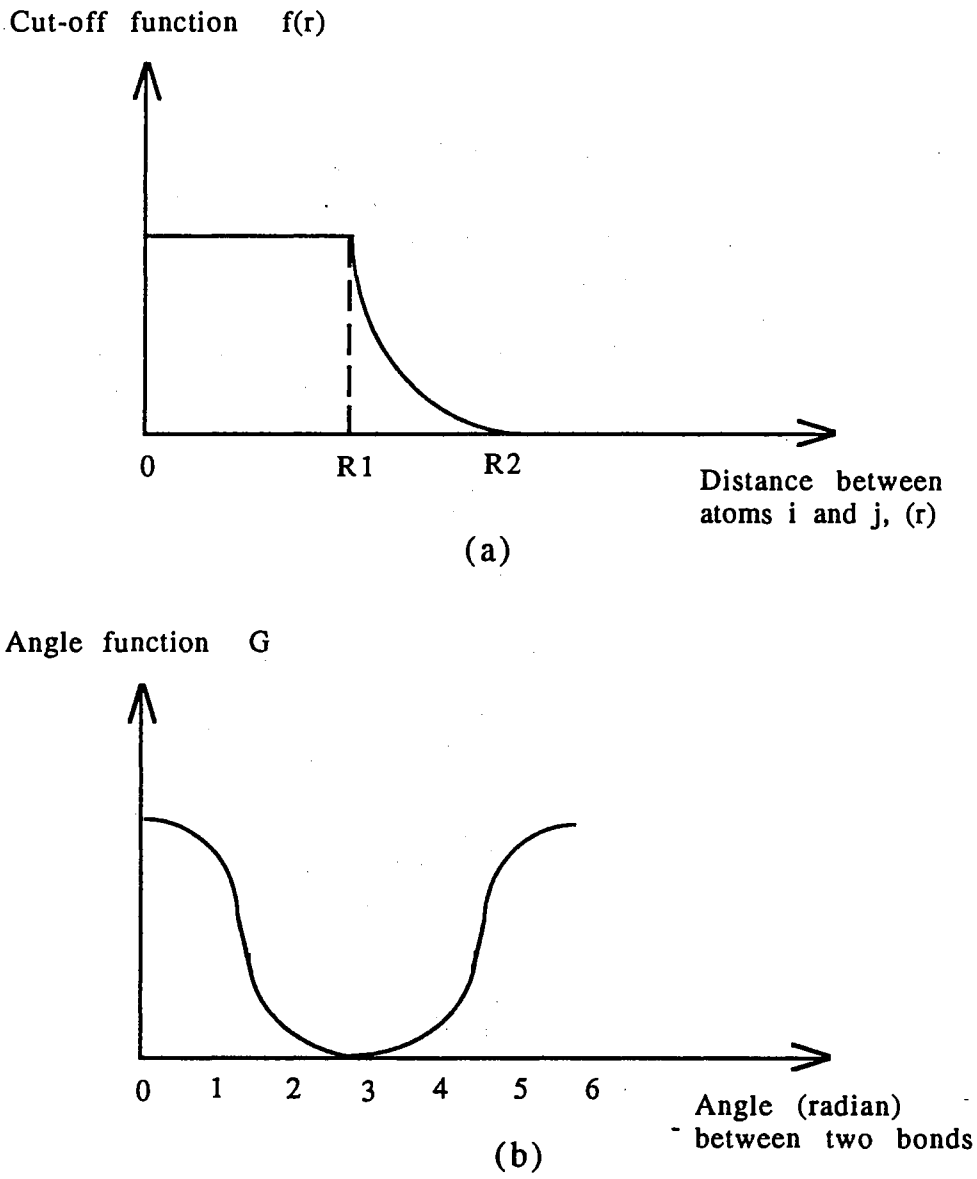

Figure 11. Plots of (a) the cut-off function $f_{ij}(r)$, and (b) $G_C(\theta)$ as a function of θ used by the Brenner empirical potential energy function.

where G_i and G_j are the functions of angles to be defined below.

Fig. 12 (a) shows that for a carbon atom i and its nearest neighbor atoms j and k (j and k could be either carbon or hydrogen), the angle θ_{ijk} is defined between bonds $i-j$ and $i-k$ (Fig. 12 (a)). For carbon atom j and its nearest neighbor atoms i and k (i and k could be either carbon or hydrogen), the angle θ_{jik} is defined between bonds $j-i$ and $j-k$ (Fig. 12 (a)). Both θ_{ijk} and θ_{jik} could be either $\theta_{CCC}, \theta_{CCH}, \theta_{CHC}$ or θ_{CHH}. The functions $G_i(\theta_{ijk})$ and $G_j(\theta_{jik})$ are defined by

$$G_C(\theta_{ijk}) = a_o \left[1 + \frac{c_o^2}{d_o^2} - \frac{c_o^2}{(d_o^2 + (1 + \cos(\theta_{ijk}))^2}\right] \tag{17}$$

and

$$G_C(\theta_{jik}) = a_o \left[1 + \frac{c_o^2}{d_o^2} - \frac{c_o^2}{(d_o^2 + (1 + \cos(\theta_{jik}))^2}\right], \tag{18}$$

where the values of parameters c_o and d_o vary with different sets of potentials. $G_C(\theta)$ as a function of θ is plotted in Fig. 11 (b). If atom i is hydrogen, the function $G_i(\theta_{ijk})$ is zero. Similarly, if j is a hydrogen atom $G_j(\theta_{jik})$ is equal to zero.

For counting neighboring hydrogen bonds N_{h_i} and neighboring carbon bonds N_{c_i} of atom i, the bond $i-j$ should not be included when we count all possible neighboring-bonds of i. The neighboring bonds are determined by cut-off functions $f_{im}(r_{im})$ and $f_{in}(r_{in})$ given by Eq. (13). Here, m runs over all neighboring hydrogen bonds, and n runs over all neighboring carbon bonds. The quantities N_{h_i}, N_{c_i} and total number of neighboring bonds N_{t_i} of atom i are given, respectively, by

$$N_{h_i} = \sum_{hydrogen(m \neq i,j)} f_{im}(r_{im}), \tag{19}$$

$$N_{c_i} = \sum_{carbon(n \neq i,j)} f_{in}(r_{in}), \tag{20}$$

and

$$N_{t_i} = N_{h_i} + N_{c_i}. \tag{21}$$

Fig. 12 (b) shows a pictorial description of method used to count neighboring bonds for atom i except bond $i-j$. Similar methods are used to determine N_{h_j}, N_{c_j} in Eq. (16), and N_{t_j} in Eq. (14).

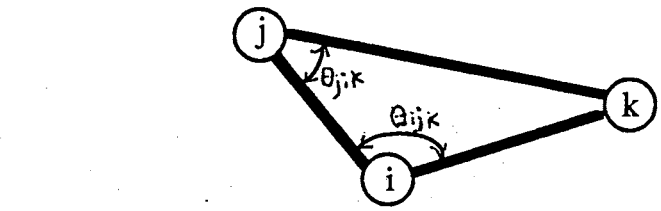

(a)

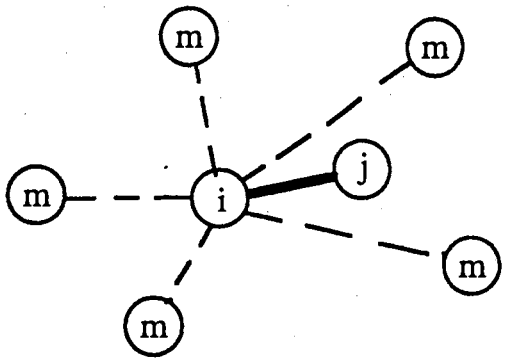

(b)

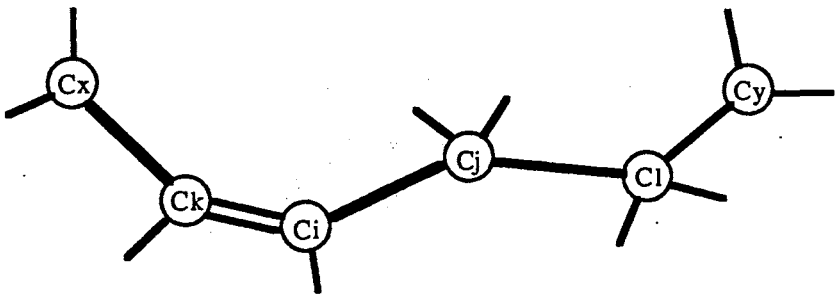

(c)

Figure 12. Pictorial description of terms which contribute to the Brenner energy function (a) definition of angles θ_{ijk} between bonds $i-j$ and $i-k$ and θ_{jik} between bonds $j-i$ and $j-k$, respectively. Atoms i, j and k could be either carbon or hydrogen; (b) atoms m are neighboring-bonds of atom i, excluding bond $i-j$; (c) a conjugated system

If any neighbors are carbon atoms that have a coordination of less than four ($N_{t_i} < 4$), the bond is defined as being part of a conjugated system. The value of $N_{conj_{ij}}$ is determined by

$$N_{conj_{ij}} = 1 + \sum_{carbon(k \neq C_i, C_j)} f_{ik}(r_{ik}) FF(xx_{ik}) + \sum_{carbon(l \neq C_i, C_j)} f_{jl}(r_{jl}) FF(xx_{jl}). \quad (22)$$

where the sum over k runs over all possible neighboring carbon bonds of carbon i except bond $i-j$, whereas the sum over l runs over all possible neighboring carbon bonds of carbon j except bond $j-i$; The quantities xx_{ik} represent the number of possible neighboring carbon bonds of carbons k except bond $i-k$. Fig. 12 (c) illustrates the situations discussed above. The quantity xx_{ik} is defined by

$$xx_{ik} = N_{t_k} - f_{ik}(r_{ik}), \quad (23)$$

The values of functions $FF(xx_{ik})$ and $FF(xx_{jl})$ are given, respectively,

$$FF(xx_{ik}) = \begin{cases} 1 & xx_{ik} \leq 2 \\ \frac{1}{2}[1 + \cos(\pi(xx_{ik} - 2))] & 2 < xx_{ik} < 3 \\ 0 & xx_{ik} \geq 3, \end{cases} \quad (24)$$

$$FF(xx_{jl}) = \begin{cases} 1 & xx_{jl} \leq 2 \\ \frac{1}{2}[1 + \cos(\pi(xx_{jl} - 2))] & 2 < xx_{jl} < 3 \\ 0 & xx_{jl} \geq 3. \end{cases} \quad (25)$$

Two sets of parameters, potential #1 and potential #2, respectively, were constructed by Brenner and tested extensively against known energies of atomization for hydrocarbons [118]. We have used Brenner potential #2 (TABLE I and II) to simulate the interaction of hydrogen, C_2H_2 and C_2H with a $C(111)$ substrate. All parameters not listed in the Tables are set equal to zero. For instance, $F(2,1,3) = 0$ since it is not listed in TABLE I and II. According to Brenner potential #2, the lengths of bonds are given as: $b_{singlebond} = 1.55$ Å, $b_{doublebond} = 1.38$ Å, and $b_{triplebond} = 1.29$ Å.

In our simulation studies, the Brenner energy calculation subroutine was written as an external file, $E\_Brenn()$. $E\_Brenn()$ can work independently for

TABLE I.

PARAMETERS FOR BRENNER POTENTIAL #2
(PART 1)[118]

Atoms (i,j)	Parameter	Value
Carbons	$R1_{CC}$	1.7 $\AA$
	$R2_{CC}$	2.0 $\AA$
	$R_{e_{CC}}$	1.39 $\AA$
	$D_{e_{CC}}$	6.0 eV
	β_{CC}	2.1 $\AA^{-1}$
	S_{CC}	1.22
	δ_{CC}	0.5
	α_{CCC}	0.0
	a_o	0.000208
	c_o	330
	d_o	3.5
Hydrogen	$R1_{HH}$	1.1 $\AA$
	$R2_{HH}$	1.7 $\AA$
	$R_{e_{HH}}$	0.7414 $\AA$
	$D_{e_{HH}}$	4.7509 eV
	β_{HH}	1.9436 $\AA^{-1}$
	S_{HH}	2.3432
	δ_{HH}	0.5
	α_{HHH}	4.0 $\AA^{-1}$
Hydrocarbons	$R1_{CH}$	1.3 $\AA$
	$R2_{CH}$	1.8 $\AA$
	$R_{e_{CH}}$	1.1199 $\AA$
	$D_{e_{CH}}$	3.6422 eV
	β_{CH}	1.9583 $\AA^{-1}$
	S_{CH}	1.6907
	δ_{CH}	0.5
	$\alpha_{CHH}, \alpha_{HCH}, \alpha_{HHC}$	4.0 $\AA^{-1}$
	$\alpha_{CCH}, \alpha_{CHC}, \alpha_{HCC}$	4.0 $\AA^{-1}$

TABLE II.

PARAMETERS FOR BRENNER POTENTIAL #2
(PART 2)[118]

Atoms (i,j)	Parameter	Value
Carbons	$H_{CC}(1,1)$	-0.0226
	$H_{CC}(2,0)$	-0.0061
	$H_{CC}(3,0)$	0.0173
	$H_{CC}(1,2)$	0.0149
	$H_{CC}(2,1)$	0.0160
Hydrocarbons	$H_{CH}(1,0)$	-0.0984
	$H_{CH}(2,0)$	-0.2878
	$H_{CH}(3,0)$	-0.4507
	$H_{CH}(0,1)$	-0.2479
	$H_{CH}(0,2)$	-0.3221
	$H_{CH}(0,3)$	-0.4460
	$H_{CH}(1,1)$	-0.3344
	$H_{CH}(2,1)$	-0.4438
	$H_{CH}(1,2)$	-0.4449
Carbons	F(2,3,1)	-0.0363
	F(3,2,1)	-0.0363
	F(2,3,2)	-0.0363
	F(3,2,2)	-0.0363
	F(1,2,2)	-0.0243
	F(2,1,2)	-0.0243
	F(1,3,1)	-0.0903
	F(3,1,1)	-0.0903
	F(1,3,2)	-0.0903
	F(3,1,2)	-0.0903
	F(0,3,1)	-0.0904
	F(3,0,1)	-0.0904
	F(0,3,2)	-0.0904
	F(3,0,2)	-0.0904
	F(1,1,1)	0.1264
	F(2,2,1)	0.0605
	F(1,2,1)	0.0120
	F(2,1,1)	0.0120
	F(0,2,2)	-0.0269
	F(2,0,2)	-0.0269
	F(0,2,1)	0.0427
	F(2,0,1)	0.0427
	F(0,1,1)	0.0996
	F(1,0,1)	0.0996

any hydrocarbon molecule (or structure). For example, we can calculate the binding energy of a carbon $C(i)$ with any hydrocarbon structure, shown in Fig. 13, by calling subroutine *E_Brenn*() for given three dimensional coordinates. As soon as *E_Brenn*() receives the coordinates of $C(i)$, all neighbors are counted (in subroutine *More_neighb*()), and bond types are identified. Then, depending on the bond type, subroutine *E_ij_CC*() or *E_ij_HH*() (inside *E_Brenn*()) is used to find angles between all bonds (using subroutine *Thetaijk*()), and to count $N_{h_i}, N_{c_i}, N_{t_i}, N_{t_j}, N_{t_{kx}}, N_{t_{ly}}, xx_{ik}$, and xx_{jl} (using subroutine *More_neighb*()). For a conjugated system, $N_{conj_{ij}}$ is calculated in subroutine *Conj_sum*(). The second terms of Eq. (15) and Eq. (16) are calculated in subroutines *Sumijk_ccc*(), *Sumijk_cch*(), *Sumijk_chc*(), and *Sumijk_chh*(). Because the angle function $G_H(\theta)$ equals zero (see the paragraph about Eq. (17) or Eq. (18)), *Sumijk_hcc*(), *Sumijk_hch*(), *Sumijk_hhc*(), and *Sumijk_hhh*() are zero. For the calculation of B_{ji}, the same subroutines are used, exchanging arguments Cj with Ci. Further, for given $C(i)$, each repulsive and attractive pair (i, j), shown in Eq. (11) and Eq. (12), are calculated in subroutines *E_Bren_ijcc*() and *E_Bren_ijch*(). Finally, summing over $C(i) - C$ and $C(i) - H$ bonds gives the binding energy of $C(i)$ with other hydrocarbons.

We have computed some single hydrocarbon molecules and radicals using subroutine *E_Brenn*() in attempt to ensure that our energy calculation in our model is correct. Our results are compared to Brenner's published calculations and to experiment in TABLE III.

2-3 Major Chemical Reactions included in Molecular Modeling

As mentioned in Chapter I, Huang, Frenklach and Maroncelli (HFM) [71] [69] have proposed that the main monomer growth species is acetylene C_2H_2, and the reaction mechanism consists of two alternating steps: (1) surface activation by H atom abstraction of a surface carbon, and (2) the addition of one or more acetylene molecules. Peploski, Thompson and Raff [73] also suggested that addition of a ethynyl radical C_2H to a chemisorbed acetylene group proceeds with a much higher

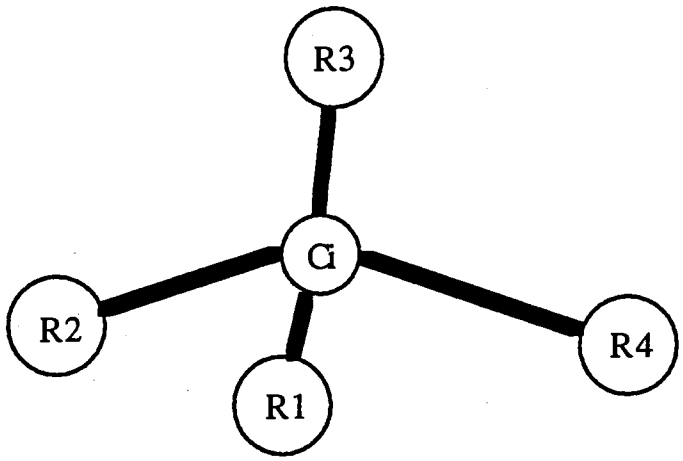

Figure 13. Pictorial description of terms which contribution to the Brenner energy calculation, in subroutine $E\_Brenn()$. Binding energy of $C(i)$ with any hydrocarbon radicals R can be calculated by $E\_Brenn()$

TABLE III.

ENERGY CALCULATION COMPARISON OF OUR RESULTS WITH BRENNER'S RESULTS AND WITH EXPERIMENTAL DATA

Hydrocarbons	Energy (eV)		
	Our results	Brenner's calculation	Experimental results
acetylene (C_2H_2)	17.135	17.1	17.1
methane (CH_4)	17.540	17.6	17.6
ethylene (C_2H_4)	23.605	23.6	23.6
methyl (CH_3)	12.704	12.7	12.7

probability than is the case for C_2H_2. Based on this result, we have considered both C_2H_2 and C_2H as reactants which can deposit on the diamond surface. The main chemical reactions in our simulation are:

- Atomic Hydrogen Reactions: Atomic hydrogen H can activate or deactivate or reactivate the diamond surface.

  1. Activation: An atomic hydrogen (H) activates the surface by abstracting an H atom from surface species $C_s - R$, and produces a radical site.

$$C_sH + H \longrightarrow \dot{C}_s + H_2 \tag{26}$$

$$C_s - CH = CH_2 + H \longrightarrow C_s - CH = \dot{C}H + H_2 \tag{27}$$

$$C_s - C \equiv CH + H \longrightarrow C_s - CH = \dot{C}H \tag{28}$$

  2. Deactivation: An atomic hydrogen (H) deactivates the surface by adding an H atom to surface species $C_s - R$ (or by changing the bond type), and obliterating a radical site.

$$\dot{C}_s + H \longrightarrow C_sH \tag{29}$$

$$C_s - CH = \dot{C}H + H \longrightarrow C_s - CH = CH_2 \tag{30}$$

$$C_s - CH = \dot{C}H + H \longrightarrow C_s - C \equiv CH + H_2 \tag{31}$$

$$C_s - CH = \dot{C}H \longrightarrow C_s - C \equiv CH + H \tag{32}$$

3. Reactivation: An atomic hydrogen (H) reactivates the surface by creating a radical site at a carbon bonded to the surface.

$$C_s - C \equiv CH + H \longrightarrow C_s - \dot{C} = CH_2 \quad (33)$$

$$C_s - CH = CH_2 + H \longrightarrow C_s - \dot{C}H - CH_3 \quad (34)$$

$$C_s - CH = CH_2 + H \longrightarrow C_s - \dot{C} = CH_2 + H_2 \quad (35)$$

- Chemisorption and desorption of C_2H_2 and C_2H on the diamond surface.

1. Chemisorption of C_2H_2 and C_2H to the $C(111)$ surface.

$$\dot{C}_s + CH \equiv CH \longrightarrow C_s - CH = \dot{C}H \quad (36)$$

$$C_s - CH = \dot{C}H + CH \equiv CH \longrightarrow C_s - CH = CH - CH = \dot{C}H \quad (37)$$

$$C_s - \dot{C} = CH_2 + CH \equiv CH \longrightarrow C_s - C(CH = \dot{C}H)H = CH_2 \quad (38)$$

$$\dot{C}_s + \dot{C} \equiv CH \longrightarrow C_s - \dot{C} = \dot{C}H \quad (39)$$

$$C_s - CH = \dot{C}H + \dot{C} \equiv CH \longrightarrow C_s - CH = CH - \dot{C} = \dot{C}H \quad (40)$$

$$C_s - \dot{C} = CH_2 + \dot{C} \equiv CH \longrightarrow C_s - C(\dot{C} = \dot{C}H) = CH_2 \quad (41)$$

2. Desorption of $CH = \dot{C}H$ from the $C(111)$ surface.

$$C_s - CH = \dot{C}H \longrightarrow \dot{C}_s + CH \equiv CH \quad (42)$$

$$C_s - CH = CH - CH = \dot{C}H \longrightarrow C_s - CH = \dot{C}H + CH \equiv CH \quad (43)$$

$$C_s - C(CH = \dot{C}H)H = CH_2 \longrightarrow C_s - \dot{C} = CH_2 + CH \equiv CH \quad (44)$$

$$C_s - \dot{C} = \dot{C}H \longrightarrow \dot{C}_s + \dot{C} \equiv CH \quad (45)$$

$$C_s - CH = CH - \dot{C} = \dot{C}H \longrightarrow C_s - CH = \dot{C}H + \dot{C} \equiv CH \quad (46)$$

$$C_s - C(\dot{C} = \dot{C}H)H = CH_2 \longrightarrow C_s - \dot{C} = CH_2 + \dot{C} \equiv CH \quad (47)$$

- Formation of tetrahedrons at the $C(111)$ surface from following situations.

1. For one $(-C = C-)$ dimer

$$C_{s_1} - \dot{C} = CH_2 + \dot{C}_{s_2} \longrightarrow C_{s_1} - \dot{C}(C_{s_2}) - \dot{C}H_2 \tag{48}$$

2. For two $(-C = C-)$ dimers in parallel (see the definition and explanation in detail in chapter III)

$$C_{s_1}-CH = \dot{C}H + C_{s_2}-\dot{C} = CH_2 \longrightarrow C_{s_1}-\dot{C}H-\dot{C}H-\dot{C}(C_{s_2})-\dot{C}H_2 \tag{49}$$

3. For two $(-C = C-)$ dimers in series (see the definition and explanation in detail in chapter III)

$$C_{s_1}-CH = \dot{C}-CH = H_2 + \dot{C}_{s_2} \longrightarrow C_{s_1}-\dot{C}H-\dot{C}(C_{s_2})H-\dot{C}H-\dot{C}H_2. \tag{50}$$

The main chemical reactions used in our simulation for diamond film growth from a $C(111)$ surface by chemical vapor deposition of an oxy/acetylene flame have been listed above. The probability of each reaction, governed by Brenner energy difference, within the Kawasaki dynamical Monte Carlo algorithm produced the results to be described in the next chapter.

CHAPTER III

METHODS

This research is a simulation of 3-dimensional diamond film growth by chemical vapor deposition on a $C(111)$ diamond surface with two different sizes of substrates (200 carbons and 512 carbons, respectively). In this chapter the numerical methods used in the simulation will be described. First, in section 3-1 the computer code flowchart will be given. Second, some special notation used in the simulation will be presented in section 3-2. Then, each step in the simulation will be described in detail in sections 3-3 - sections 3-10. Finally, computer run procedures will be summarized in section 3-11.

3-1 Computer Code Flowchart

The flowchart of the computer program, which includes four external files, is shown in Fig. 14. The four external subprograms and their structures are shown in the following figures: (1) Fig. 15 shows the subprogram *fdepos.c* that was used for hydrogen abstraction and addition, and acetylene deposition on $C(111)$ diamond surface; (2) Fig. 16 shows the subprogram *ftetra.c* that was used for tetrahedron formation at the $C(111)$ diamond surface; (3) Fig. 17 shows the subprogram *frelax.c* that was used for surface relaxation, desorption and adsorption from and to the $C(111)$ diamond surface; and (4) Fig. 18 shows the subprogram *fenerg.c* that was used for Brenner energy calculations applied to each Monte Carlo move.

A *main* program contains code for initializing the system, for the Monte Carlo loops, and for input/output. The first three subprograms were inside the Monte Carlo loops and were called directly by the main program, whereas, *fenerg.c*

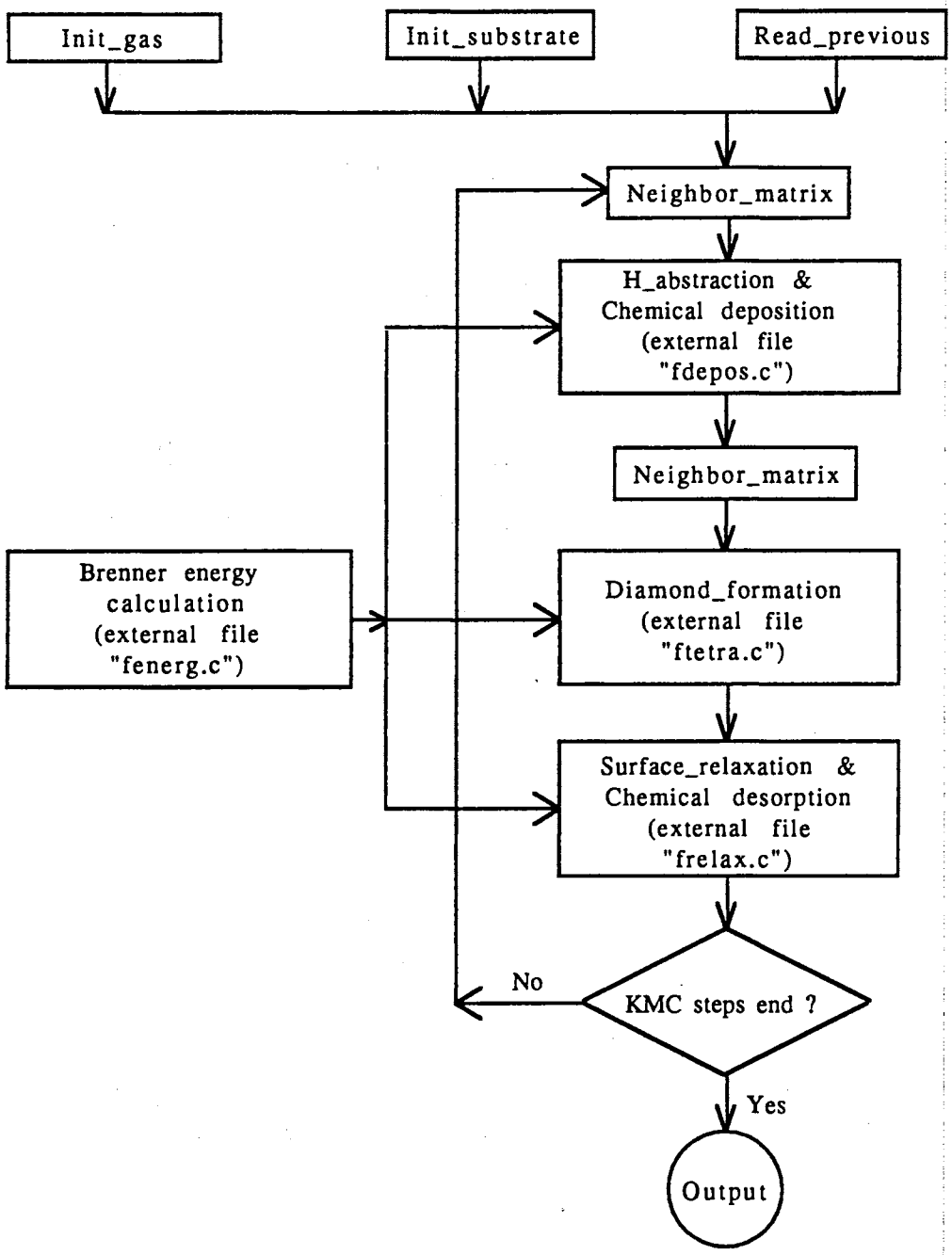

Figure 14. Computer simulation flowchart for diamond film growth by chemical vapor deposition (cvd).

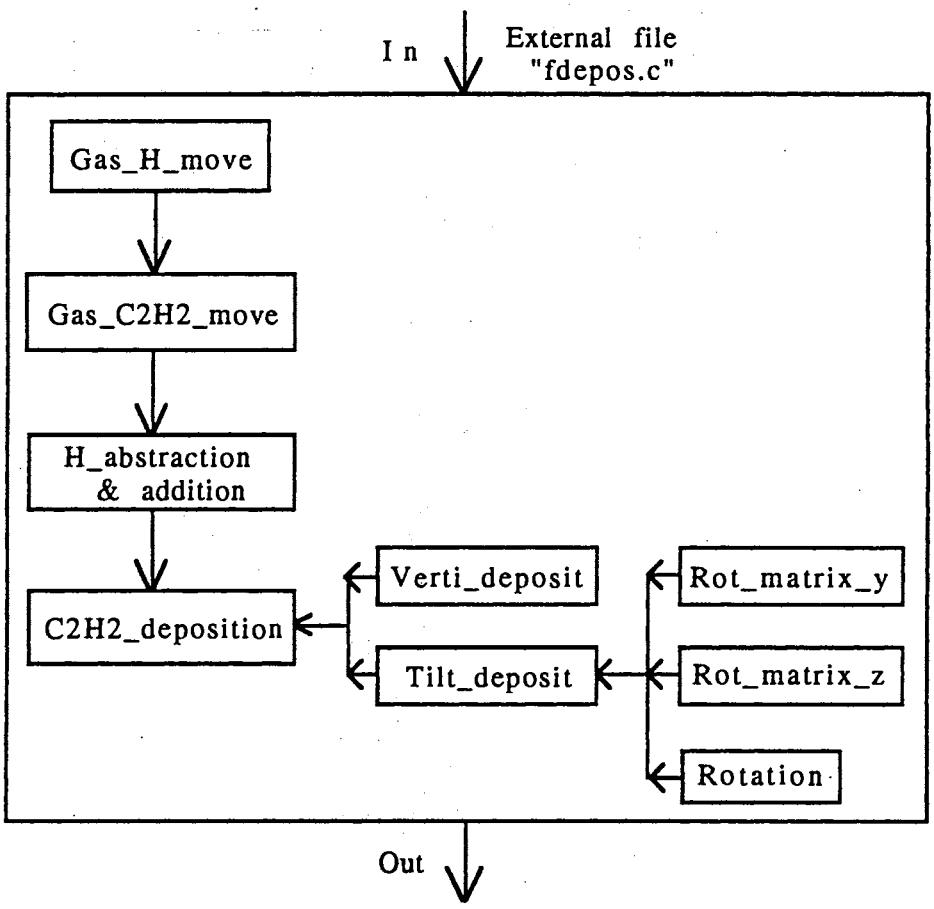

Figure 15. Subprogram *fdepos.c* was applied to the simulation of hydrogen abstraction and addition, and acetylene deposition on $C(111)$ diamond surface.

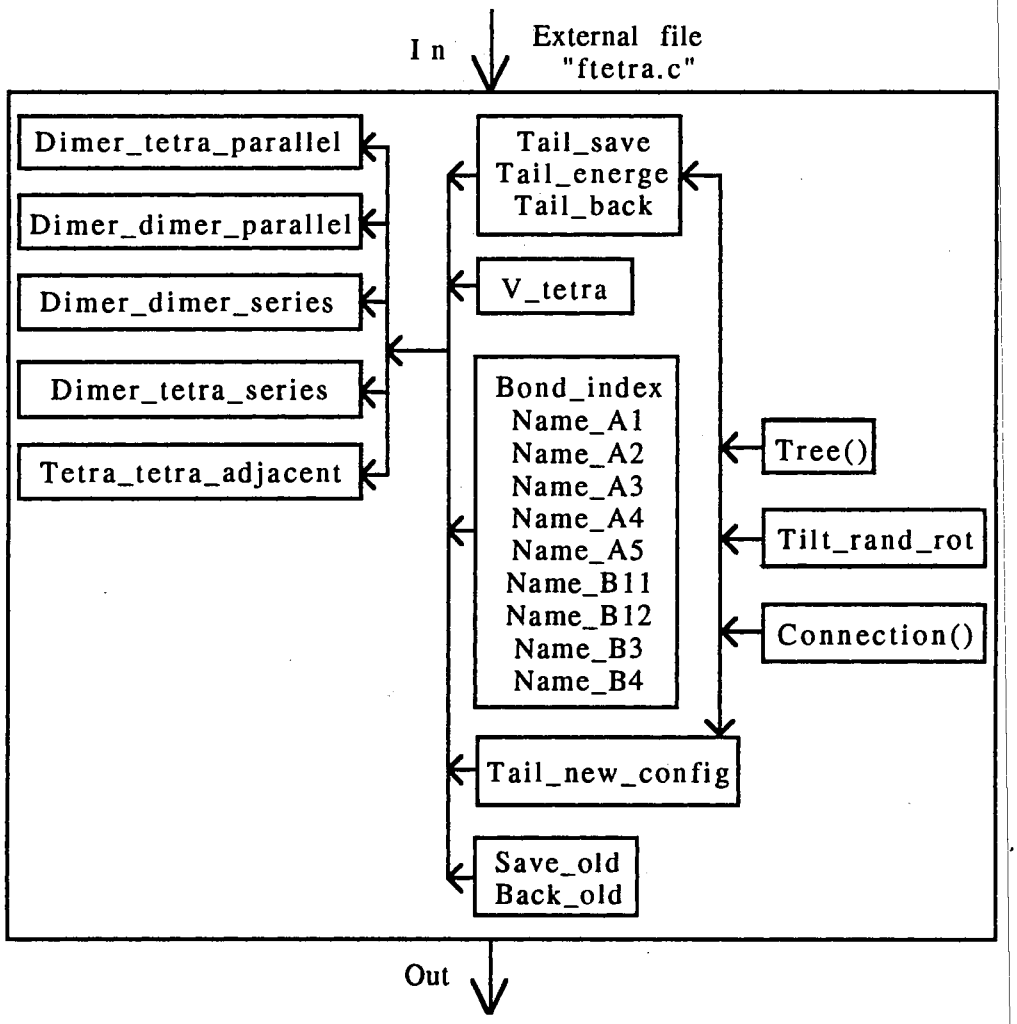

Figure 16. Subprogram *ftetra.c* was applied to the simulation of tetrahedron formation at the $C(111)$ diamond surface.

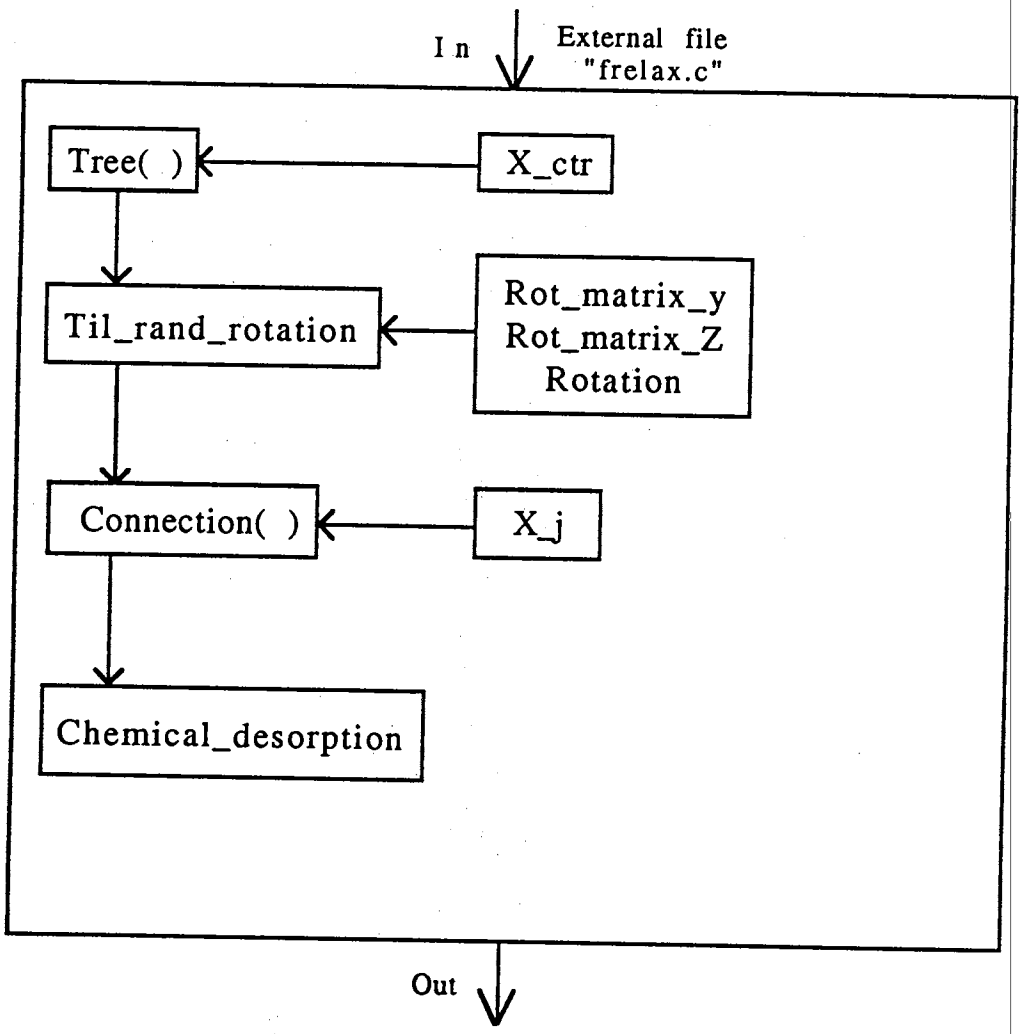

Figure 17. Subprogram *frelax.c* was applied to the simulation of surface relaxation, desorption and adsorption from and to the $C(111)$ diamond surface.

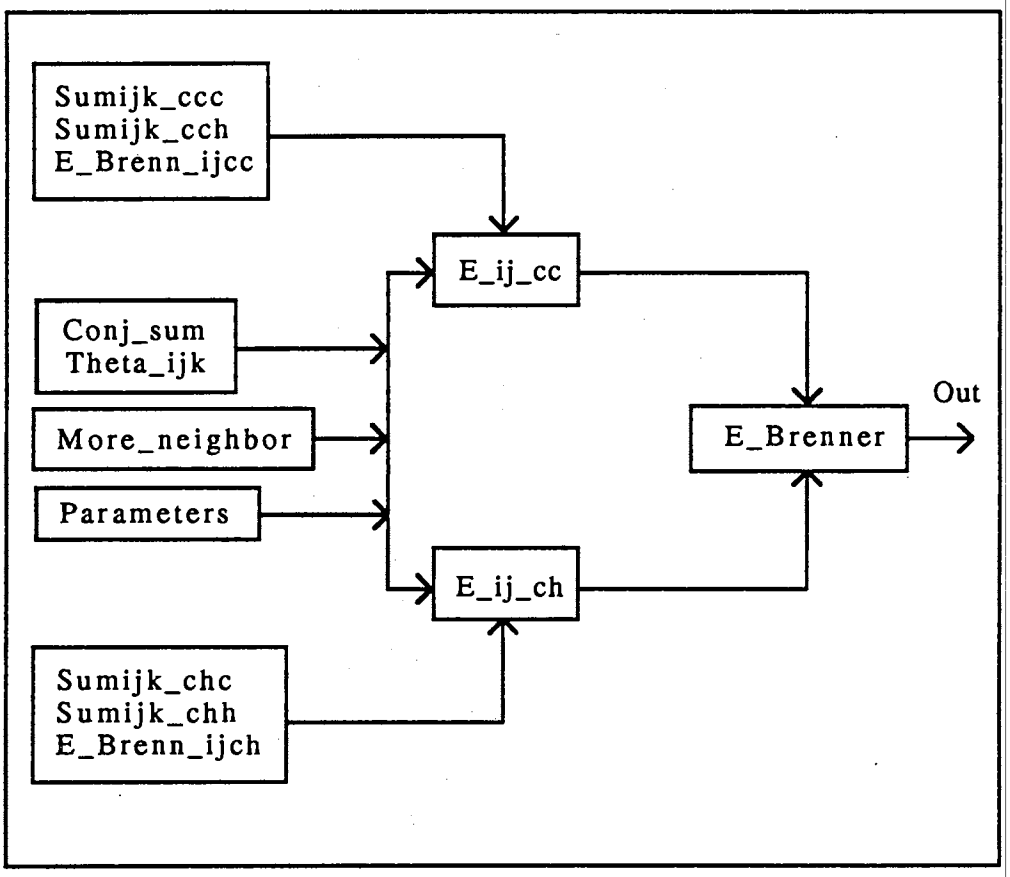

Figure 18. Subprogram *fenerg.c* carried out all Brenner energy calculations.

was called by each of the three subprograms, individually, for each Monte Carlo move. The computer code, including 53 subroutines and about 7,000 lines of code, were written in the C computing language. The various steps, shown from Fig. 14 through Fig. 18, will now be described in detail.

3-2 Special Notations in the Simulation

Because Monte Carlo moves are totally random, hydrogen activation, deactivation and reactivation, acetylene deposition, desorption and adsorption, and surface relaxation could occur at any where on or near the surface. For this reason, when we randomly pick any carbon or bond, we need information about its location, number of neighbors, the types of bonds, and direction cosines of each bond. Thus, we have introduced special notations in our simulation.

- Position of carbon: array has been used to locate carbon i, i.e. $CP[x, y, z][i]$.
- Type of bond: Since there are at most four possible bonds for each carbon, we use an array $C\_bonds[1, 2, 3, 4][i]$, to denote four bond-indices of carbon i. There are four bond types between carbon i and its neighbors, including carbon-carbon single bonds $(C - C)$, carbon-carbon double bonds $(C = C)$, carbon-carbon triple bonds $(C \equiv C)$, and carbon-hydrogen bonds $(C - H)$. A fifth possibility case is the carbon radical $(\dot{C}_i)$, i.e. a carbon atom with "dangling" bond. Finally, for double and triple carbon bonds, $C = C$ and $C \equiv C$, each carbon may only bind to two other atoms or one atom, respectively. The array $C\_bonds[1, 2, 3, 4][i]$ was defined so that the number and type of bond associated with each neighbor can be read. For instance,
  1. for $C_i \overset{k}{-} C_n$ bond, $C\_bonds[k][i] = n$ means the carbon i ($i = 0 \rightarrow 19999$) bonds to the carbon n ($n = 0 \rightarrow 19999$) via the kth bond-index (k = 1,2,3,4) of carbon i.
  2. for $C_i \overset{k}{=} C_n$ bond, $C\_bonds[k][i] = n + 20000$.
  3. for $C_i \overset{k}{\equiv} C_n$ bond, $C\_bonds[k][i] = n + 30000$.
  4. for $C_i \overset{k}{-} H$ bond, $C\_bonds[k][i] = 50000$.

5. for $\dot{C}_i$, $C\_bonds[k][i] = i$, which means the kth bond of the carbon i is unpaired.

6. for the case of no bond, $C\_bonds[k][i] = -1$, which means the kth bond of the carbon i does not exist, and the carbon i is not tetrahedrally coordinated.

- Bond vectors: the $V\_bond[x, y, z][1, 2, 3, 4][i]$ is used to define the lengths and directions of four bond vectors of carbon i.

3-3 Initialization of Substrate and Gas Phase

As shown in the flowchart (Fig. 14), We first initialized both substrate and gas phase. Two different sizes of substrates were tested in this research. For brevity, only one of them will be described in detail.

A substrate consisting of 512 carbons (16 carbons $\times$ 16 carbons $\times$ 2) in a diamond (111) lattice geometry was generated. Fig. 19 shows part of the lattice from (a) a top view, and (b) a sideview. All carbons in the substrate were tetrahedrally coordinated with a bond length of 1.55 Å for $C - C$, and 1.09 Å for $C - H$. The angle between any two bonds was 109°28′. The position of each carbon and their bond vectors are described in the Cartesian coordinates. A clean surface was created with the top dangling bonds of $C(111)$ diamond surface (pointing in the Z direction).

In the gas phase, six acetylenes and six atomic hydrogens were initially generated at the height of 50 Å over the substrate. This height was adjusted upward as the diamond surface grow. Fig. 20 illustrates the positions of the gaseous species. (a) From a top view, the gaseous species were arranged hexagonally. The only reason for this is to ensure that initial gaseous species did not overlap each other. (b) From a sideview, the gaseous species were above the diamond surface at the height of $SIZEZ$. The reason for his is to let new gaseous species always come from the same height.

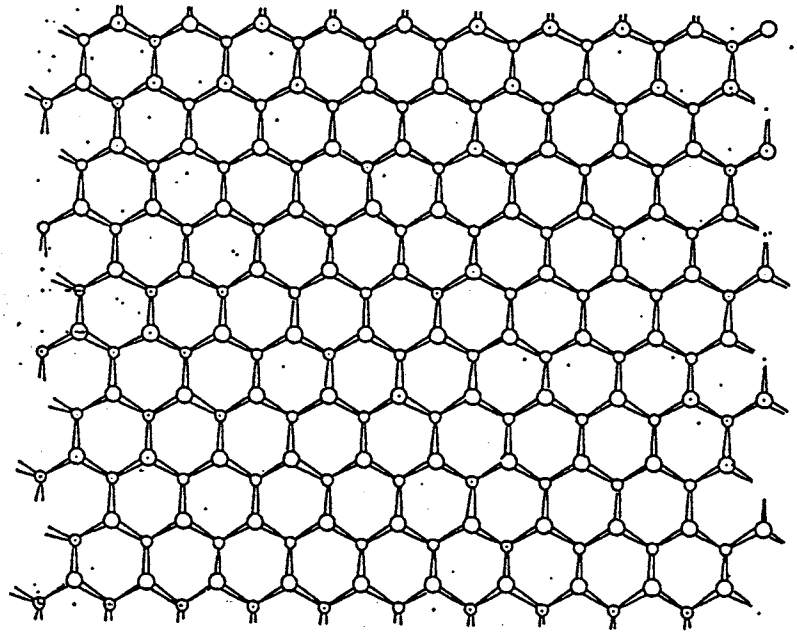

(a)

(b)

Figure 19. Initialization of substrate in (a) a top view, and (b) a sideview.

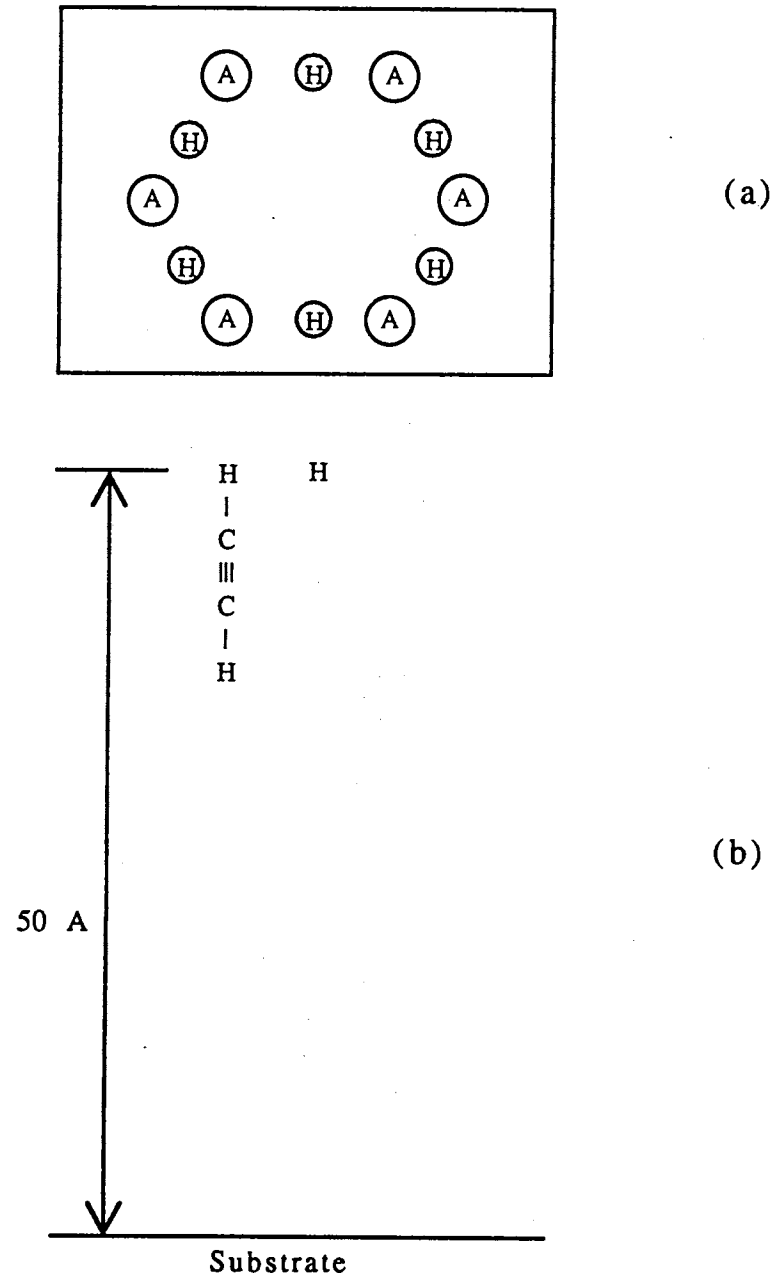

Figure 20. Initialization of gaseous species including six acetylenes and six atomic hydrogens. (a) From a top view, the gaseous species were placed in hexagon where 'A' is acetylene. (b) From a sideview, the gaseous species were about 50 Å over diamond surface.

The system was initialized for the first step. For subsequent steps, configurational data were read at the beginning of each subsequent run. It needs to be emphasized that the total number of carbon will increase continuously, and various chemical species will be created or removed through the chemical reactions described in Eqs. (26) $\rightarrow$ (48).

3-4 Boundary Conditions

Three types of boundary conditions, periodic boundary, fixed boundary and deposition boundary, have been used in this research. Fig. 21 shows those boundaries from either top-view or sideview. In Fig. 21 (a), from top-view, periodic boundary condition (PBC) were used in both X and Y directions. PBC means that the atom which moved out from a boundary of the lattices in X and Y directions is considered to move into the lattices at the opposite boundary. Let Δx, Δy and Δz be the distances between a carbon i and another carbon $j(\neq i)$. PBC in the X and Y directions means that

$$\Delta x = \begin{cases} \Delta x & \text{if } \Delta x \leq SIZEX - \Delta x \\ SIZEX - \Delta x & \text{otherwise} \end{cases} \tag{51}$$

$$\Delta y = \begin{cases} \Delta y & \text{if } \Delta y \leq SIZEY - \Delta y \\ SIZEY - \Delta y & \text{otherwise} \end{cases} \tag{52}$$

where $SIZEX$ and $SIZEY$ were the sizes of substrate in X and Y directions separately in the simulation.

In Fig. 21 (b), from a sideview, we see that fixed boundaries were considered at both top (the highest position of gaseous species) and bottom (the bottom of substrate) of the system in the Z direction. A deposition boundary was defined at the diamond surface where diamond film was growing.

3-5 Neighbor-Spheres

A neighbor list algorithm was used for energy calculation, for surface diffusion, and for relaxation moves. To save computer time two neighbor-spheres were

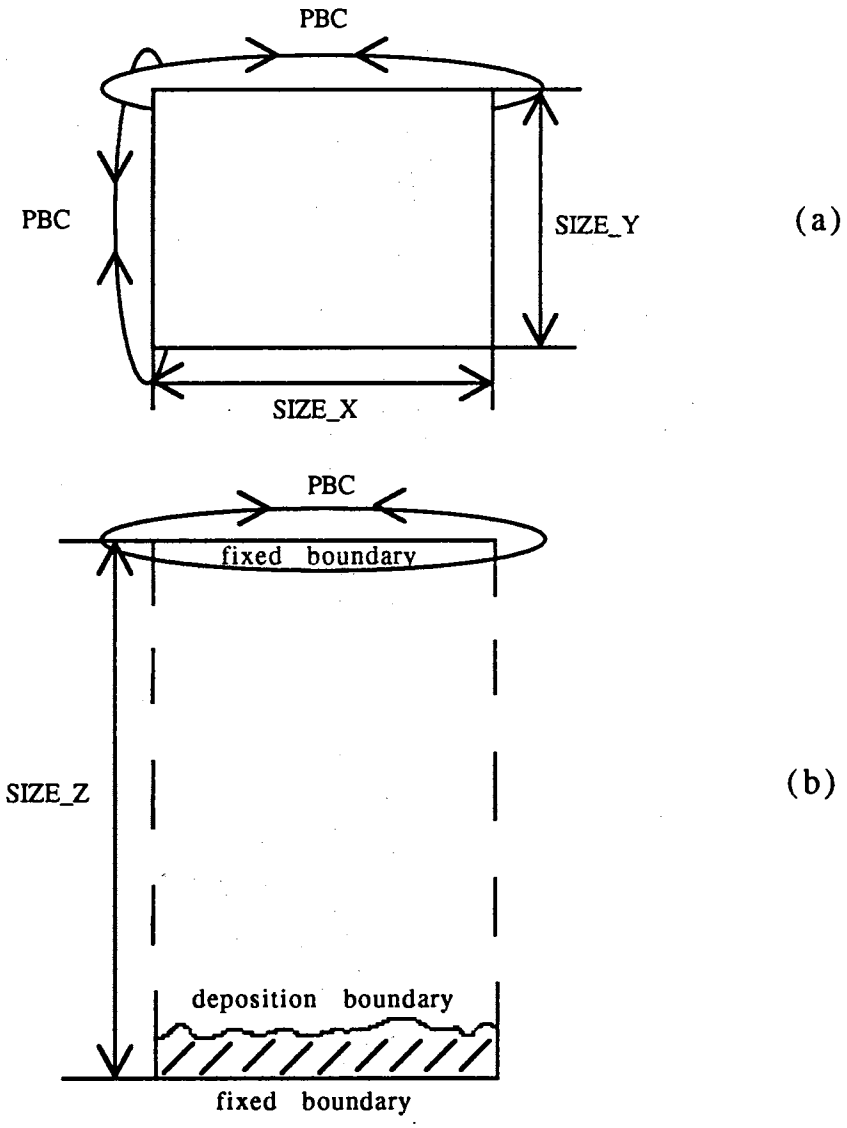

Figure 21. Boundary conditions. (a) a top-view, periodic boundary conditions (PBC) were used in both X and Y directions. (b) a sideview, fixed boundaries were imposed at both top (the highest position of gaseous species) and bottom (the bottom of substrate) of system in Z direction.

defined, with radii of 6 Å and 9 Å, respectively, to contain all nearest neighbors (NN), next nearest neighbors (NNN) or even farther neighbors (FNNN) of any carbon. The choice of the cut off range (the radii of the spheres) was based on both the ranges of Brenner potential energy and the distance of surface diffusion. Because the range of Brenner potential is very short (2 Å for carbon-carbon interaction, 1.8 Å for carbon-hydrogen interaction, and 1.7 Å for hydrogen-hydrogen interaction), the actual cut off range was determined by the distance of surface diffusion. The smaller neighbor-sphere (with radius of 6 Å) was used in calculations of energy and for surface diffusion moves. The larger neighbor-sphere (with radius of 9 Å) was used to supply (or receive) additional neighbors to (or from) the smaller neighbor-sphere when atoms moved in (or out) of the the smaller neighbor-sphere.

Let dis be the distance between carbon i and any other carbon $j(\neq i)$,

$$dis = (\Delta x)^2 + (\Delta y)^2 + (\Delta z)^2. \tag{53}$$

All neighbors, contained in a neighbor-sphere, of carbon i were given by a two dimensional neighbor matrix $neighb[k][i]$,

$$neighb[k][i] = j \quad \text{if } dis < CUT\_RANGE. \tag{54}$$

Eq. 54 means that the carbon j is the kth neighbor of carbon i if the distance between i and j is less than the cut off range. Generally, the neighbor matrix was updated every 25 Monte Carlo steps.

3-6 H-abstraction or addition

Starting from the initial position, gas phase acetylene and hydrogen were moved in a directed random walk towards the diamond surface. When vapor and surface molecules approached to within the Brenner potential cutoff distances, appropriate reactions were considered.

Initially, the $C(111)$ surface was clean (no hydrogen atoms). Therefore hydrogen addition and acetylene deposition occurred more often than hydrogen abstraction. As more and more hydrogen atoms bound to the surface, the number of

hydrogen abstraction events increased. For hydrogen and hydrocarbons the cutoff distances are 1.7 Å and 1.8 Å, respectively, (see TABLE I). Within those ranges, hydrogen abstraction or addition could occur (see the reactions of Eqs. (26) → (35)). Fig. 22 illustrates various examples of hydrogen abstraction or addition with different orientations.

3-7 C_2H_2 or C_2H Deposition

This research is a simulation of diamond film growth by oxy/acetylene flame-based deposition. As a main component of the flame, acetylene (C_2H_2) was continuously supplied to the system. At the same time, various chemical reactions occurred in the gas phase and at the diamond surface to produce chemical species such as ethynyl (C_2H) and methyl (CH_3), etc. Consequently, C_2H_2, C_2H and CH_3 should also be considered as growth species. In this research, diamond film growth based upon only C_2H_2 and C_2H deposition has been tested (see the reactions of Eqs. (36) → (41)).

In the simulation, when a C_2H_2 or C_2H approached the diamond surface within a distance of 2.0 Å, chemisorption was considered. Let C_a and C_b be any two carbons bound each other with double or triple bond, and C_s be a surface carbon with tetrahedral structure. Chemisorption consisted of breaking the $C_a \equiv C_b$ bond to produce a $C_a = C_b$ bond, and a new $C_s - C_a$ bond along the direction of the unpaired bond of the surface carbon C_s. Consequently, a species of $C_s - C_aH = \dot{C}_bH$ or $C_s - \dot{C}_aH = \dot{C}_bH$ appeared at the surface (see the reactions of Eqs. (36) → (41)). However, before any configuration changes were accepted, a total old energy E_{old} was calculated as a sum of the energies of C_s ($E_{old\_C_s}$) and C_2H_2 or C_2H ($E_{C_2H_2 or C_2H}$)

$$E_{old} = E_{old\_C_s} + E_{C_2H_2 or C_2H}. \tag{55}$$

Then, the configuration changed from old to new. Fig. 23 illustrates those changes for different C_s and various orientations, and a new energy, E_{new}, was calculated. Move were accepted or rejected via the Kawasaki algorithm described in Chapter II.

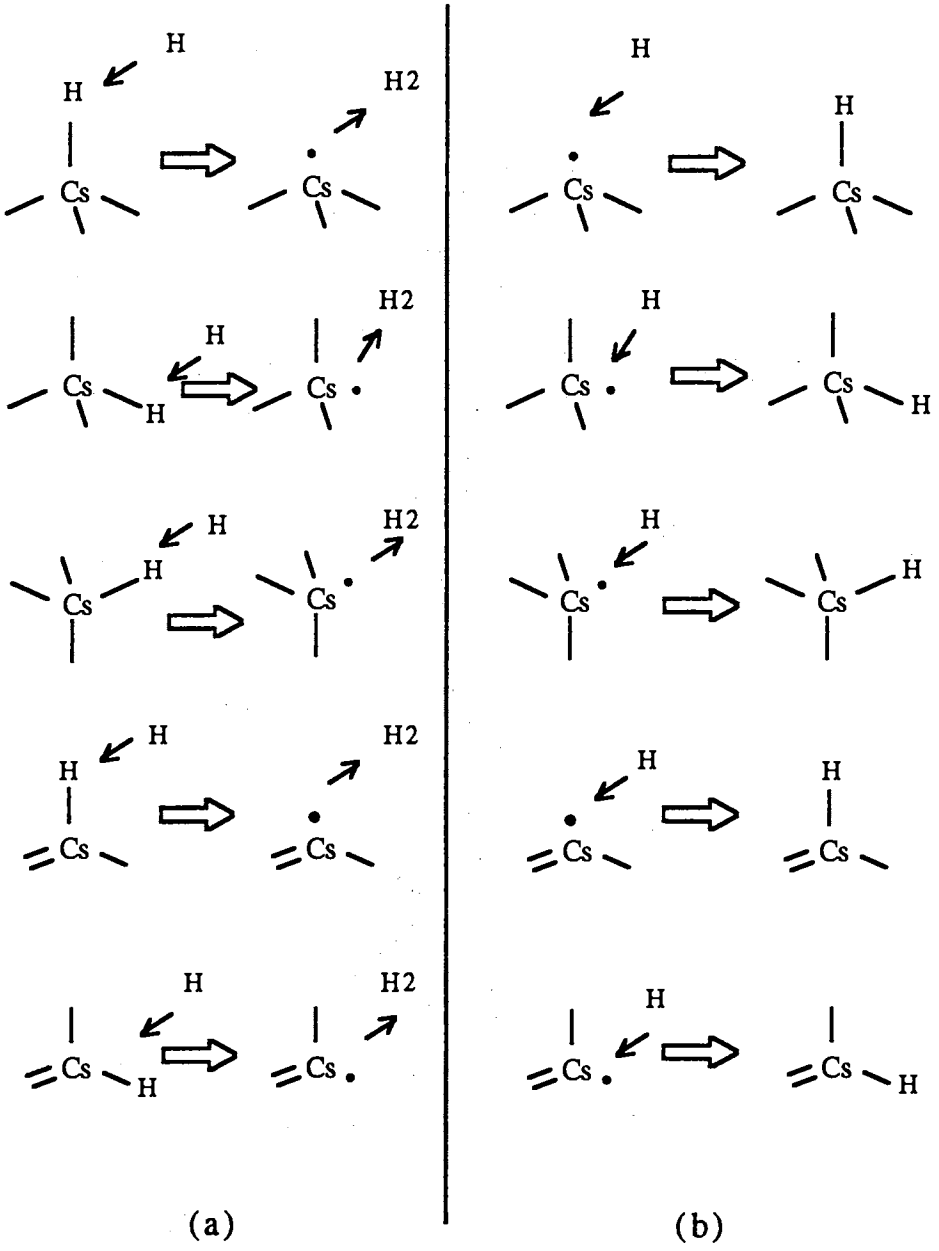

Figure 22. Hydrogen abstraction (a), and addition (b) with different orientations.

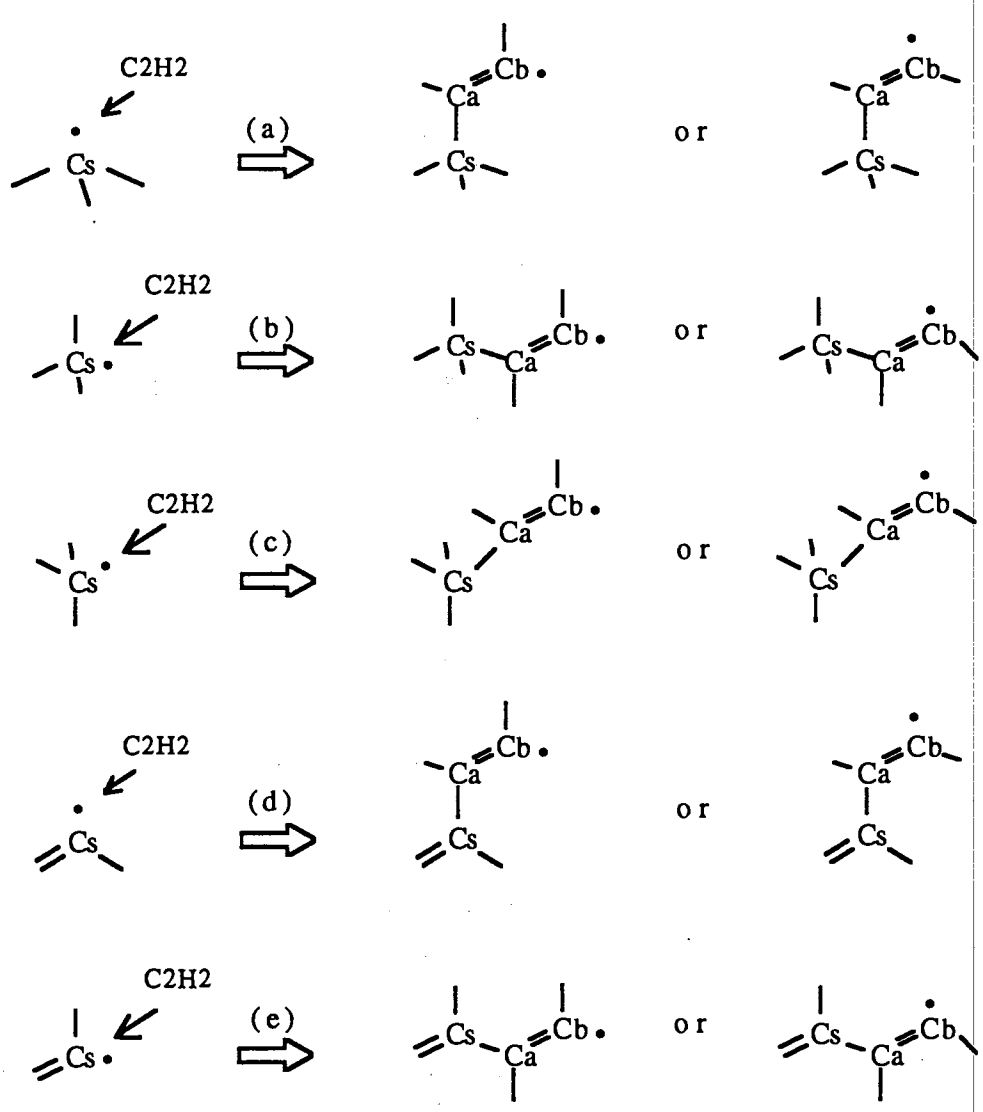

Figure 23. C_2H_2 or C_2H deposition on the surface at carbon C_s with various orientations, C_s tetrahedrally co-ordinated (a)-(c), C_s has a double bond, (d) and (e).

Practically, subroutines $Rot\_matr\_y, Rot\_matr_z, Rotation, Verti\_depos$ and $Tilt\_depos$ (see Fig. 15) were used to process the configuration change including angle calculations, bond rotation and bond formation. If the $C_s - C_a$ bond vector $\vec{r}_s$ is perpendicular to the $C(111)$ surface (Fig. 23 (a) and (d)) the position of the dimer species $C_a = C_b$ can be directly given by $Verti\_depos$ (Fig. 24 (a)). Otherwise, if $\vec{r}_s$ was tilted to $C(111)$ surface with any angle (Fig. 23 (b), (c) and (e)), the following procedure was followed to calculate the coordinates of the adsorbed dimer.

Let θ be the angle between $\vec{r}_s$ and Z axis, and ϕ be the angle between the projection of $\vec{r}_s$ on the $X - Y$ plane and X axis. θ and ϕ were computed by

$$\theta = \arccos\left(\frac{z_s}{|\vec{r}_s|}\right), \tag{56}$$

where $0 \leq \theta \leq \pi$, and

$$\phi = \arccos\left(\frac{x_s}{\sqrt{x_s^2 + y_s^2}}\right), \tag{57}$$

where $0 \leq \phi \leq \pi$. If $y_s < 0, \phi = -\phi$.

Two rotation operators Rot_matr_y and Rot_matr_z were used to process bond rotation around Y and Z axes, respectively,

$$Rot\_matr\_y = \begin{pmatrix} \cos\theta & 0 & \sin\theta \\ 0 & 1 & 0 \\ -\sin\theta & 0 & \cos\theta \end{pmatrix}, \tag{58}$$

and

$$Rot\_matr\_z = \begin{pmatrix} \cos\phi & -\sin\phi & 0 \\ \sin\phi & \cos\phi & 0 \\ 0 & 0 & 1 \end{pmatrix}. \tag{59}$$

Fig. 24 (b) illustrates the rotation procedure. Starting from a vertical position, the bond $C_s \rightarrow C_a$ rotates around the Y axis by an angle θ, and, then, rotates around the Z axis by an angle ϕ to overlap the vector $\vec{r}_s$. Consequently, the dimer species $C_a = C_b$ becomes bound to the surface carbon C_s along the direction of unpaired bond of C_s.

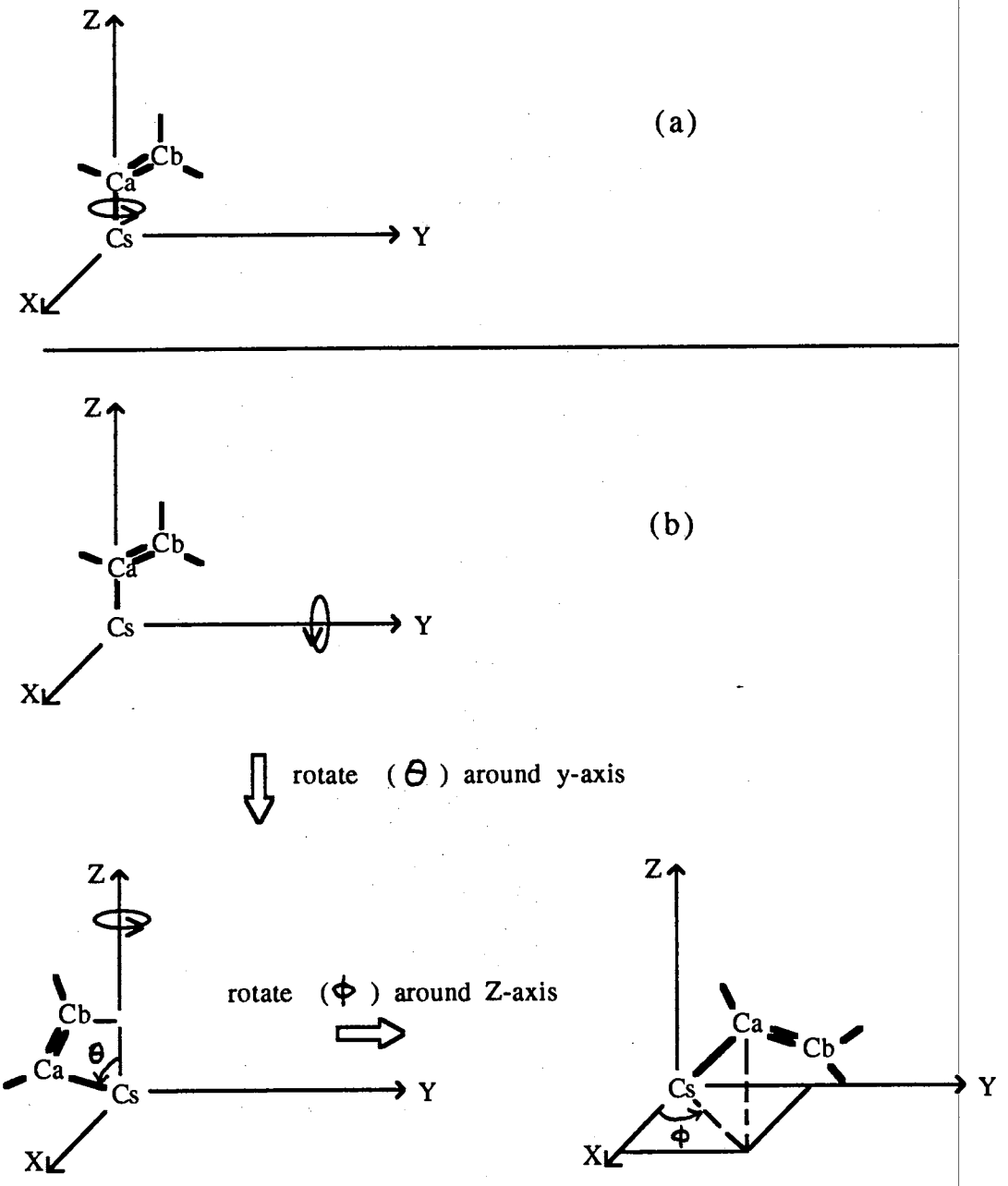

Figure 24. Pictorial description of bond rotation when the $C_s - C_a$ bond is (a) perpendicular to $C(111)$ surface, and (b) tilted to $C(111)$ surface with any angle.

3-8 Surface Diffusion to Form Tetrahedrons

As we mentioned in previous sections, hydrogen abstraction or addition, and C_2H_2 or C_2H deposition occur during a program run. As a result, surface activation or deactivation could occur any local area, and a new dimer $C_a = C_b$ could be added anywhere on the surface bonded with a surface carbon C_s along any possible direction. A snapshot of this surface growth might be shown in Fig. 25(a) which looks like some sparse, unstable trees. In point of fact, there always exists surface diffusion, local reorientation, hopping, or migration, on the surface during local thermal equilibration, and then should tend to form tetrahedral configurations that are closely packed and more stable (see Fig. 25(b)).

The method of the surface diffusion in our simulation was based on the principal of a random walk. First, a surface carbon called C_a (C_a and C_b had already deposited on the surface) was randomly picked. Two possible cases for C_a were considered:

1. C_a was connected to C_b with a double bond, $C_a = C_b$. Then, three additional possible situations were considered:

   - The $C_a = C_b$ dimer had a tetrahedron as nearest neighbor but was not connected to it. This configuration was called *one dimer and one tetrahedron in parallel* (see Fig. 26).
   - Two $C_a = C_b$ dimers were adjacent but not connected to each other. This configuration was called *two dimers in parallel* (see Fig. 27).
   - Two $C_a = C_b$ dimers connected to each other. This configuration was called *two dimers in series* (see Fig. 28).

2. C_a was a tetrahedron. Then, two additional possible situations were considered:

   - C_a had a $C_{a_2} = C_{b_2}$ dimer as nearest neighbor and connected to each other, called *one tetrahedron and one dimer in series* (see Fig. 29).

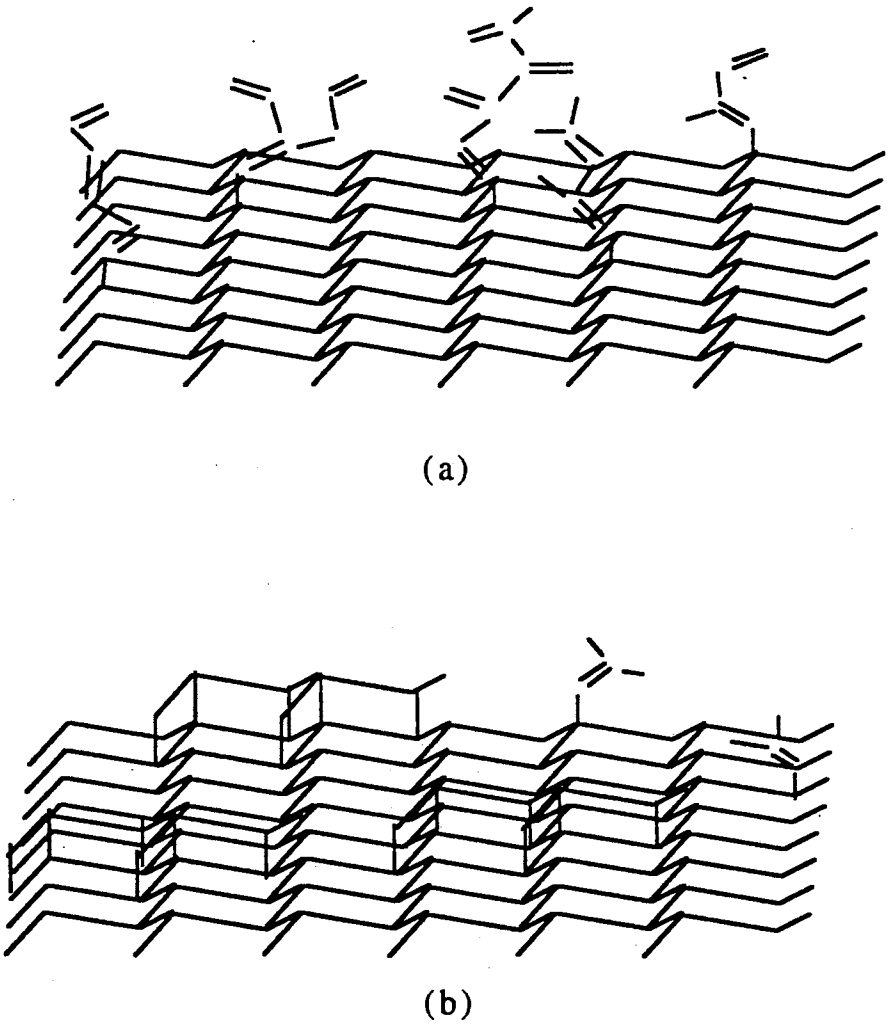

Figure 25. Surface growth configurations (a) without surface diffusion, (b) with surface diffusion.

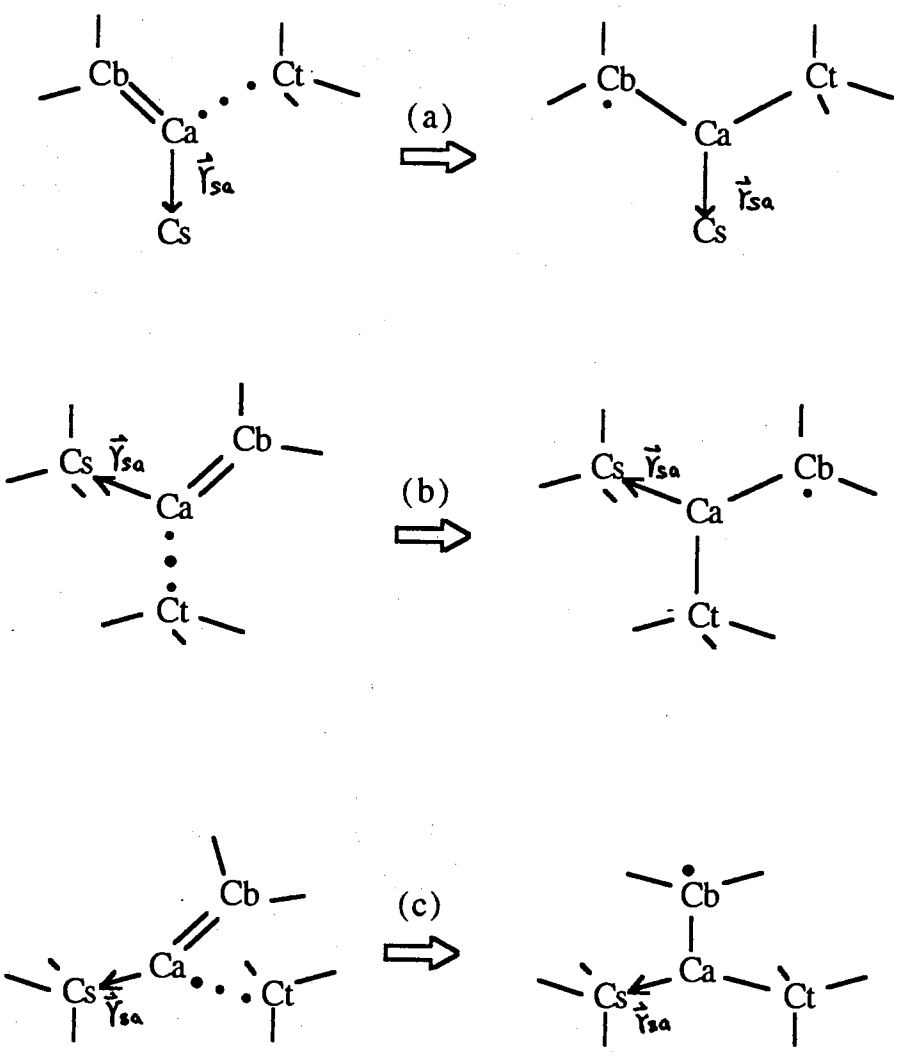

Figure 26. One dimer and One Tetrahedron in Parallel: $C_a = C_b$ dimer, which had a tetrahedron C_t as nearest neighbor but not connected to each other, connected to an surface carbon C_s with a bond vector $\vec{r}_{sa}$ when (a) $\vec{r}_{sa}$ was perpendicular to $C(111)$ surface, (b) $\vec{r}_{sa}$ was tilted up, as well as (c) $\vec{r}_{sa}$ was tilted down.

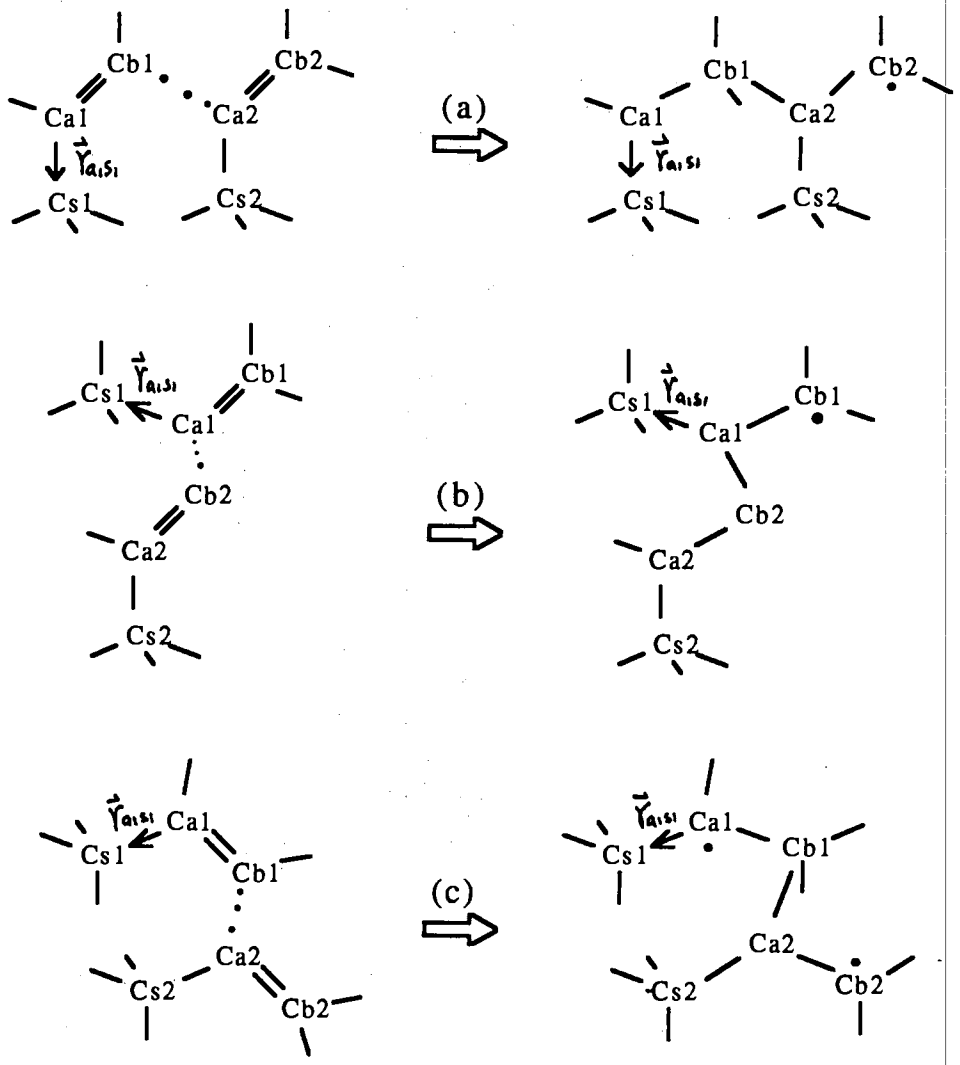

Figure 27. Two $C = C$ dimers are parallel each other. Three possible situations of bond vector $\vec{r}_{a1s1}$ were considered: (a) $\vec{r}_{a1s1}$ was perpendicular to $C(111)$) surface. (b) $\vec{r}_{a1s1}$ was tilted up. (c) $\vec{r}_{a1s1}$ was tilted down.

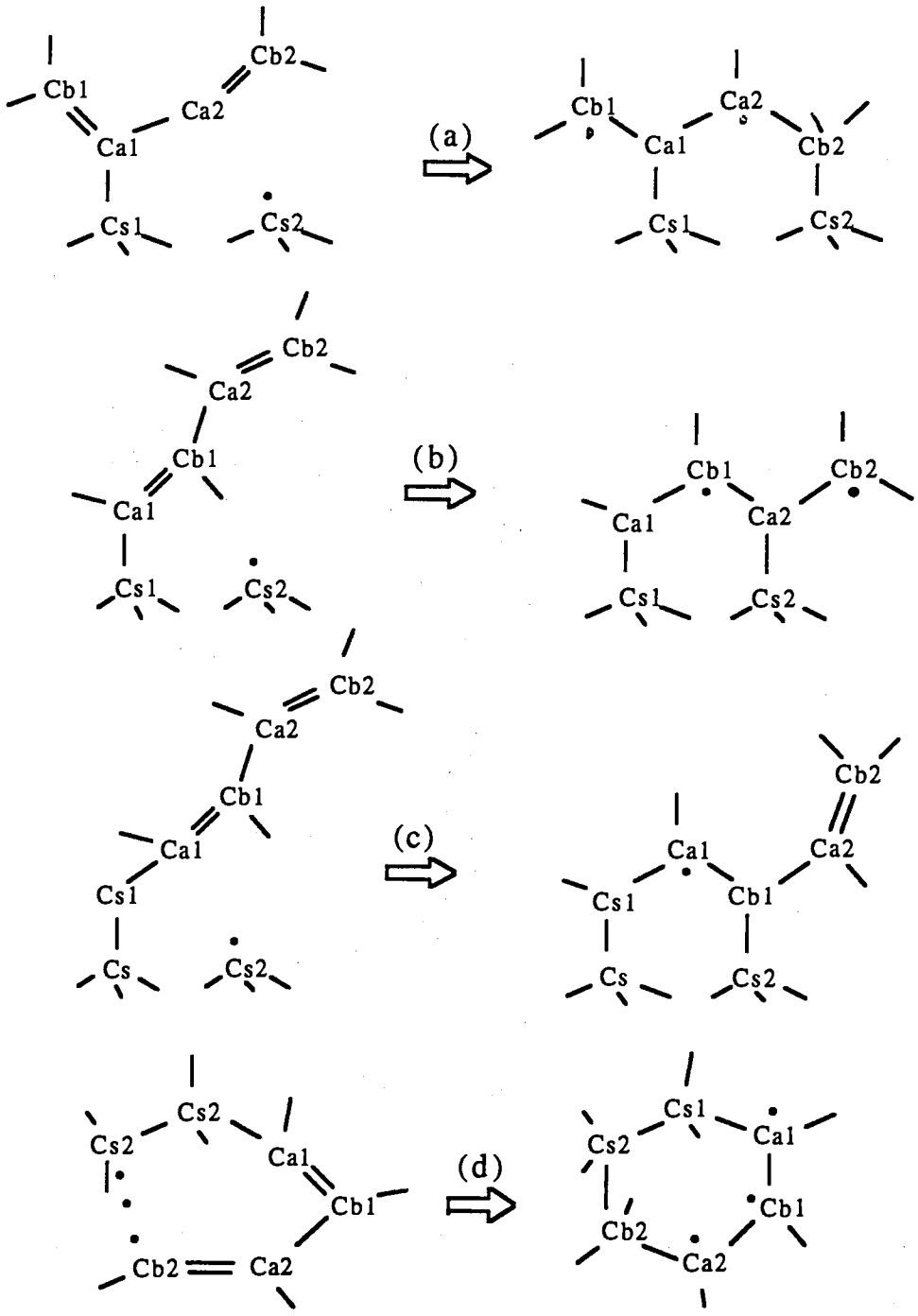

Figure 28. Two $C = C$ dimers configured in series. *Dimer* 1 and *dimer* 2 are connected to each other via bond (a) $C_{a1} - C_{a2}$, (b) → (d) *dimer* 1 and *dimer* 2 are connected via bond $C_{b1} - C_{a2}$. (a) → (c) shows tree-like connectivity; (d) shows ring-like connectivity.

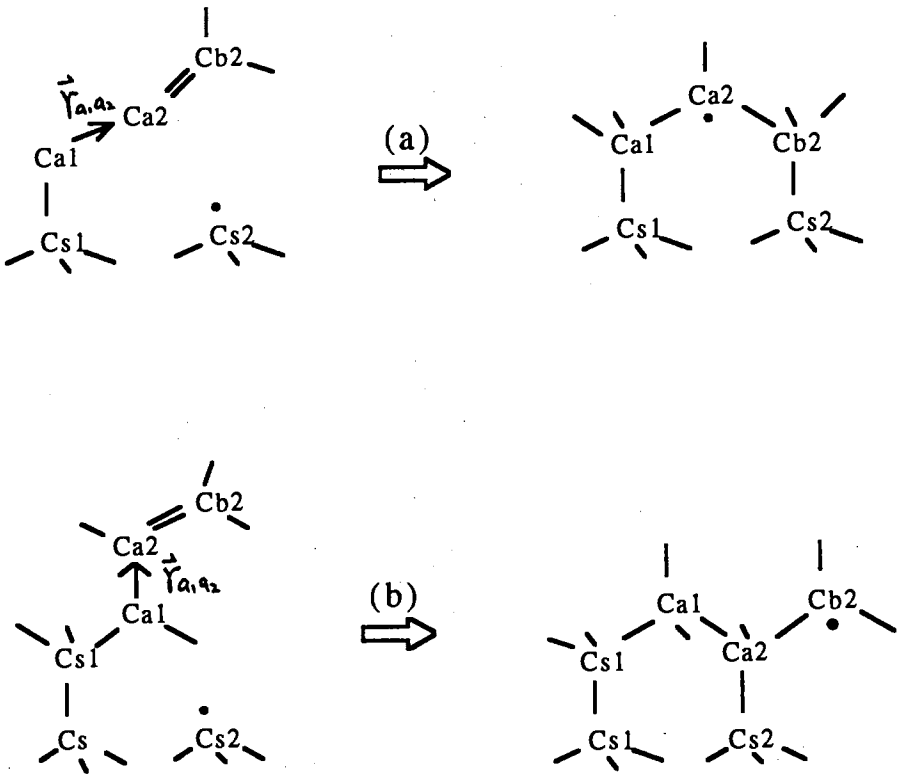

Figure 29. A tetrahedron and a dimer configured in series. Bond vector $\vec{r}_{a1a2}$ is (a) tilted with respective to; (b) perpendicular to the $C(111)$ surface.

- Two C_a tetrahedrons were adjacent but not connected to each other, called *two tetrahedrons in parallel* (see Fig. 30).

In all cases, the old energy configuration was computed. Then, configuration changes from old to new were made through surface diffusion, local regroup, hop or migration, as well as bond rotation and formation. Finally, the new energy associated with the new configuration was computed to compare with the old energy. The procedure for each situation listed above will be described in detail below.

One Dimer and One Tetrahedron in Parallel

Fig. 26 shows a $C_a = C_b$ dimer connected to a surface carbon C_s with a single bond $C_s - C_a$, called $\vec{r}_{sa}$. There are three possible directions of bond vector $\vec{r}_{sa}$: (a) $\vec{r}_{sa}$ perpendicular to the $C(111)$ surface, (b) $\vec{r}_{sa}$ tilted up, (c) $\vec{r}_{sa}$ tilted down. The $C_a = C_b$ dimer is also adjacent to an unpaired bond of tetrahedron C_t, but not connected. The distance along the unpaired bond between C_a and C_t is so close (about 1.55 Å) that it is easy for them to form a $C_a - C_t$ single bond with the the change of the $C_a = C_b$ double bond to a $C_a - C_b$ single bond. Consequently, two new tetrahedrons C_a and C_b form. We found that this situation frequently occurred at the edge of a local tetrahedron-island. The area of tetrahedron-island thereby gradually expanded to form a diamond layer.

Because of the random process of hydrogen abstraction, the bond-index of the unpaired bond of C_t could be any one of four bond-indices, and this will determine the direction of bond $C_a - C_t$. For a 3-dimensional configuration of a tetrahedron, each angle between any two bonds is 109° 28′. Practically, we need to use some given fixed bonds to locate others. For instance, given fixed bonds might be $C_a - C_t$ and $C_s - C_a$. However, there still are many possible orientations of the other bonds of C_a and C_b. For most purposes, a four tetrahedron cluster was considered. Fig. 31 shows from a top view that tetrahedral carbon atoms a, b, c and d connect to each other in series. Assuming one bond of each atom is perpendicular to the $C(111)$

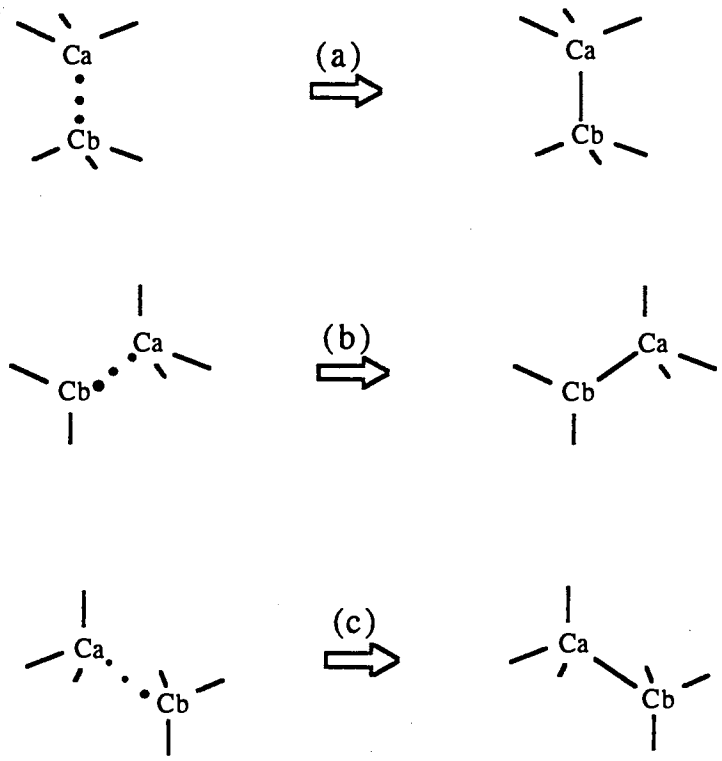

Figure 30. Two adjacent tetrahedrons with unpaired bonds in the direction of the dotted line. The direction of the dotted line is (a) perpendicular to $C(111)$ surface; (b) tilted up; (c) tilted down.

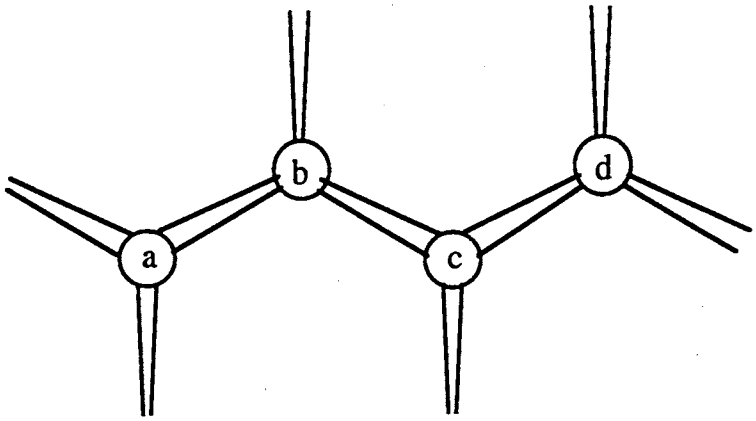

Figure 31. Bond connections of diamond structure (from a top view of the $C(111)$ surface) for tetrahedral carbons a, b, c and d.

surface, we view them along this bond. As we can see, carbon a has three possible connections with b. carbon b has another two possible connections with c. Further along, carbon c has two additional connections with d. Furthermore, for each of d there are two free bonds to connect to either hydrogens or other carbons. Thus, the total number of possible connections for a four tetrahedrons cluster illustrated in Fig. 31 is $3 \times 2 \times 2 \times 2 = 24$. Practically, there is other helpful information such as: (1) given bond vectors, (2) volume repulsion of other atoms, (3) requirement of lower energy configuration. With the help of those conditions, we can determine directions of all bonds.

Two dimers in Parallel

Let $C_{s1} - C_{a1} = C_{b1}$ denote *dimer* 1 growing from C_{s1}, and let $C_{s2} - C_{a2} = C_{b2}$ denote *dimer* 2 growing from C_{s2}. *Dimer* 1 and *dimer* 2 are not directly connected to each other. Three possible situations for bond vector $\vec{r}_{a1s1}$ are illustrated in Fig. 27. Case (a) shows that both $\vec{r}_{a1s1}$ of bond $C_{s1} - C_{a1}$ and $\vec{r}_{a2s2}$ of bond $C_{s2} - C_{a2}$ are perpendicular to $C(111)$) surface. However, the orientation of each planar dimer could be different. When the distance between carbons C_{b1} and C_{a2} is close enough to form a new $C_{b1} - C_{a2}$ bond, the two dimers break their $C = C$ double bonds to become tetrahedrons. The configuration change is done numerically using the fixed bond vectors $\vec{r}_{a1s1}$ and $\vec{r}_{a2s2}$. Because the angle between any two bonds for a tetrahedron is 109°28′, all orientations of the bonds can be determined given the orientations of any two bonds, or can be optionally determined for given the orientation of an any bond (the other three bonds can rotate around the given bond).

Case (b) shows $\vec{r}_{a1s1}$ tilted up. *Dimer* 1 and *dimer* 2 may change to four tetrahedral carbons by forming a new bond $C_{a1} - C_{b2}$ when the distance between carbons C_{a1} and C_{b2} is close enough. Case (c) shows $\vec{r}_{a1s1}$ tilted down. A new bond could be formed between C_{b1} and C_{a2}. Four new tetrahedral carbons may form as a different configuration from those in the cases (a) and (b).

Two dimers in Series

Four possible cases of two dimers in series have been considered, and are illustrated in Fig. 28. Cases (a) → (c) show tree-like structures. In fact, these tree-like structures were not stable. The dimers on the branch may either be desorbed from surface or form a new bond with a surface carbon C_{s2}. The case of desorption will be discussed in a later section. The formation of a new bond between dimers and the surface carbon C_{s2} will be discussed here.

First, C_{s2} must satisfy two conditions: (1) it must be a nearest neighbor of the dimer tree; (2) it must have an unpaired bond oriented towards the tree. Then, for the different cases we considered here, tetrahedral structure could form. In case (a), carbon C_{a2} of *dimer* 2 is connected to carbon C_{a1} of *dimer* 1. A new sp^3 bond formation occurs between the carbon C_{b2} and the surface carbon C_{s2}. In case (b), carbon C_{a2} is connected to carbon C_{b1}. The new sp^3 bond forms between C_{a2} and C_{s2}. In case (c), Carbons C_{b1} and C_{s2} connect to each other to form a new sp^3 bond.

Unlike cases (a), (b) and (c), case (d) shows ring-like structure. Two surface carbon (C_{s2} and C_{s1}) and two dimers are connected to form a six carbon chain. Rotations may occur about any carbon-carbon single bond. When the tail of the chain, carbon C_{b2}, moves close to the head of chain, C_{s2}, along the direction of unpaired bond of C_{s2}, a new sp^3 bond can form between C_{b2} and C_{s2}. Thus, a closed tetrahedral hex-ring is created.

One Tetrahedron and One dimer in Series

Fig. 29 shows a dimer (C_{a2} and C_{b2}) connected to a tetrahedron (C_{a1}) forming a short chain structure. Two additional situations were considered: the direction of bond vector $\vec{r}_{a1a2}$ is (a) tilted; (b) perpendicular to $C(111)$ surface. Again, another surface carbon C_{s2} must be a nearest neighbor of the short chain, and must have an unpaired bond oriented towards the chain. Then, a new sp^3 bond may formed between $C_{s2} - C_{b2}$ for case (a), and $C_{s2} - C_{a2}$ for case (b), respectively.

Two Adjacent Tetrahedrons

Considering two adjacent tetrahedrons, when the distance between them was about 1.55 Å, and both of them had unpaired bonds in the direction of their connecting line shown in Fig. 30, there were three additional possible situations: vector $\vec{r}_{ab}$ is (a) perpendicular to $C(111)$ surface; (b) tilted up; (c) tilted down. Practically, they formed a bond $C_a - C_b$ to connect each other very easily.

Common Subroutines for Surface Transitions

Many common subroutines were used in surface transitions. We will describe them below.

According to the general Monte Carlo algorithm, the old configuration should be saved before moving to a new configuration. Subroutine *Save_old*() was used to save old configuration. If a Monte Carlo move failed, subroutine *Back_old* was used to let system go back to the old configuration.

When carbon chains are connected to the carbon that will be moved, the first thing we need to do is to find the coordinates of each carbon on the chain and all bond vectors. This was done by subroutine *Tree*(). Subroutine *Tail_save*() was used to save the old configuration of chains. Fig. 32 (a) shows an old configuration of a dimer $C_a = C_b$ and its tail chain with components of C_1, C_2, C_3 and C_4.

Next, we need to move chains associated with the above dimer changing to two tetrahedrons (see Fig. 32 (b)). This was done by subroutines *Tail_newc*(), *Tilt_ran_rot*() and *Connect*(). From Fig. 32, the entire chain needs to rotated an angle Ω that is the angle between new bond vector $\vec{r}'_{ac1}$ and old bond vector $\vec{r}_{ac1}$. Thus, all bonds of chain have to be rotated through the angle Ω. The way thus was done is illustrated in Fig. 33. With the help of three dimensional components of bond vectors, it is easy to find the angles including:

θ_1, the angle between $\vec{r}_{ac}$ and Z axis,

ϕ_1, the angle between the projection of $\vec{r}_{ac}$ on $X - Y$ plane and X axis,

θ_2, the angle between $\vec{r}'_{ac}$ and Z axis,

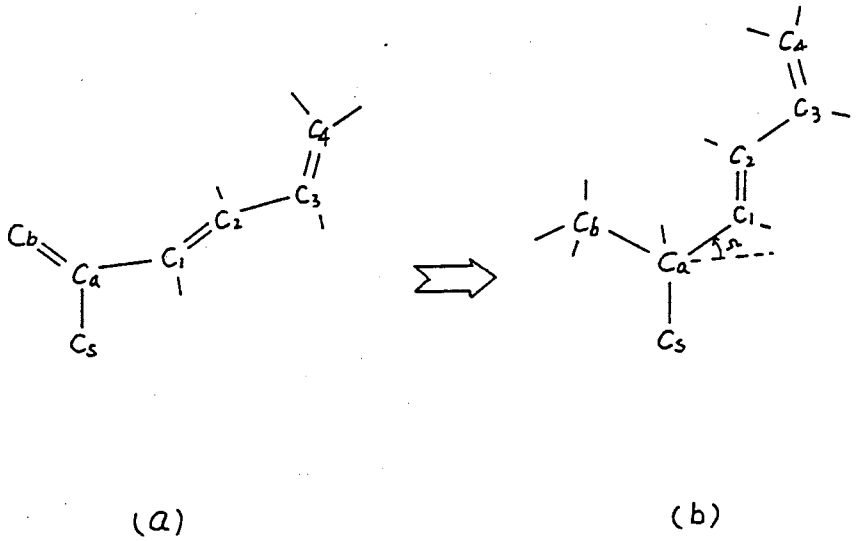

Figure 32. Pictorial description of a possible chain transition. (a) initial configuration of a dimer $C_a = C_b$ and its tail chain with components of C_1, C_2, C_3 and C_4. (b) After carbon C_a and C_b become tetrahedral, the chain moves accordingly.

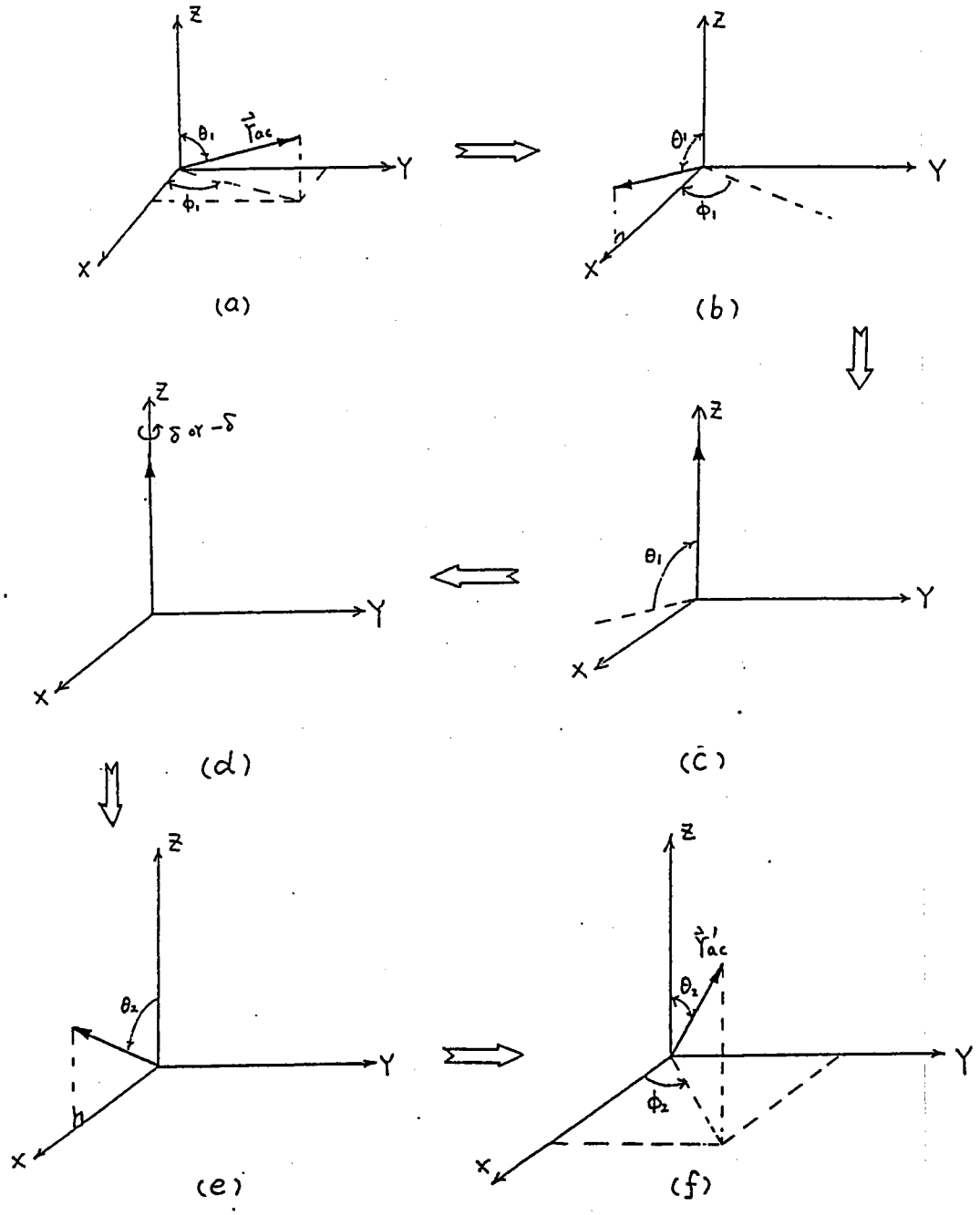

Figure 33. General procedure for bond rotation from $\vec{r}_{ac}$ to $\vec{r}'_{ac}$. (a) $\vec{r}_{ac}$ has an angle $\theta 1$ with Z axis and its projection on $X-Y$ plane has an angle ϕ_1 with X axis. $\vec{r}_{ac}$ executes a series rotations (b) around Z axis with ϕ_1, (c) around Y axis with θ_1, (d) around Z axis with any small random angle δ, (e) around Y axis with angle θ_2 which is the angle between vector $\vec{r}'_{ac}$ and Z axis, (f) around Z axis with angle ϕ_2, an angle between the projection of $\vec{r}'_{ac}$ on $X-Y$ plane and X axis.

ϕ_2, the angle between the projection of $\vec{r'}_{ac}$ on $X-Y$ plane and X axis.
Once the values of the angles were determined, all bonds from carbon C_a to the end of tail have to be rotated. For the example of Fig. 33, all bonds on the tail, including $C_a - C_1$, $C_1 = C_2$, $C_2 - C_3$ and $C_3 = C_4$, need to execute a series rotations illustrated in the figure:

(a) $\rightarrow$ (b) around Z axis with ϕ_1,

(b) $\rightarrow$ (c) around Y axis with θ_1,

(c) $\rightarrow$ (e) around Y axis with angle θ_2

(e) $\rightarrow$ (f) around Z axis with angle ϕ_2.

3-9 Surface Relaxation

In order to approach a lower energy configuration we utilized bond rotations to achieve surface relaxation. First, we picked up a rotatable bond, such as a carbon-carbon single bond $(C-C)$, randomly. Second, we found all carbons and bonds following the rotatable bond. Then, the same procedure as a chain move (discussed in previous section) was performed (see Fig. 32 and Fig. 33). However, the rotational angles were not the same. The small angle δ, which we picked randomly, was considered for surface relaxation. For instance, here, $\delta \neq 0$, $\theta_2 = \theta_1$, as well as $\phi_2 = \phi_1$. We rotated each bond individually. Finally, we connected those bonds to each other and located new positions of carbons.

3-10 Chemical Desorption-Adsorption

As we mentioned in previous section adsorbed molecules may desorb to go back to the gas phase. In our simulation, during each KMC pass through the system all adsorbed $C_a = C_b$ dimers were given opportunities to desorb from surface by breaking the $C_s - C_a$ bond, resulting in a free $C \equiv C$ gaseous species. desorbed $C \equiv C$ was then allowed to randomly move near the surface to attempt to re-adsorb at a different site. Some $C \equiv C$ species experience several adsorption

and desorption events before becoming part of a tetrahedral (and therefore stable) structure.

3-11 Run Procedures

Simulations were run on the Cray Y-MP at the National Center for Supercomputing Applications at the University of Illinois at Urbana-Champaign. Three sets of simulations were run:

1. For a 200-carbons substrate system, 15K KMC passes through the system at a temperature of 1300 K.

2. For a 200-carbons substrate system in which desorption was "turned off" to determine the effect on the structure of the film, and 18K KMC passes through the system at a temperature of 1300 K.

3. For a 512-carbons substrate system, 22K KMC passes through the system at a temperature of 1300 K.

The results of the three sets of runs will be described in next chapter.

CHAPTER IV

RESULTS AND DISCUSSION

4-1 The Role of Chemical Desorption in Film Growth

The results show that chemical desorption plays an important role in the process of diamond film growth. Desorption turned out to be less likely if the neighborhood of the adsorbed $C = C$ dimer was locally similar to a clean C[111] surface. Dynamical calculations [73] show the same result, i.e. desorption from a clean $C[111]$ surface is unlikely but it is highly probable from other surface structures. In other cases (e.g. a $C = C$ adsorbed to an isolated $C_s - C$) desorption occurs easily, resulting in free $C \equiv C$ molecules. In the simulations, desorbed $C \equiv C$ molecules are allowed to move randomly near the surface until they re-adsorbed elsewhere. This desorption and surface diffusion led to a layer-by-layer growth of the film in the simulations, as each layer tended to reach close to 50% coverage before the next layer began to take shape. TABLE IV shows layer-by-layer coverage as a function of the number of KMC steps. It can be seen that layers 1 and 2 reached over 50% coverage before the next layer exceeded 10% coverage.

By comparison, when desorption was turned off the film took on a dendritic structure, with poor crystalline order in any layer. TABLE V shows that crystalline film growth is slower in this case. This is because branched dendritic structures form. These structures impede crystal growth by blocking deposition in lower layers. Both TABLE IV and TABLE V were for 200-carbon substrate systems.

The Tables show that in the former case (with desorption) layers have greater coverage than in the latter case (without desorption), and therefore greater crystalline order. It is established that, in general growth problems, the mechanism of

desorption and surface diffusion is an aid in the improvement of the quality of the resulting crystal [148]. However the effectiveness of this mechanism must depend in each case on the details of the interactions between adsorbed, gas phase, and substrate atoms. Our simulations show the effect of surface interactions under the Brenner potential.

For the case of a simulation with a 512-carbon substrate Fig. 34 shows the coverage of diamond film growth for each layer as a function of KMC steps. When layer 2 reached 6% coverage layer 1 had already reached over 55% coverage. While layer 3 reached 9.8% coverage layer 1 and layer 2 reached 74.6% and 41.0% coverage, respectively. When layer 4 reached 10.9% coverage layer 1, layer 2 and layer 3 reached 83.8%, 69.9% and 50.6% coverage, respectively.

4-2 The Average Height of the Crystalline Film

Fig. 35 shows the average heights of the crystalline film against the KMC step number for both the 512-carbon substrate simulation, symbolized by ($\Box$), and 200-carbon substrate simulations, symbolized by ($+$) and (Δ). The branched structures are not counted in the average height calculation. Comparison of the results of 512-carbon substrate and 200-carbon substrate for the runs in which desorption were allowed, (($\Box$) and ($+$)), show that they have similar average height curves. One can also observe three regions in this figure where the height curves exhibit a reduction in slope, followed by an increase in slope. The periodic leveling off of the growth curve is due to successive filling of layers 1, 2, and 3 respectively. The curves do not become perfectly flat at these "plateaus" because the average height still increases as a layer fills, but the rate of increase is slower than during the initial formation of a new layer.

The simulation with no surface desorption is symbolized by (Δ) in Fig. 35. Comparison of the curves with and without desorption shows that the crystalline film grows more rapidly when desorption occurs. When desorption is not allowed branched structures containing $C = C$ bonds form and impede the crystallization process in the shaded area. The slope of the curves are about 0.24 (Å /1000 KMC

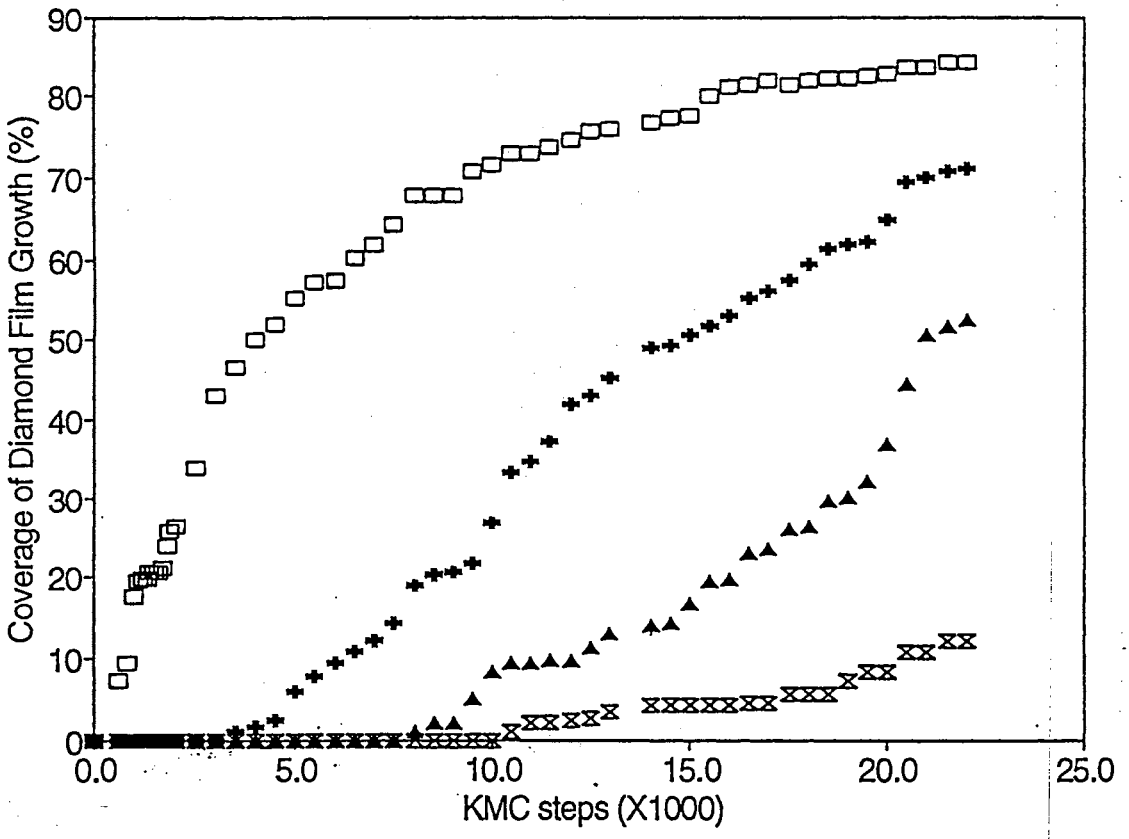

Figure 34. Plot of the coverage of diamond film growth for each layer as a function of KMC steps: (□) for layer 1, (+) for layer 2, (Δ) for layer 3, and (X) for layer 4.

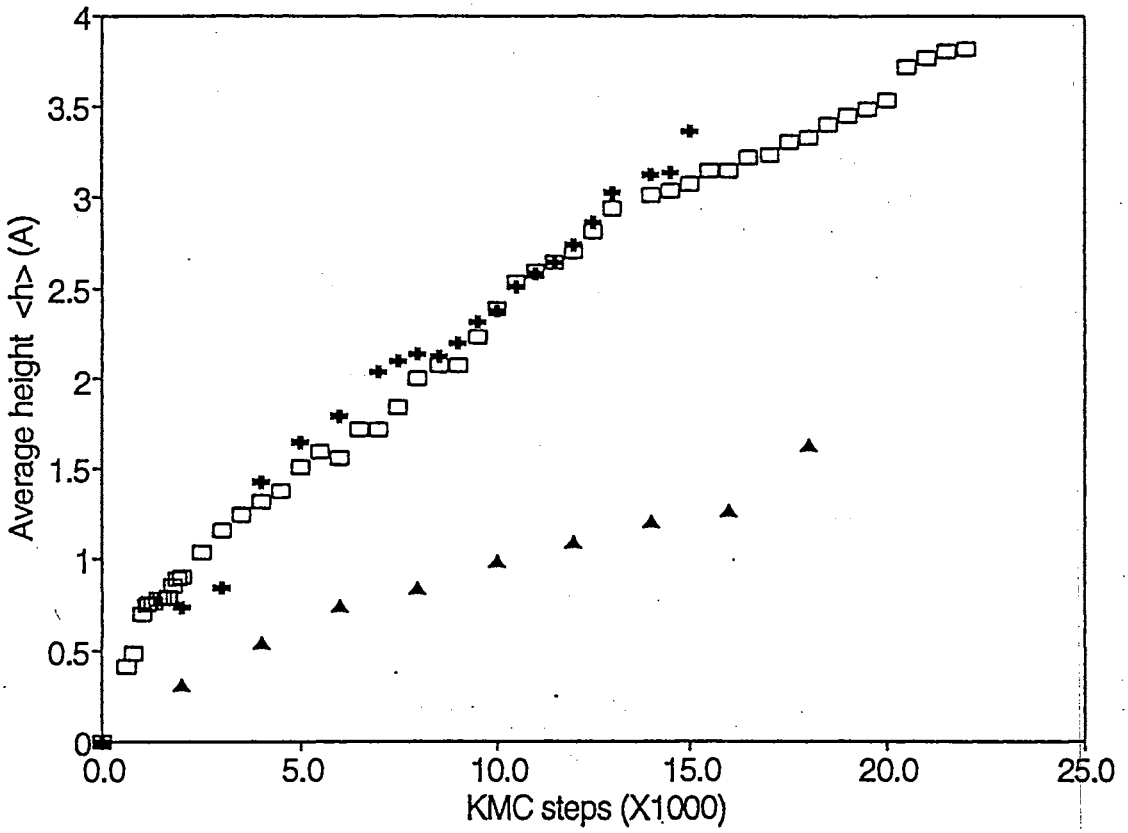

Figure 35. Plot of the average height of the crystalline film against the KMC step number: (□) for the 512-carbon substrate system; (+) for the 200-carbon substrate system; (Δ) for the 200-carbon substrate system, when desorption was turned off.

steps) and 0.088 (Å /1000 KMC steps) for the curves with and without desorption, respectively.

4-3 Transformation from Non-Tetrahedral Carbon to Tetrahedral Carbon

Fig. 36 depicts the extent of the tetrahedral crystallinity of the adsorbed film for the cases of both the 512-carbon substrate system (□), and 200-carbon substrate system (+ and **Δ**), respectively. All carbons at the surface were counted for testing tetrahedral crystallinity.

Compared with the results of 200-carbon substrate for the runs in which desorption were allowed (□ and +), the ratio of tetrahedrally bonded carbon to deposited acetylene for 512-carbon substrate was approaching to the curve for the 200-carbon substrate.

Comparison of the cases of desorption allowed (+) and not allowed (**Δ**) show that the ratio of tetrahedrally bonded carbon to deposited acetylene is much greater for the former case than for the latter case. The differences of the radios between desorption allowed and not-allowed were about 29 % after 5000 KMC steps, 28 % after 10000 KMC steps, and 36 % after 15000 KMC steps. The reason for this is that when desorption is allowed, it is possible for a $C = C$ dimer to desorb and then to re-form in a tetrahedral geometry elsewhere at the surface. Consequently, the total number of the tetrahedral carbon is greater than that for the case where desorption is not allowed. This is evidence that chemical desorption plays an important role in the process of diamond film growth.

4-4 Snapshot of a Simulated Film

Fig. 37 is a snapshot of the configuration of the substrate plus film after 22,000 KMC passes for the 512-carbon substrate simulation. Five tetrahedrally coordinated layers (the $C(111)$ substrate and four adsorbed layers) can be observed, with a number of adsorbed structures containing $C = C$ bonded pairs (the double lines), as well as C_2H_2 and C_2H vapor phase (the triple lines). There are total

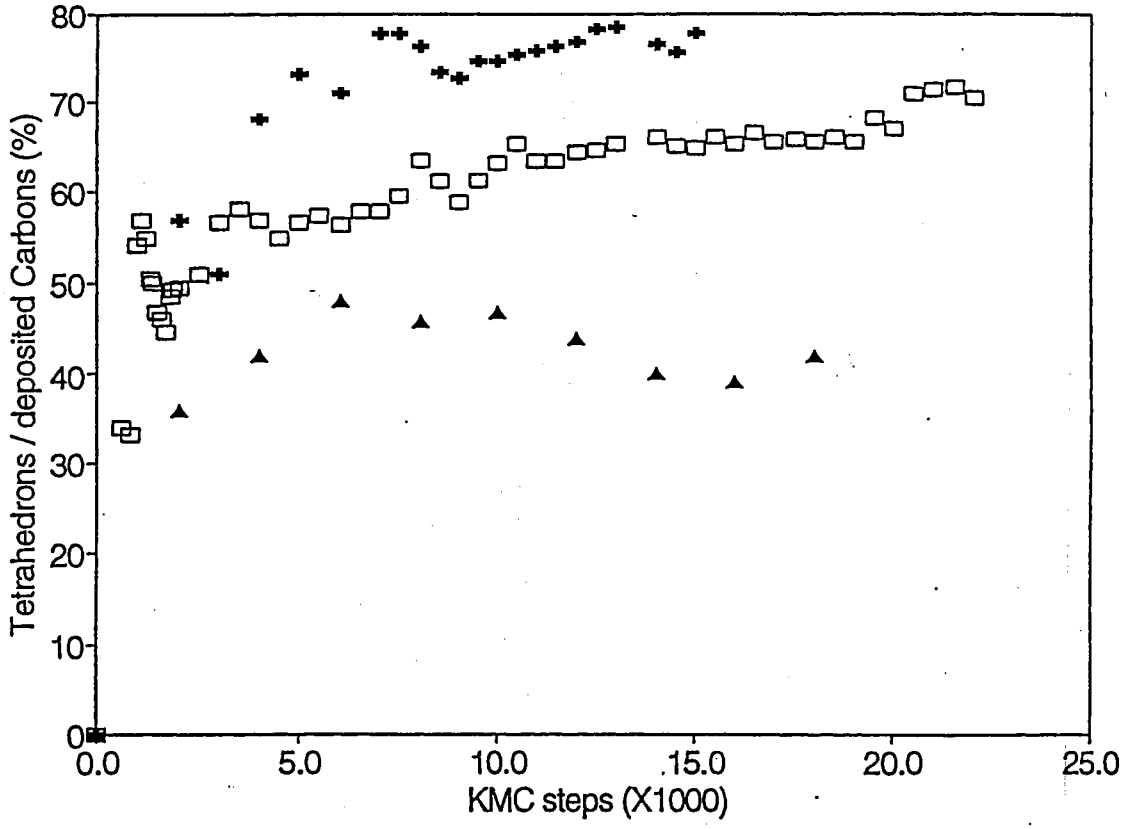

Figure 36. Plot of the ratio of tetrahedrally bonded adsorbed carbon to the total number of deposited carbon atoms: (□) for the 512-carbon substrate system; (+) for the 200-carbons substrate system; (Δ) for the 200-carbon substrate system, and the runs in which desorption was turned off.

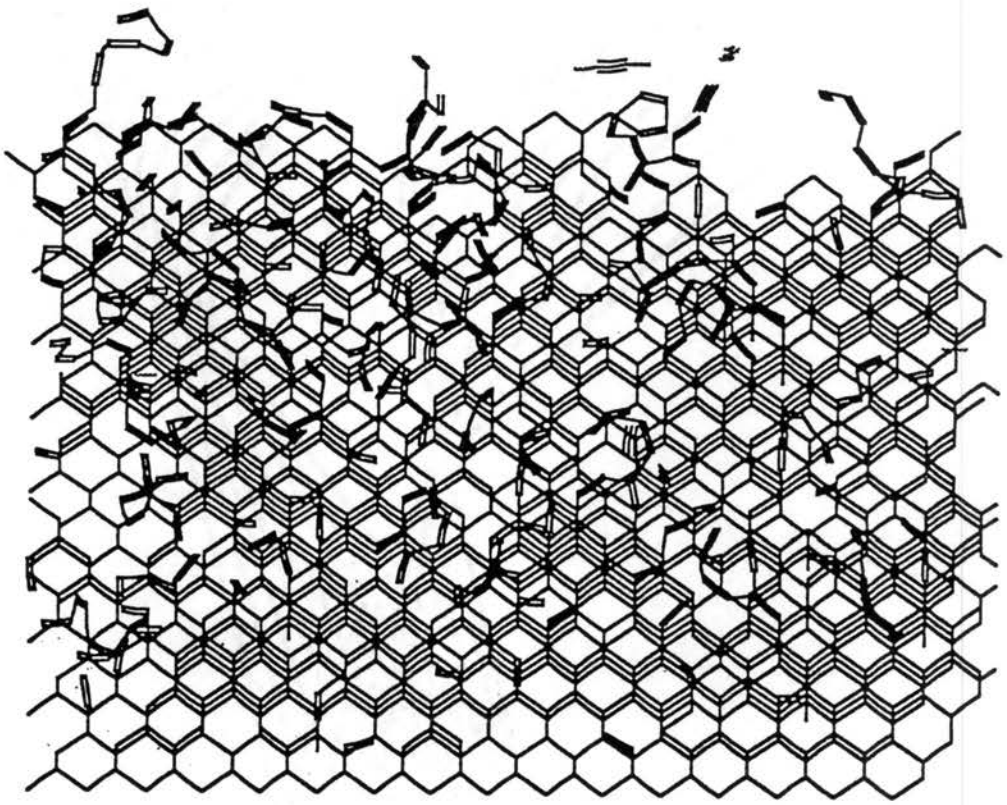

Figure 37. Snapshot of the simulated film after 22K KMC steps. Picture shows the $C(111)$ substrate and up to four adsorbed layers, tilted slightly towards the viewer. Single lines are $C-C$ tetrahedral bonds, short double lines are $C=C$ bonds, and the shortest triple lines are $C \equiv C$ bonds.

of 2108 carbons (1638 tetrahedrons and 470 atoms belong to $C = C$, $C \equiv C$ molecules) shown in the figure after 22,000 KMC steps.

A few of tree-like structures appear in the snapshot even though they are not stable. Some tree-like structures are branched, some are not. They can rotate during surface relaxation, or bend to the surface to form tetrahedrons, or break their branch to desorb from the surface.

An unclosed hex-ring can be seen at the top edge. Whether it will complete the hex-ring by closing the end of carbons or the dimers will desorb by breaking their bonds will depend upon local energetics. The conditions for closing the ring are (1) the tail carbon is close to the head carbon (the chain tail could be any orientation due to the surface relaxing rotation); (2) a bond forms between the tail carbon and the head carbon and is energetically acceptable.

Gaseous acetylene ($C \equiv C$) diffuses near the surface to deposit or be re-adsorbed to the surface. We found that the concentration of $C \equiv C$ varied with the extent diamond crystallization at the surface. Before a new layer started, one or more tree-like structures appeared at the film interface. Then, most of the branches of these structures desorbed from the surface, resulting in an increased local concentration of $C \equiv C$. This provided a good opportunity for $C \equiv C$ readsorption onto energetically more favorable sites. In this way, more and more re-adsorbed $C = C$ dimers became tetrahedrons. This progress occurred, periodically, as each layer formed.

4-5 Plot of a Simulated Film Surface

Fig. 38 is a surface plot of the top carbon at each lattice site for the configuration of diamond film in Fig. 37. Due to the complexity of the potential surface we used, the simulation cells were necessarily small, and this made it impossible to observe micrometer scale structures in the simulations for direct comparison with experiments. However, it is possible to compare our results shown in Fig. 38 with atomic scale measurements done by atomic force microscopy (AFM).

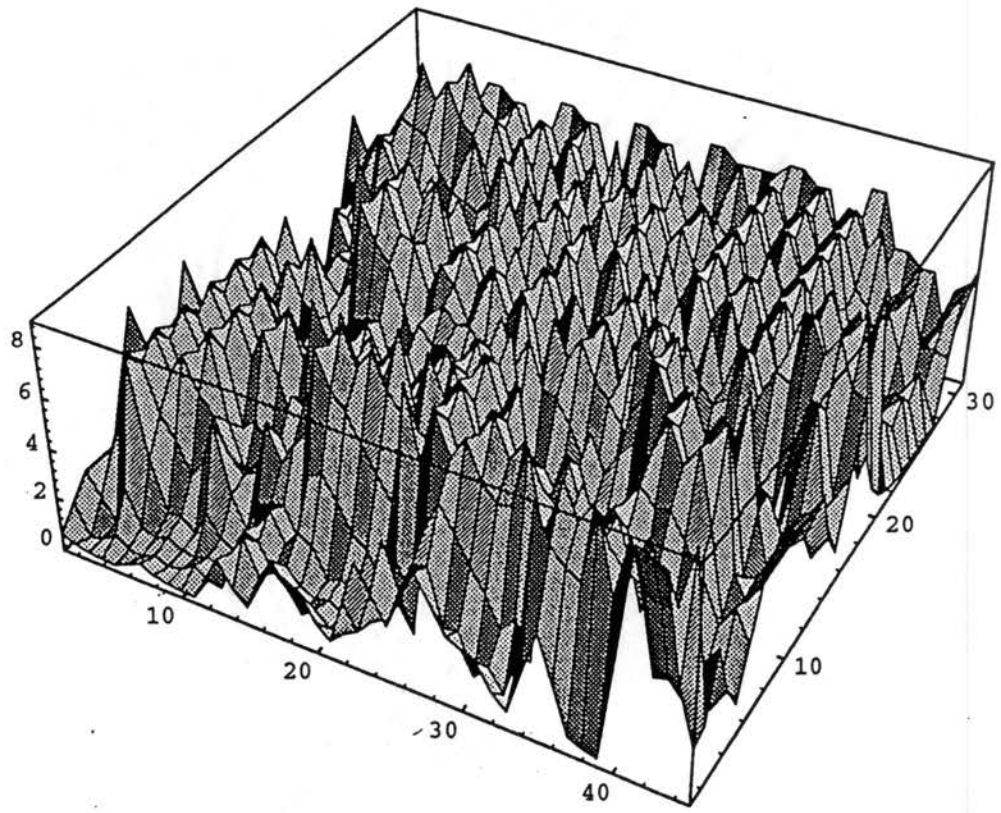

Figure 38. Surface plot of the top carbon at each lattice site for the configuration of diamond film. Distance on the vertical axis is in angstroms, while the horizontal axes labels are site indices. The horizontal dimensions are 44.6 Å X 33.7 Å.

Fig. 38 reveals roughness on the atomic scale with a maximum amplitude of about 5 Å. By comparison, AFM micrographs show roughness on an atomic scale with maximum amplitude of about 3 Å [149]. Similar results of surface roughness for the smaller size simulation (200-carbon substrate) were obtained, suggesting that the roughness is not a function of simulation size. The maximum amplitude of about 5 Å is over a two-layers difference (about 2.06 Å height for each layer on the $C(111)$ surface). This occurs at the edge of tetrahedral islands or in the small area between islands. It appears to be hard to fill the lower sites with newly arrived $C = C$ dimers in the small area between islands. A possible solution of the problem of volume effect caused by $C = C$ dimer is to allow the methyl radical CH_3, a smaller growth species, to be an additional growth molecule.

4-6 Future Work

Our simulations have demonstrated that it is possible to model the atom-by-atom growth of diamond films by kinetic Monte Carlo methods. The potential function of Brenner [118] provides an excellent base for such simulations, and allows for the direct examination of the mechanisms involved in the growth process. However, what should be next step of our research? A plan of study may be considered below.

- As discussed in the Introduction, it is plausible that acetylene dimers are not the only growth species, and perhaps not even the primary one. The dimeric nature of acetylene presents slightly greater excluded volume problems than, say, methyl radical, and this should produce slower growth and rougher surfaces. Future simulations will include the methyl radical CH_3 in the vapor phase as a growth species.

- Although we have simulated two different sizes of substrates with 200-carbons and 512-carbons it seems that the results of two simulations were not distinctly different. This means that the size of the simulation may still not be

large enough to test for a finite size effect. In future, a larger simulation may be run when we can get more computer time to run this.

- What is currently missing is a precise timescale for the simulations. This is only available if the rates for the various reactions are known [126]. Ongoing molecular dynamics calculations of these rates by Raff and coworkers, as well as others, will make this information available in the near future. In future, we will directly apply the rates to KMC simulations. This will save tremendous computer time to simulate huge system with micrometer scale.

Generally, in the future our simulations of atom-by-atom model will provide us with a more realistic system to compare with experimental measurement, and a better understanding of the mechanism of diamond CVD to elucidate the fundamental process in low-pressure diamond synthesis.

TABLE IV.

LAYER-BY-LAYER DIAMOND FILM GROWTH RATE:
DESORPTION ALLOWED

KMCS (x1000)	0.0	2.0	4.0	6.0	8.0	10.0	12.0	14.0	15.0
Layer 1 (%)	0.0	21.0	37.0	55.0	66.0	70.0	75.5	76.5	80.0
Layer 2 (%)	0.0	2.0	8.0	18.0	38.0	52.0	60.0	61.5	64.0
Layer 3 (%)	0.0	0.0	2.0	2.0	2.0	4.0	20.0	34.0	38.0
Layer 4 (%)	0.0	0.0	0.0	0.0	0.0	0.0	0.0	6.0	14.0

TABLE V.

LAYER-BY-LAYER DIAMOND FILM GROWTH RATE:
DESORPTION NOT ALLOWED

KMCS (x1000)	0.0	2.0	4.0	6.0	8.0	10.0	12.0	14.0	16.0	18.0
Layer 1 (%)	0.0	7.0	10.0	17.0	21.0	28.0	30.0	31.0	36.0	36.0
Layer 2 (%)	0.0	0.0	2.0	2.0	2.0	2.0	4.0	6.0	6.0	13.0
Layer 3 (%)	0.0	0.0	0.0	0.0	0.0	0.0	0.0	0.0	0.0	2.0

BIBLIOGRAPHY

1. Blakey, G. G., *The Diamond*, BAS Printers Limited, London, (1977).
2. Lavoisier, A-L., *Memoire Academie des Sciences*, pp. 564, (1772).
3. Tennant, S., *Phil. Trans. R. Soc.*, **87**, 97, (1797).
4. Bruton, E., *Diamonds*, NAG Press, London, (1978).
5. Davies, G., *Diamond*, Adam Hilger Ltd, Bristol, (1984).
6. Bragg, W. H. Bragg, W. L., *Proc. R. Soc.*, **A89**, 277, (1913).
7. Bernal, J. D., *Proc. R. Soc.*, **A106**, 749, (1924).
8. Martin L. R., *American Ceramic Society Bulletin*, **71**, 1419, (1992).
9. Geis, M. W. and Angus, J. C., *Scientific American*, **October**, 84, (1992).
10. Gannal, J. N., *Chim. Med*, **4**, 582, (1828).
11. Despretz, C., *C. R. Acad. Sci. Paris*, **37**, 443, (1853).
12. Hannay, J. B., *Nature*, **22**, 255, (1880).
13. Moissan, H., *The Electric Furnace*, transl. Monilpied, A. T. de, Edward Arnold, London, (1904).
14. Parsons, C. A., *Proc. R. Soc.*, **A 79**, 532, (1907).
15. Parsons, C. A., *Phil. Trans. R. Soc.*, **220**, 67, (1920).
16. Lonsdale, D., *Nature*, **196**, 104, (1962).
17. Berman, R. and Simon, F., *Z. Elektrochem.*, **59**, 333, (1955).
18. Bridgman, P. W., *J. Appl. Phys*, **12**, 461, (1941).
19. Bridgman, P. W., *J. Chem. Phys*, **15**, 92, (1947).
20. Hawtin, P., Lewis, J. B., Moul, N. and Philips, R. H., *Phil. Trans. R. Soc.*, **A216**, 67, (1966).
21. Lewis, G. N. and Randall, M., *J. Am. Chem. Soc.*, **37**, 458, (1915).

22. Roth, W. and Walasch, H., *Ber. Dtsch. Chem. Ges.*, **46**, 896, (1913).

23. Simon, F., *Handbuch der Physik*, **X**, 350, (1926).

24. Bundy, F. P., Hall, H. T., Strong, H. M. and Wentorf, R. H., *Nature*, **176**, 51, (1955).

25. Eversole, W. G., *U.S. Patent* Nos 3,030,187 and 3,030,188, (1958).

26. Eversole, W. G., *Canadian Patent* No 628,567, (1961).

27. Angus, J. C., Will, H. A. and Stanko, W. S., *J. Appl. Phys.*, **39**, 2915, (1968).

28. Deryagin, B. V. and Fedoseev, D. B., *Scient. Am.*, **233**, November,102, (1975).

29. Deryagin, B. V., Spitsyn, B. V., Buklov, L. L., Klochkov, A. A., Gorodetskii, A. E. and Smol'yaninov, A. V., *Sov. Phys. Dokl.*, **21**, 676, (1976).

30. Spitsyn, B. V., Bouilov, L. L. and Derjaguin, B. V., *J. Crystal Growth*, **52**, 219, (1981).

31. Spitsyn, B. V., Bouilov, L. L. and Derjaguin, B. V., *Prog. Cryst. Growth Charact.*, **17**, 79, (1988).

32. Anderson, D. A., *Phil. Mag.*, **35**, 17, (1977).

33. Gautherin, G. and Weismental, Chr., *Thin Solid Films*, **50**, 135, (1978).

34. Berg, S. and Andersson, L. P., *Thin Solid Films*, **58**, 117, (1979).

35. Matsumoto, S., Sato, Y., Tsutsumi, M. and Setaka, N., *J. Mater. Sci.*, **17**, 3106, (1982).

36. DeVries, *Annual Review of Material Scrence*, **17**, 161, (1987).

37. Angus, J. C., Hayman, C. C., *Science*, **241**, 913, (1988).

38. Lux, B. and Haubner, R., *Refractory Metals and Hard Materials*, p. 158, (1989).

39. Hirose, Y. Amanoma, S., Okada, N. and Komaki, K., *Abstracts, First International Conference on New Diamond Science and Technology*, Tokyo, p. 38, (1988).

40. Hanssen, L. M. Carrington, W. A., Butler, J. G. and Snail, K. A., *Phil. Mater. Sci. Lett.*, **7**, 289, (1988).

41. Yarbrough, W. A., Stewart, M. A. and Cooper, J. A., *Surf. Coatings Technol.*, **39**, 241, (1988).

42. Tzeng, Y., Cutshaw, E., Phillips, R., Sriningunon, T., Ibrahim, A. and Loo, B. H., *Appl. Phys. Lett.*, **56**, 134, (1990).

43. Komanduri, R., Snail, K. S. and Fehrenbacher, L. L., *Philosophical Magazine Letters*, **62**, 283, (1990).

44. Kittel, C., *Introduction to Solid State Physics*, John Wiley & Sons, Inc., (1986).

45. Pate, B. B., *Surf. Sci.*, **165**, 83, (1986).

46. Hamza, A. V., Kubiak, G. D. and Stulen, R. H., *Surf. Sci.*, **206**, L833, (1988).

47. Lander, J. J. and Morrison, J., *Surf. Sci.*, **4**, 241, (1966).

48. Vidali, G. and Frankl, D. R., *Phys. Rev. B.*, **27**, 2480, (1983).

49. Pandey, K. C., *Phys. Rev. Lett.*, **47**, 1913, (1981).

50. Hamza, A. V., Kubiak, G. D. and Stulen, R. H., *Surf. Sci.*, **237**, 35, (1990).

51. Maguire, H. G., *Phys. Status Solidi B*, **76**, 715, (1976).

52. Marsh, J. B. and Farnsworth, H. E., *Surf. Sci.*, **1**, 3, (1964).

53. Celii, F. G. and Butler, J. E., *Auun. Rev. Phys. Chem.*, **42**, 643, (1991).

54. Lurie, P. G. and Wilson, J. M., *Surf. Sci.*, **65**, 453, (1977).

55. Cappelli, M. A. and Paul, P. H., *J. Appl. Phys.*, **67**, 2596, (1990).

56. Celii, F. G., Pehrsson, P. E., Wang, H. and Butler, J. E., *Appl. Phys. Lett.*, **52**, 2043, (1988a).

57. Celii, F. G., Pehrsson, P. E., Wang, H., Nelson, H. H. and Butler, J. E., *Proc. 1st Int. Conf. New Diamond Sci. Technol.*, ed. Saito, S. and Yoshikawa, M., Tokyo: KTK Scientific, Terra Scientific, **October**, pp. 17-23, (1988b).

58. Harris, S. J., Weiner, A. M. and Perry, T. A., *Appl. Phys. Lett.*, **53**, 1605, (1988).

59. Harris, S. J., Belton, D. N., Weiner, A. M. and Schmieg, S. J., *J. Appl. Phys.*, **66**, 5353, (1989).

60. Harris, S. J., and Weiner, A. M., *J. Appl. Phys.*, **67**, 6520, (1990).

61. Inspektor, A., Liou, Y., McKenna, T. and Messier, R., *Surf. Coatings Technol.*, **39/40**, 211, (1989).

62. Jansen, F., Chen, I. and Machonkin, M. A., *J. Appl. Phys.*, **66**, 5749, (1989).

63. Matsui, Y., Yabe, H. and Hirose, Y., *Jpn. J. Appl. Phys.*, **29**, 1552, (1990).

64. Matsui, Y., Yuuki, A. Sahara, M. and Hirose, Y., *Jpn. J. Appl. Phys.*, **28**, 1718, (1989).

65. Matsumoto, O., Toshima, H. and Kanzaki, Y., *Thin Soli. Films*, **128**, 341, (1985).

66. Mitsuda, Y. Tanaka, K. and Yoshida, T., *J. Appl. Phys.*, **67**, 3604, (1990).

67. Saito, Y., Sato, K., Tanaka, H., Fujita, K. and Matuda, S., *J. Mater. Sci.*, **23**, 842, (1987).

68. Zhu, W., Inspektor, A. Badzian, A., McKenna, T. and Messier, R., *J. Appl. Phys.*, **68**, 1489, (1990).

69. Frenklach, M. and Spear, K. E., *J. Mater. Res.*, **3**, 133, (1988).

70. Frenklach, M. and Wang, H., *Phys. Rev. B*, **43**, 1520, (1991).

71. Huang, D., Frenklach, M. and Maroncelli, M., *J. Phys. Chem.*, **92**, 6379, (1988).

72. Huang, D. and Frenklach, M., *J. Phys. Chem.*, **96**, 1868, (1991).

73. Peploski, J., Thompson, D. L. and Raff, L. M., *J. Phys. Chem.*, **96**, 8539, (1992).

74. Xing, J. and Scott. H. L., *Phys. Rev. B.*, **48**, 15 August, (1993).

75. Tsuda, M., Nakajima, M. and Oikawa, S., *J. Am. Chem. Soc.*, **108**, 5780, (1986).

76. Tsuda, M., Nakajima, M. and Oikawa, S., *Jap. J. Appl. Phys.*, **26**, L527, (1987).

77. Joffreau, P.-0., Bichler, R., Haubner, R. and Lux, B., *Int. J. Refract. Hard Metals.*, **7**, 92, (1988).

78. Joffreau, P.-0., Haubner, R. and Lux, B., *Int. J. Refract. Hard Metals.*, **7**, 186, (1988).

79. Lee, Y. H., Bachmann, K. J., Glass, J. T., LeGrice, Y. M. and Bemanich, R. J., *Appl. Phys. Lett.*, **57**, 1916, (1990).

80. Meilunas, R., Wong, M. S., Sheng, K. C., Chang, R. P. H. and Van Duyne, R. P., *Appl. Phys. Lett.*, **54**, 2204, (1989).

81. Ravi, K. V., Koch, C. A., Hu, H. S. and Joshi, A., *J. Mater. Res.*, **5-11**, 2356, (1990).

82. Belton, D. N., Harris, S. J., Schmieg, S. J. and Weiner, A. M., *Appl. Phys. Lett.*, **54**, 416, (1989).

83. Belton, D. N., and Schmieg, S. J., *Surf. Sci.*, **233**, 133, (1990).

84. Belton, D. N., and Schmieg, S. J., *Thin Solid Films*, **212**, 68, (1992).

85. Glass, J. T., Williams, B. E. and Davis, R. F., *SPIE Conf. Proc.*, **877**, 56, (1988).

86. Williams, B. E. and Glass, J. T., *J. Mater. Res.*, **4**, 373, (1989).

87. Williams, B. E., Glass, J. T., Davis, R. F. and Kobashi, K., *J. Cryst. Growth*, **99**, 1168, (1990).

88. Jansen, F., Machonkin, M. A. and Kuhman, D. E., *J. Vac. Sci. Technol.*, **A 8**, 3785, (1990).

89. Bachmann, P. K., Drawl, W., Knight, D., Weimer, R. and Messier, R. F., *Diamond and Diamond-Like Materials Synthesis*, extended abstracts, ed. Johnson, G. H., Badzian, A. R. and Geis, M. W., **Mater. Res. Soc. EA-15**, 99, (1988).

90. Polini, R., Gazzoli, D., Molinari, E., Sessa, V., Terranova, M. L., Ascarelli, P. and Fontana, S., *Diamond and Related Mater.*, **1**, 205, (1992).

91. Frenklach, M., *J. Chem. Phys.*, **97**, 5794, (1992).

92. Belton, D. N., and Harris, S. J., *J. Chem. Phys.*, **96**, 2371, (1992).

93. Harris, S. J., *Appl. Phys. Lett.*, **56**, 2298, (1990).

94. Harris, S. J. and Belton, D. N., *Thin Solid Films*, **212**, 193, (1992).

95. Harris, S. J. and Belton, D. N., *Japn. J. Appl. Phys.*, **30**, 2615, (1991).

96. Harris, S. J., Belton, D. N. and Blint, R. J., *J. Appl. Phys.*, **70**, 2654, (1991).

97. Bou, P., Boettner, J. C. and Vandenbulcke, L., *Jap. J. Appl. Phys.*, **31**, 2931, (1992).

98. Frenklach, M., *J. Appl. Phys.*, **65**, 5142, (1989).

99. Harrison, J. A., Brenner, D. W., White, C. T. and Colton, R. J., *Thin Solid Films*, **206**, 213, (1991).

100. Iarlori, S., Galli, G., Gygi, F., Parrinello, M. and Tosatti, E., *Phys. Rev. Lett.*, **69**, 2947, (1992).

101. Valone, S. M., Trkula, M. and Laia, J. R., *J. Mater. Res.*, **5**, 2296, (1990).

102. Agrawal, P. M., Raff, L. M. and Thompson, D. L., *Surf. Sci.*, **188**, 402, (1987).

103. Agrawal, P. M., Thompson, D. L. and Raff, L. M., *Surf. Sci.*, **195**, 283, (1988).

104. Agrawal, P. M., Thompson, D. L. and Raff, L. M., *J. Chem. Phys.*, **91**, 5021, (1989).

105. Brenner, D. W. and Carrison, B. J., *Surf. Sci.*, **198**, 151, (1988).

106. Brenner, D. W. and Garrison, B. J., *Adv. Chem. Phys.*, **76**, 281, (1989).

107. Brenner, D. W., Dunlap, B. I., Mintmire, J. W., Mowrey, R. C. and White, C. T., In *Proceedings of the Second International Symposium on Diamond Materials*, Purdes, A. J., Angus, J. C., Davis, R. f., Meyerson, B. M., Spear, K. E. and Yoder, M., Eds., The Electrochemical Society: Pennington, NJ, pp. 39, (1991).

108. Garrison, B. J., Dawnkaski, E. J., Srivastava, D. and Brenner, D. W., *Science*, **February**, 835, (1992).

109. Halicioglu, T., *Surf. Sci. Lett.*, **259**, L714, (1991).

110. Kaukonen, H.-P. and Nieminen, R. M., *Phys. Rev. Lett.*, **68**, 620, (1992).

111. Stillinger, F. H. and Weber, T. A., *Phys. Rev. Lett.*, **62**, 2144, (1989).

112. Srivastava, D., Garrison, B. J. and Brenner, D. W., *Phys. Rev. Lett.*, **63**, 302, (1989).

113. Weakliem, P. C. and Carter, E. A., *J. Chem. Phys.*, **96**, 3240, (1992).

114. Weber, T. A. and Stillinger, F. H., *J. Chem. Phys.*, **92**, 6239, (1990).

115. Zhao, X. G., Carmer, C. S., Weiner, B. and Frenklach, M., *J. Phys. Chem.*, **97**, 1639, (1993).

116. Stewart, J. P. P., *Quant. Chem. Prog. Exch. (QCPE)*, **No. 455**, (1983).

117. Chang, X. Y., Perry, M., Peploski, J., Thomplon, D. L. and Raff, L. M., *J. Chem. Phys.*, submitted, (1993).

118. Brenner, D. W., *Phys. Rev. B*, **42**, 9458, (1990).

119. Tersoff, J., *Phys. Rev. Lett.*, **61**, 2879, (1988).

120. Tersoff, J., *Phys. Rev. B*, **37**, 6991, (1988).

121. Tersoff, J., *Phys. Rev. B*, **38**, 9002, (1988).

122. Tersoff, J., *Phys. Rev. B*, **39**, 5566, (1989).

123. *Monter Carlo Method in Statistical Physics*, Vol. 7 of Topocs in Current Physics, edited by Binder, K., Springer, Heidelberg, (1979).

124. *Applications of the Monter Carlo Method in Statistical Physics*, Vol. 36 of Topocs in Current Physics, edited by Binder, K., Springer, Heidelberg, (1984).

125. Piersall, S. D. and Anderson, J. B., *J. Chem. Phys.*, **95**, 971, (1991).

126. Fichthorn, K. A. and Weinberg, W. H., *J. Chem. Phys.*, **95**, 1090, (1991).

127. Hood, E. S., Toby, B. H. and Weinberg, W. H., *Phys. Rev. Lett.*, **55**, 2437, (1985).

128. Rouhani, M. D. and Esteve, D., in *Interaction of Atoms and Molecules with Solid Surfaces*, edited by Bortolani, V., March, N. H. and Tosi, M. P., pp. 657, Plenum, New York, (1990).

129. Smith, R., in *Diamond and Diamond-Like Films and Coatings*, edited by Clausing, R. E., Horton, L. L., Angus, J. C. and Koidl, P., pp. 97, Plenum, New York, (1991).

130. Unac, R., Sales, J. L. and Zgrablich, G., *J. Phys. Chem.*, **95**, 9382, (1991).

131. Kang, H. C. and Weinberg, W. H., *J. Chem. Phys.*, **90**, 2824, (1989).

132. Mak, C. H., Andersen, H. C. and George, S. M., *J. Chem. Phys.*, **88**, 4052, (1988).

133. Chen, I., *J. Appl. Phys.*, **64**, 3742, (1988).

134. Kotecki, D. E. and Herman, I. P., *J. Appl. Phys.*, **64**, 4920, (1988).

135. Matsumura, S., Takano, K., Kuwano, N. and Oki, K., *J. Chryt. Growth*, **115**, 194, (1991).

136. Silverberg, M. and Ben-Shaul, A., *J. Chem. Phys.*, **87**, 3178, (1987).

137. Metropolis, N., Rosenbluth, A. W., Rosenbluth, M. N., Teller, A. H. and Teller, E., *J. Chem. Phys.*, **21**, 1087, (1953).

138. Fosdick, L. D., *Methods Comp. Phys.*, **1**, 245, (1963).

139. Müller-Krumbhaar, H. and Binder, K., *Jpn. J. Statist. Phys.*, **8**, 1, (1973).

140. *Simulation of Diffusion in Lattice Gases and Related Kinetic Phenomena*, in *Applications of the Monter Carlo Method in Statistical Physics*, Vol. 36 of Topocs in Current Physics, edited by Binder, K., pp. 181, Springer, Heidelberg, (1987).

141. Kawasaki, *Phys. Rev.*, **145**, 224, (1966).

142. Kawasaki, *Phys. Rev.*, **148**, 375, (1966).

143. Kawasaki, *Phys. Rev.*, **150**, 285, (1966).

144. Binder, K. and Heermann, D. W., *Monter Carlo Simulation in Statistical Physics, An Introduction*, Springer, Heidelberg, (1992).

145. Abell, G. C., *Phys. Rev. B*, **31**, 6184, (1985).

146. Tersoff, J., *Phys. Rev. Lett.*, **56**, 632, (1986).

147. Chang, X. Y. and Raff, L. M., unpublished results.

148. Meakin, P. and Jullien, R., *J. Physique*, **48**, 1651, (1987).

149. Baranauskas, V., Fukui, M., Rodrigues, C. R. and Parizotto, N., *Appl. Phys. Lett.*, **60**, 13, (1992).

150. Brenner, D. W., *Mat. Res. Soc. Symp. Proc.*, **141**, 59, (1989).

151. Erwin, S. C. and Pickett, W. E., *Solid State Comm.*, **81-11**, 891, (1992).

152. Harris, S. J. and Goodwin, D. G., *Appl. Phys. Chem.*, **97**, 23, (1993).

153. Kondoh, E., Ohta, T., Mitomo, T. and Ohtsuka, K., *J. Appl. Phys.*, **73**, 3041, (1993).

154. Mitsui, Y., Yuuki, A., Sahara, M. and Hirose, Y., *Jpn. J. Appl. Phys.*, **28**, 1718, (1989).

155. Mitsui, Y., Uabe, H. and Hirose, Y., *Jpn. J. Appl. Phys.*, **29**, 1552, (1990).

VITA 2

JIAN XING

Candidate for the Degree of

Doctor of Philosophy

Thesis: COMPUTER SIMULATION OF DIAMOND FILM GROWTH BY CHEMICAL VAPOR DEPOSITION USING MONTE CARLO METHOD

Major Field: Physics

Biographical:

Personal Data: Born in Chengdu, Sichuan, P. R. China, March 24, 1954, the son of Yu-Ting Xing and Shao-Kun Yang.

Education: Graduated from the 29th Middle School, Chengdu, Sichuan, P. R. China, May 1971; received Bachelor of Science Degree in Physics from Sichuan University, Chengdu, Sichuan, P. R. China in August 1982; received Master of Science Degree in Physics from Oklahoma State University, in July 1989; completed the requirements for the Doctor of Philosophy Degree at Oklahoma State University in December 1993.

Professional Experience: Research Assistant, Physical and Chemical Analysis Center, Steel Company, Chengdu, Sichuan, P. R. China, January 1976 to September 1978; Undergraduate Research Assistant, Sichuan University, Chengdu, Sichuan, P. R. China, September 1981 to August 1982; Researcher, Institute of Optics and Electronics, Chinese Academy of Sciences, September 1982 to April 1985; Technical Service Engineer, China Service Center of BAIRD Corporation (USA), April 1985 to February 1987; Graduate Research Assistant, Oklahoma State University, June 1988 to present.